# Application of Attosecond Techniques to Condensed Matter Systems

DISSERTATION

Presented in Partial Fulfillment of the Requirements for the Degree Doctor of Philosophy in the Graduate School of The Ohio State University

By

Gregory J. Smith, B.Sc., M.Sc.

Graduate Program in Physics

The Ohio State University

2020

Dissertation Committee:

Louis F. DiMauro, Advisor

L. Robert Baker

Jay A. Gupta

Yuri V. Kovchegov

# Abstract

design and construction of attosecond transient absorption beamline.

design and testing of a bright XUV source

initial transient absorption experiments in germanium

Dedicated to my family.

# Acknowledgments

Lou DiMauro and Pierre Agostini - of course. say something up here about them and the group in general.

Thank you to the following people who have helped me throughout my scientific career:

- Stephen Hageman - most work in this thesis was done in close collaboration with Steve. major components of beamline were designed solely by Steve, and he was there to help in nearly every single experiment. endless discussions on nearly every aspect of all experimental and design work.
- Andrew Piper for designing the OMRON vacuum control system, and attempting to implement interferometric stabilization on the TABLe.
- Dietrich Keissewetter for coding the Thorlabs/Newport motor interface and the home-made beamline pointing software. Also, thanks for helping with the initial design of the TABLe apparatus, helping to chase down vibrations and making subtle improvements to the apparatus.
- Kent Talbert for writing the entire LavVIEW software data collection suite.
- Antoine Camper for implementing the phase plate and phase gratings, as well as helping calibrate the photon spectrometer.
- Jakub Husek, Anthony Cirri, Somnath Biswas & Prof. Robert Baker for many discussions pertaining to data collection, experimental design and sample considerations.
- Cristian Ott for designing the original “cage and crank” vacuum flange manipulator, which we adapted to work with our photon spectrometer.
- Sierra O’Bryan for doing the initial optical design of the photon spectrometer.
- Yaguo Tang, Michael Chilcote, Michael Newburger, Jinson Xu & Yutichai Mueangern from OSU, Prof. S.K. Sundaram from Alfred University, Grant Johnson, Venkateshkumar (Venky) Prabhakaran, Le Wang & Yingge Du from PNNL - for sample preparation.

- Eric Moore for automating the TABLe alignment system.
- Marieke Jager from the Leone group and Norman Niewrzella from the Semiconductor Manufacturing Technology Business Group at Carl Zeiss SMT GmbH, for answering my questions about ellipsoidal mirrors.
- Pete Gosser and Michael Graham at the Physics Machine Shop for machining countless parts (including our vacuum chambers) and providing endless consulting about general machining practices. Special thanks to Jon Shover from the Astronomy Machine Shop for welding our vacuum chambers and some components on the high pressure cell.
- Tim Gorman for endless discussions about physics, experimental design, laser troubleshooting, and good conversations.
- Rich Pfisterer, Ryan Irvin and Donna Pfisterer from Photon Engineering, for providing me a university gratis software license of FRED, and for teaching me to use the software efficiently.
- Phil Davids and Mark Reed for helping out with general building problems. Kent Ludwig for helping repair our rough vacuum system.
- Kris Dunlap, Mary Kay Jackson, Shirley McClung, Dameyon Shipley, Kyle Schechter and Jessica Middleton for help with administrative issues.
- Jack Simonson, Carlos Marques, Meigan Aronson & Jacob Grosse from BNL for fostering my interest in science and encouraging me to go to graduate school. They set me down this path and I thank them for it.
- From my time in Dr. Yang's group: Nick Minutillo, Yi-Shin Chiu, Zeke, Prof. Yang.
- Everyone else in the DiMauro group who has helped me throughout the years: Stephen Schoun, Tim Scarborough, Cosmin Blaga, Hyunwook Park, Junliang Xu, Urszula Szafruga, Kaikai Zhang, Kevin Gudenkauf, Zhou Wang, Yu Hang (Marco) Lai, Bryan Smith, Sha (Lisa) Li, Abraham Camacho, Daniel Tuthill, Vyacheslav (Slava) Leshchenko, Li Fang.

# VITA

| | |
|---|---|
| 2010 | B.Sc. Physics & Mathematics. SUNY Stony Brook, Stony Brook, NY |
| 2010 - 2012 | Research Analyst. Correlated Electron Group, Condensed Matter Physics and Materials Science Division at Brookhaven National Laboratory, Upton, NY |
| 2014 | M.Sc. Physics. The Ohio State University, Columbus, OH |
| 2014 - present | Graduate Research Associate. The Ohio State University, Columbus, OH |

## Publications

A. Camper, H. Park, S. J. Hageman, **G. Smith**, T. Auguste, P. Agostini and L. F. DiMauro. High relative-phase precision beam duplicator for mid-infrared femtosecond pulses. *Opt. Lett.*, 44(22):5465-5458, Nov. 2019.

L. Steinke, J. W. Simonson, W.-G. Yin, **G. J. Smith**, J. J. Kistner-Morris, S. Zellman, A. Puri, and M. C. Aronson. $CaMn_2Al_{10}$: Itinerant Mn magnetism on the verge of magnetic order. *Phys. Rev. B*, 92(2):020413, July 2015.

W. Miiller, J. M. Tomczak, J. W. Simonson, **G. Smith**, G. Kotliar, and M. C. Aronson. Protected Fe valence in quasi-two-dimensional $\alpha$-$FeSi_2$. *J. Phys.: Condens. Matter*, 27(17):175601, May 2015.

Y.-H. Chiu, N. G. Minutillo, R. E. Williams, **G. J. Smith**, D. W. McComb, J. A. Carlin, E. Johnston-Halperin, and F. Yang. Photoluminescence evolution in GaAs/AlGaAs core/shell nanowires grown by MOCVD: Effects of core growth temperature and substrate orientation. *Journal of Crystal Growth*, 429:1, Nov. 2015.

**G. J. Smith**, J. W. Simonson, T. Orvis, C. Marques, J. E. Grose, J. J. Kistner-Morris, L. Wu, K. Cho, H. Kim, M. A. Tanatar, V. O. Garlea, R. Prozorov, Y. Zhu, and M. C. Aronson.

Intrinsic nanostructure in $Zr_{2-x}Fe_4Si_{16-y}$ ($x = 0.81$, $y = 6.06$). *J. Phys.: Condens. Matter*, 26(37):376002, Sept. 2014.

J. W. Simonson, M. E. Pezzoli, V. O. Garlea, **G. J. Smith**, J. E. Grose, J. C. Misuraca, G. Kotliar, and M. C. Aronson. Local moments and suppression of antiferromagnetism in correlated $Zr_4Fe_4Si_7$. *Phys. Rev. B*, 88(8):081107, Aug. 2013.

J. W. Simonson, Z. P. Yin, M. Pezzoli, J. Guo, J. Liu, K. Post, A. E. Menko, N. Hollmann, Z. Hu, H.-J. Lin, C.-T. Chen, C. Marques, V. Leyva, **G. Smith**, J. W. Lynn, L. L. Sun, G. Kotliar, D. N. Basov, L. H. Tjeng, and M. C. Aronson. From antiferromagnetic insulator to correlated metal in pressurized and doped LaMnPO. *PNAS*, 109(27):E1815, July 2012.

J. W. Simonson, **G. J. Smith**, K. Post, M. Pezzoli, J. J. Kistner-Morris, D. E. McNally, J. E. Hassinger, C. S. Nelson, G. Kotliar, D. N. Basov, and M. C. Aronson. Magnetic and structural phase diagram of $CaMn_2Sb_2$. *Phys. Rev. B*, 86(18):184430, Nov. 2012.

J. W. Simonson, K. Post, C. Marques, **G. Smith**, O. Khatib, D. N. Basov, and M. C. Aronson. Gap states in insulating $LaMnPO_{1-x}F_x$ ($x = 0 - 0.3$). *Phys. Rev. B*, 84(16):165129, Oct. 2011.

## Fields of Study

Major Field: Physics

Studies in Ultrafast Physics: Agostini-DiMauro Ultrafast Atomic Physics Research Group

# Table of Contents

# List of Figures

# List of Tables

# Chapter 1
# Introduction

## 1.1 Ultrafast Dynamics in Condensed Matter Systems

timescales and processes in solids

## 1.2 Attosecond Transient Absorption Spectroscopy (ATAS)

**why are you doing it with HHG?**

include figure of pulse duration vs photon energy, showing different light sources (synchrotrons, HHG sources, XFEL, etc.) tie this into the timescales neccessary to probe condensed matter physics.

### 1.2.1 overview of the technique

references [73]

The basic concept of an *attosecond transient absorption spectroscopy* (ATAS) experiment is shown in **??**. In this experiment, a sample is placed at the combined XUV/IR focus in a transmission (normal) geometry. An XUV photon spectrometer is placed behind the sample and the transmitted XUV spectrum $S$ is measured as a function of XUV-IR delay. The IR light is not measured by the spectrometer.

Fundamentally, changes in photoabsorption correspond to electron and phonon dynamics in the sample. In condensed matter materials, these processes occur on the picosecond ($10^{-12}$ s), femtosecond ($10^{-15}$ s) and even attosecond ($10^{-18}$ s) time scales [21, 78, 89, 94]. At XUV energies, photons drive electronic transitions from a core-level state to one near the Fermi level, which requires electron population in the initial state and a vacancy in the final state. Because the initial state is tens or even hundreds of eV below the bandgap, it is shielded from the external IR field. The final states, being closer to the Fermi level, enjoy no such shielding. Therefore they can be distorted by the external IR field, and the electron population can be transferred between these states in response to the IR field. After an

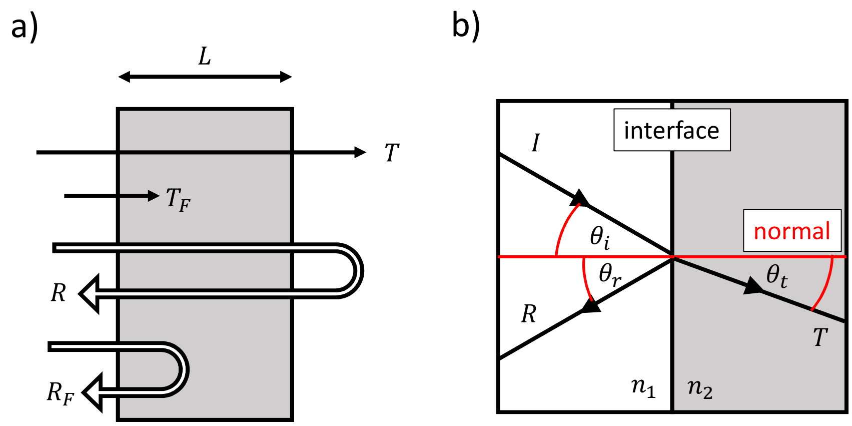


Figure 1.1: Normal and non-normal incident geometries. **a)** Normal incidence geometry showing Fresnel coefficients $R_F$, $T_F$ for interfaces and total transmission $T$ and reflectance $R$ for a slab of thickness $L$. Figure recreated from [61]. **b)** Non-normal geometry showing definitions of angles $\theta_i, \theta_r$ and $\theta_t$ with respect to each interface.

initial IR excitation, electrons relax via different scattering channels, including with other electrons or phonon modes with longer lifetimes. Provided the dipole selection rules allow it, the photoabsorption spectrum is sensitive to all of these dynamics. Thus by measuring the XUV spectrum as a function of XUV-IR delay, we can track the electronic and phononic response of a sample to an ultrafast IR excitation.

**induced dipole interpretation**

**population transfer and probing interpretation**

**comparison of absorptive and reflective measurements**

In a transient absorption experiment, we measure the transmission $T$ of a sample in response to excitation by an external field. Generally speaking, $T$ depends on both parts of the complex refractive index: $\tilde{n} = n + ik$. However, in a normal transmission geometry it turns out that the contribution of $\mathrm{Im}(\tilde{n})$ dominates the measured signal, and to a good approximation the role of $\mathrm{Re}(\tilde{n})$ can be ignored. Note that in a non-normal reflection geometry, both parts of $\tilde{n}$ make significant contributitions to the measured signal. In the following discussion we will analyze the Fresnel equations to see why this is the case. This section will draw from arguments made in reference [61].

First, we consider the normal geometry shown in the left panel of Fig. 1.1. We write the complex index of refraction in the following form:

$$\begin{aligned}\tilde{n} &= n - ik \\ &= (1 - \delta) - i\beta\end{aligned} \tag{1.1}$$

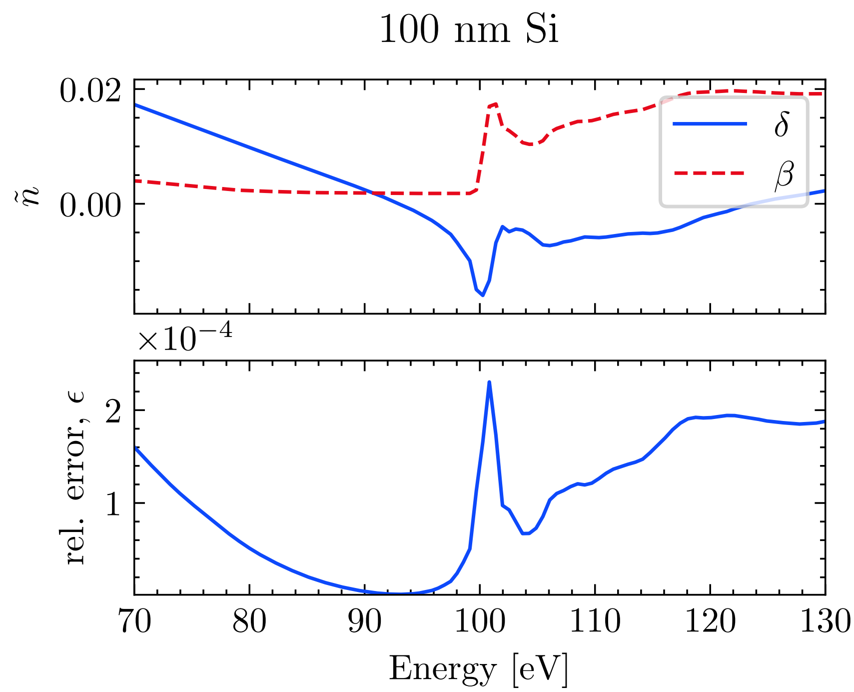


Figure 1.2: Consequences of ignoring the real part of $\tilde{n}$ when calculating the transmission $T$ of a thin sample. Top panel: complex refractive index of silicon using the notation from Eq. (1.1). The Si $L$-edge absorption feature is visible near 100 eV. Data from [32]. Bottom panel: relative error in $T$, as defined in Eq. (1.8), introduced by ignoring the contribution of $\mathrm{Re}(\tilde{n})$. An infinite number of bounces (e.g., Eq. (1.6)) is assumed.

The Fresnel coefficients $R_F$ and $T_F$ describe the interface reflectance and transmittance and depend on both parts of the complex index $\tilde{n}$. For normal incidence, they are:

$$\begin{aligned} R_F &= \left| \frac{n - ik - 1}{n - ik + 1} \right|^2 \\ T_F &= \frac{4n}{|n - ik + 1|^2} \end{aligned} \tag{1.2}$$

Absorption in the bulk is described via the absorption length $\alpha$:

$$\alpha = 4\pi k / \lambda \tag{1.3}$$

Ignoring interface effects, the transmisison through the bulk is:

$$T_{\text{bulk}} = \exp(-\alpha L) \tag{1.4}$$

Note that $\alpha$ and $T_{\text{bulk}}$ only depend on $k$.

The total reflectance $R$ and transmission $T$ are the result of interface effects plus bulk effects. We must consider the case where the detected light is the result of multiple reflections within the sample. Neglecting interference, we consider the case of $2N$ bounces where the laser's coherence length is less than the thickness of the bulk. In this case, the sum is incoherent with the expressions for $T$ and $R$ given by:

$$\begin{aligned} R &= R_F + R_F T_F^2 T_{\text{bulk}}^2 \sum_{m=0}^{N} \left[ R_F T_{\text{bulk}} \right]^{2m} \\ T &= T_F^2 T_{\text{bulk}} \sum_{m=0}^{N} \left[ R_F T_{\text{bulk}} \right]^{2m} \end{aligned} \tag{1.5}$$

For the case of an infinite number of bounces, Eq. (1.5) simplifies to:

$$\begin{aligned} R &= R_F + \frac{R_F T_F^2 T_{\text{bulk}}^2}{1 - R_F^2 T_{\text{bulk}}^2} \\ T &= \frac{T_F^2 T_{\text{bulk}}}{1 - R_F^2 T_{\text{bulk}}^2}, \end{aligned} \tag{1.6}$$

whereas if only a single bounce occurs, Eq. (1.5) reduces to:

$$\begin{aligned} R &= R_F + R_F T_F^2 T_{\text{bulk}}^2 \\ T &= T_F^2 T_{\text{bulk}} \end{aligned} \tag{1.7}$$

We now consider the fractional error introduced by ignoring the interface effects described by $T_F$ and $R_F$. That is, what would happen if we assume that the interfaces have no effect on the transmitted intensity? We introduce the relative error $\epsilon$ made by ignoring the Fresnel coefficients of Eq. (1.6):

$$\epsilon \equiv \frac{T_{\text{bulk}}}{T} - 1 \tag{1.8}$$

As an example, consider a 100 nm thick Si sample measured in transmission near the Si $L$-edge (about 100 eV), as shown in Fig. 1.2. The relative error is in the range of one part in $10^4$ to $10^5$, well below our experimental detection limit. Silicon was chosen due to its data availability above and below the absorption edge, but this behavior should hold for all materials in normal transmission.

The real part of the complex index becomes important when the sample isn't normal to the beam, as shown in the right panel of Fig. 1.1. In this case, the Fresnel equations are a bit messier:

$$\begin{aligned} R_s &= \left| \frac{\tilde{n}_1 \cos\theta_i - \tilde{n}_2 \cos\theta_t}{\tilde{n}_1 \cos\theta_i + \tilde{n}_2 \cos\theta_t} \right|^2 \\ R_p &= \left| \frac{\tilde{n}_1 \cos\theta_t - \tilde{n}_2 \cos\theta_i}{\tilde{n}_1 \cos\theta_t + \tilde{n}_2 \cos\theta_i} \right|^2 \\ T_s &= 1 - R_s \\ T_p &= 1 - R_p \end{aligned} \tag{1.9}$$

Here, the subscripts $s$ and $p$ denote the polarization relative to the surface normal. For a sample in vacuum, $\tilde{n}_1 = 1$ and $\tilde{n}_2$ is the index of the sample. We can extract the relevant physics without any additional manipulation of Eq. (1.9). Right away, we can see that unlike Eq. (1.2), Eq. (1.9) is symmetric in the real and imaginary parts of the sample's complex index, $\tilde{n}_2$. In the limit of a thick slab, ($L \gg \alpha$), the light is attenuated before it can reflect off the back surface and we have $T \to 0$ and $R \to R_{s,p}$. That is, the only contributions to the reflected intensity are from the interface and possibly the sample volume within $z \approx 1/\alpha$ of the interface. As a result, both parts of $\tilde{n}_2$ will make significant contributions to the reflected intensity. This geometry is common in transient reflection-absorption experiments [18, 42].

complex refractive index

sample requirements and preparation

pointing stability (in reflection, sample is an XUV optic)

### 1.2.2 previous work

what is state of the art?

previous work in condensed matter (Si, Ge, Si-Ge, etc)

motivation for long-wavelength studies in condensed matter

### 1.2.3 physical observables in ATAS

limited k-space information (requires single crystal)

transmission geometry measures imaginary and not the real part of n

### 1.2.4 interpretation of experimental data

absorbance $A$:

$$A(E) = -\log_{10}(T) = -\log_{10}\left(\frac{S_{\text{gs}}(E)}{S_{\text{vac}}(E)}\right) \tag{1.10}$$

change in absorbance $\Delta A$:

$$\begin{aligned}\Delta A(E,\tau) &= A_{\text{sig}}(E,\tau) - A_{\text{gs}}(E) \\ &= -\log_{10}\left(\frac{S_{\text{sig}}(E,\tau)}{S_{\text{vac}}(E)}\right) - \log_{10}\left(\frac{S_{\text{gs}}(E)}{S_{\text{vac}}(E)}\right) \\ &= -\log_{10}\left(\frac{S_{\text{sig}}(E,\tau)}{S_{\text{gs}}(E)}\right) \end{aligned} \tag{1.11}$$

## 1.3 High Harmonic Generation

High harmonic generation (HHG) is the extremely nonlinear process in which a strong infrared field produces light with frequencies that are integer multiples of the fundamental field after interacting with a medium. Rather than providing a first principles discussion of HHG, the main objective of this section is to understand how we can produce bright attosecond XUV light pulses with a sufficient spectral coverage for use in an ATAS experiment.

We consider the case of an atom in strong laser field, where the electric field of the laser is comparable to the Coulomb field of the parent atom. Under these conditions, there is an appreciable chance of ionization. To determine which physical process is responsible for the ionization, we must consider two energy scales: the ionization potential of the atom $I_p$ and the ponderomotive energy $U_p$:

$$U_p = \frac{q_e^2 F_0^2}{4 m_e \omega^2} \propto I_0 \lambda^2 \tag{1.12}$$

where $m_e$ is the electron mass, $q_e$ is the electron charge, $\omega$ is the frequency, $F_0$ is the electric field strength, $I_0$ is the intensity, and $\lambda$ is the wavelength of the laser. A more useful form of Eq. (1.12) is given below:

$$U_p\ [\text{eV}] = \left(9.33738 \times 10^{-5}\right) \times I_0[\text{PW/cm}^2] \times \lambda[\text{nm}]^2 \tag{1.13}$$

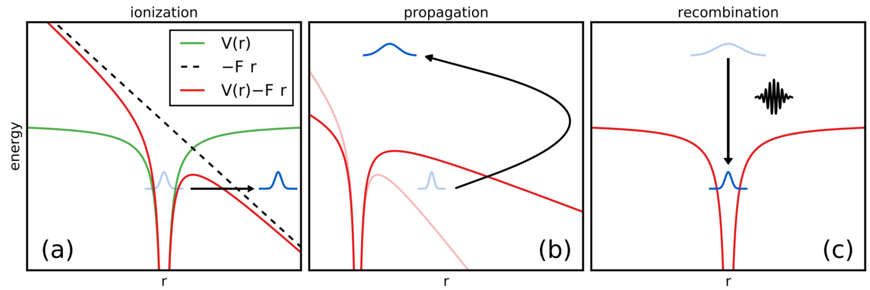


Figure 1.3: The three step model of HHG. Figure adapted from [77].

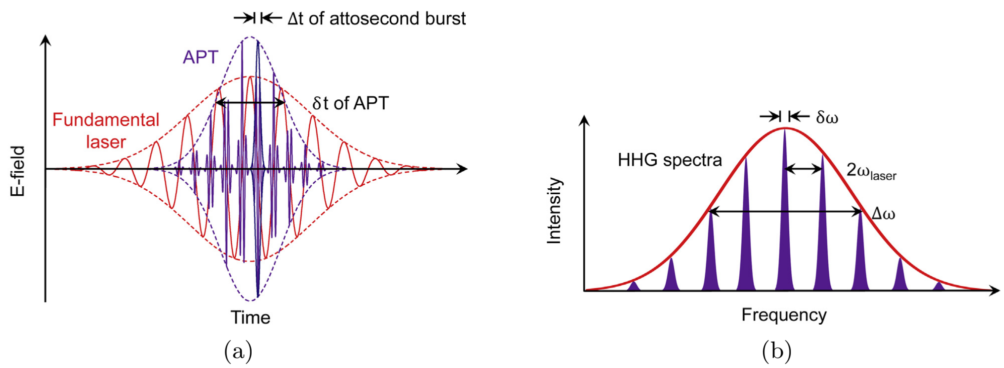


Figure 1.4: Time and frequency domain pictures of HHG. Figure adapted from [24].

The Keldysh parameter $\gamma$ compares the magnitudes of these two energy scales [45]:

$$\gamma = \sqrt{\frac{I_p}{2U_p}} \tag{1.14}$$

The value of $\gamma$ determines the physical mechanism responsible for ionization. When $\gamma \gg 1$, we are in the multi-photon ionization (MPI )regime; $\gamma \leq 1/2$ corresponds to tunnel ionization, and $\gamma \ll 1$ corresponds to over the barrier (OTB) ionization. We will restrict our discussion to the tunnelling regime, where HHG occurs.

- spectral coverage of harmonics

- pulse duration of harmonic light

Gas phase HHG

symmetry leads to odd harmonics.

gas and solid HHG has been studied

| atom | $I_p$ [eV] | $I_p$ [at. u.] | $l$ | $m$ | $F_0$ [at. u.] | $F_b$ [at. u.] |
|---|---|---|---|---|---|---|
| He | 24.5874 | 0.90357 | 0 | 0 | 2.42946 | 0.20412 |
| Ne | 21.5645 | 0.792481 | 1 | 0 | 1.99547 | 0.15702 |
| Ar | 15.7596 | 0.579155 | 1 | 0 | 1.24665 | 0.08386 |
| Kr | 13.9996 | 0.514476 | 1 | 0 | 1.04375 | 0.06617 |
| Xe | 12.1298 | 0.445762 | 1 | 0 | 0.84187 | 0.04968 |

Table 1.1: ADK parameters.

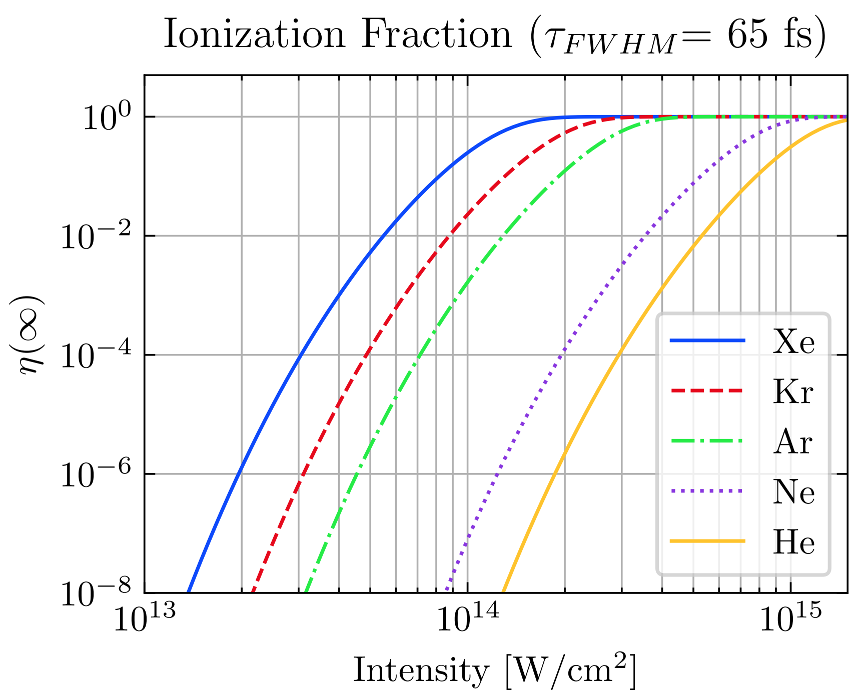


Figure 1.5: Ionization fraction following a 65 fs pulse, calculated using the cycled-averaged OTB-corrected ADK rate.

### 1.3.1 Single Atom Response

We start with a microscopic picture of harmonic generation, focusing on the interaction between a single atom and the laser field. In the early 1990s, a semi-classical model was developed to describe the process of high harmonic generation in three discrete steps: tunnel ionization, classical propagation in the vacuum, and recombination of the electron and the parent ion [20, 76]. This model accurately predicts many of the fundamental features of HHG.

#### Strong Field Ionization

In the three step model, the electric field strength is on the order of the atomic potential that binds the electron to its parent atom. The valence electron's wavepacket evolves subject to the sum of the shielded Coloumb field and the spatially varying laser field. The electron can tunnel out of the distorted Coloumb field, as shown in the left panel of Fig. 1.3. This step is most likely to occur at the peak of the field, which occurs every half-cycle of the laser period.

The ionization rate from the ground state in the tunnelling regime is best described by an analytical formula first derived by Ammosov, Delone and Krainov in 1986 [1, 15, 52]. The resulting equation bears their names (ADK):

$$w_{ADK}(F)\ [\text{at. u.}] = c^2_{n^*l^*} f(l,m) I_p \left(\frac{2F_0}{F}\right)^{2n^*-|m|-1} \exp\left(-\frac{2F_0}{3F}\right) \tag{1.15}$$

with

$$c^2_{n*l^*} = \frac{2^{2n^*}}{n^*\Gamma(n^*+l^*+1)\Gamma(n^*-l^*)} \tag{1.16}$$

$$f(l,m) = \frac{(2l+1)(l+|m|)!}{2^{|m|}(|m|)!\,(l-|m|)!} \tag{1.17}$$

$$F_0 = \sqrt{2I_p} \tag{1.18}$$

$$n^* = \frac{1}{\sqrt{2I_p}} \tag{1.19}$$

$$l^* = n^* - 1 \tag{1.20}$$

In the above equations, $\Gamma$ is the Gamma function; $F$ is the field amplitude; $I_p$ is the ionization potential; $l$ and $m$ are the orbital and magnetic quantum numbers of the valence electron, respectively; $n^*$ is the effective quantum number and $l^*$ is the effective orbital qunatum number. Note that the ADK rate is indepenent of laser frequency, and is valid when $\gamma < 0.5$. The ADK parameters for various atoms are listed in Table 1.1.

If the laser field is strong enough, the Coloumb field will be suppressed below the initial state and the electron can ionize without tunnelling. This ionization channel is called *over* *the barrier* or *barrier suppression* ionization. At this point the ADK formula breaks down. The field strength at which the laser field is equal to the Coloumb field is:

$$F_b = \frac{I_p^2}{4} \tag{1.21}$$

Tong and Lin introduced an empirical correction to the ADK formula to model the barrier suppression regime [86]:

$$W_{OTB}(F) = W_{ADK}(F) \exp\left(-\frac{2\alpha Z_c^2}{\sqrt{F_0}} F\right) \tag{1.22}$$

where $\alpha$ is an experimentally derived correction factor and $Z_c = 1$ for neutral atoms. The cycle averaged ADK rate is:

$$\bar{w}_{ADK}(F) = \sqrt{\frac{2}{\pi}} \sqrt{\frac{3F}{2(2I_P)^{3/2}}} w_{ADK}(F) \tag{1.23}$$

In the above equations, the ionization rate is expressed as a rate per atomic unit of time. Conversions to experimentally convenient units are given below:

$$F \text{ [at. u.]} = \sqrt{\frac{I \text{ [W/cm}^2\text{]}}{3.55 \times 10^{16}}} \tag{1.24}$$

$$w_{ADK} \text{ [at. u.]} = \frac{w_{ADK} \text{ [1/s]}}{41.341 \times 10^{15}} \tag{1.25}$$

The fraction of atoms ionized by time $t$ is found by integrating the rate of ionization:

$$\eta(t) = 1 - \exp\left(-\int_{-\infty}^{t} \omega(t')\,\mathrm{d}t'\right) \tag{1.26}$$

The ionization fraction for a 65 fs pulse using Eqs. (1.22) and (1.26) is shown in Fig. 1.5 for various generating media.

### Propagation and Recombination

The recently liberated electron is assumed to be born with zero initial kinetic energy. It accelerates in the oscillating laser field, gaining kinetic energy along the way, as shown in the central panel of Fig. 1.3. Its kinetic energy is proportional to the cycle-averaged quiver energy $U_p$.

The birth phase of the electron (relative to the laser period) determines its classical trajectory. Some electrons will be driven away from the parent ion, never to return; some will be driven back to the birth location, where they can scatter off of, miss, or recombine with the parent ion. We will only concern ourselves with those electrons that recombine (right panel of Fig. 1.3). Upon recombination, the electron will emit a photon of energy

$I_p + KE$, where $I_p$ is the ionization potential of the atom and $KE$ is the kinetic energy acquired during the propagation step. A classical analysis of the electron propagation reveals that the maximum kinetic energy such an electron can gain is $3.17U_p$, and therefore the maximum photon energy is:

$$E_{cutoff} = \hbar\omega_{\text{cutoff}} = I_p + 3.17U_p \tag{1.27}$$

This quantity is often called the cutoff energy, and it is proportional to $I_0\lambda^2$. Thus, we can extend the maximum photon energy of the harmonics by increasing the fundamental wavelength of the laser.

Unfortunately, the brightness of an individual harmonic order will decrease strongly with increasing wavelength, with the intensity scaling between $\lambda^{-5}$ and $\lambda^{-6}$ [80, 85]. We can conceptually understand this as the compounding of two separate problems [54]. First, longer wavelengths extend the cutoff energy, spreading a fixed harmonic conversion efficiency across more harmonics and lowering the brightness of each individual harmonic. This accounts for a factor of $\lambda^{-2}$. Secondly, the recombination probability scales inversely with square of the electron wavepacket spread that occurs during the propagation step. Longer wavelengths mean longer excursion times $\tau$, and the wavepacket spreads out as $\tau^{3/2}$. Since we are concerned with the harmonic intensity, we square this value to get $\tau^3 \propto \lambda^{-3}$. With this simple argument, we can see why the harmonic brightness should decrease as $\lambda^{-5}$.

So far, it appears that XUV spectrum is continuous in energy, ranging from $I_p$ to $\hbar\omega_{\text{cutoff}}$. This is because we have been considering the effects of a single-cycle laser pulse. In a multi-cycle pulse, the ionization-propagation-recombination steps will happen twice per pulse (every $T_0/2$ seconds), and each event results in a brief burst of light, as shown in Fig. 1.4a. If we Fourier transform this comb of attosecond pulses, we will get a comb in the frequency domain with separation $2\omega_0$, as shown in Fig. 1.4b. Thus, we expect to see only odd harmonics of the laser frequency $\omega_0$.

### 1.3.2 Macroscopic Picture

We now zoom out to the macroscopic picture, which encompasses the entire gas-laser interaction volume. In the far field, the radiation from individual atoms will be coherently summed to form an bright XUV light source. The overall efficiency of the HHG process depends on the phase mismatch $\Delta k$ of the individual dipoles across the interaction volume. We will see how the phase matching determines optimal interaction pressures for a given driving wavelength. Additionally, we will see the effect of XUV reabsorption by the gas on the overall XUV brightness.

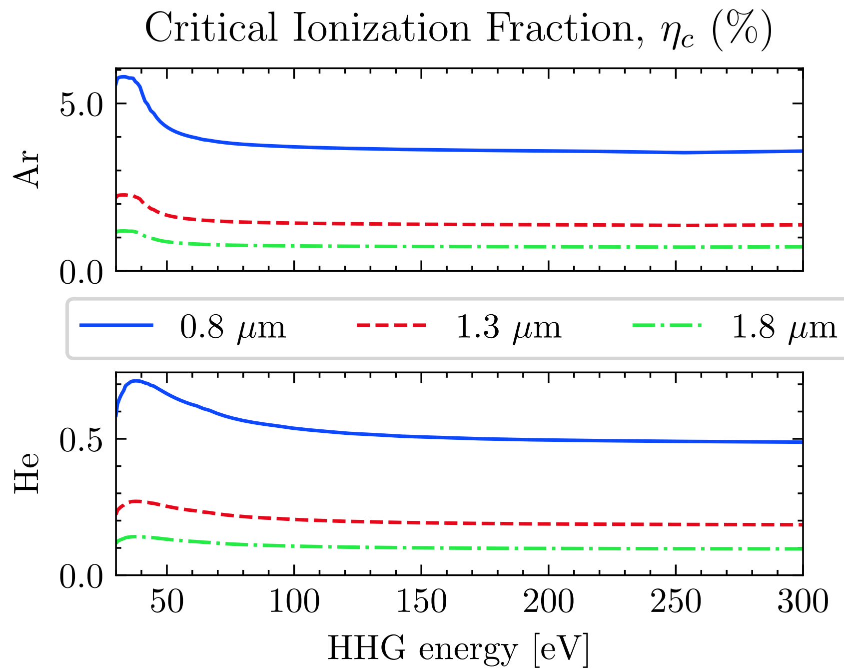


Figure 1.6: The critical ionization fraction, $\eta_c$ for helium and argon at different fundamental wavelengths. Refractive index information from [32, 56, 67].

### Phase Matching

HHG will be an efficient process if the wave vector mismatch $\Delta k$ of the independent dipoles is zero. The phase mismatch term can be expressed as four separate factors, each arising from distinct physical phenomena [74]:

$$\Delta k \equiv qk_{\omega} - k_{q\omega} = \Delta k_{\text{neutral}} + \Delta k_{\text{plasma}} + \Delta k_{\text{Gouy}} + \Delta k_{\text{dipole}} \tag{1.28}$$

The first two term represents the dispersion from the generating neutral atoms and the electron plasma. In the discussion that follows below, we will use the refractive index $n$ at STP (pressure $P_0$, number density $\rho_0$, temperature $T_0$), where literature values are readily available. We assume that the index scales linearly with the interaction pressure (density). That is, we assume $n(\rho) = (1-\eta)(\rho/\rho_0)n(\rho_0)$, where $\rho$ is the interaction density before any atoms are ionized and $\eta$ is the ionization fraction of the gas medium. For brevity, we will write the index of refraction at STP as $n = n(\rho_0)$. Using this notation, the neutral dispersion mismatch term for an interaction density $\rho$ is:

$$\begin{aligned}\Delta k_{\text{neutral}} &= qk_{\text{neutral}}(\lambda_1) - k_{\text{neutral}}(\lambda_q) \\ &= \frac{2\pi q}{\lambda_1}(1-\eta)\frac{\rho}{\rho_0}\Delta n\end{aligned} \tag{1.29}$$

where we have used $k(\lambda) = \omega n/c = n/(2\pi\lambda)$ and defined $\Delta n$ as:

$$\Delta n \equiv n_{\text{neutral}}(\lambda_1) - n_{\text{neutral}}(\lambda_q) \tag{1.30}$$

using the notation $\lambda_q \equiv \lambda_1/q$ for the wavelength of the $q^{th}$ harmonic with frequency $\omega_q \equiv q\omega$ and $\lambda_1$ ($\omega_1$) for the laser wavelength (frequency). To compute the plasma mismatch term, we start with the refractive index of a plasma:

$$n_{\text{plasma}}(\omega) = \sqrt{1 - \frac{\omega_p^2}{\omega^2}} \approx 1 - \frac{\omega_p^2}{2\omega^2} \tag{1.31}$$

$$\omega_p = \sqrt{\frac{e^2 \rho_e}{\epsilon_0 m_e}} \tag{1.32}$$

where $\omega_p$ is the plasma frequency and $\rho_e = \eta\rho$ is the plasma density. Then, the phase mismatch of the plasma is:

$$\begin{aligned}
\Delta k_{\text{plasma}} &= q k_{\omega_1} - k_{q\omega_1} \\
&= \frac{q}{2\pi\lambda_1}(n_{\text{plasma}}(\omega_1) - n_{\text{plasma}}(\omega_q)) \\
&= -\frac{1}{4\pi\lambda_1}\frac{q^2-1}{q}\frac{\omega_p^2}{\omega_1^2} \\
&\approx -\frac{q}{4\pi\lambda_1}\frac{\omega_p^2}{\omega_1^2} \quad \text{(for large } q\text{)} \\
&= -q\eta\rho r_e \lambda_1
\end{aligned} \tag{1.33}$$

Where $r_e$ is the classical electron radius:

$$r_e = \frac{1}{4\pi\epsilon_0}\frac{e^2}{m_e c^2} \tag{1.34}$$

Note that since $\Delta n > 0$ for the wavelengths of interest, we have $\Delta k_{\text{plasma}} \leq 0$. Adding the two dispersive terms together, we get an expression for the dispersive phase mismatch terms:

$$\Delta k_{\text{neutral}} + \Delta k_{\text{plasma}} = \frac{2\pi q}{\lambda_1}(1-\eta)\frac{\rho}{\rho_0}\Delta n - q\eta\rho r_e \lambda_1 \tag{1.35}$$

Inspection of Eq. (1.35) reveals that there exists a *critical ionization fraction* $\eta_c$ for which the dispersive phase terms sum to zero:

$$\eta_c \equiv \left(1 + \frac{\rho_0 r_e \lambda_1^2}{2\pi\Delta n}\right)^{-1} \tag{1.36}$$

We can rewrite Eq. (1.35) using $\eta_c$:

$$\Delta k_{\text{neutral}} + \Delta k_{\text{plasma}} = \frac{2\pi q \Delta n}{\lambda_1} \frac{\rho}{\rho_0} \left(1 - \frac{\eta}{\eta_c}\right) \tag{1.37}$$

The critical ionization fraction for helium and argon is shown in Fig. 1.6. Note that for $\eta < \eta_c$, the dispersive mismatch term is positive. We will see below that at the IR focus, phase matching ($\Delta k = 0$) is impossible for $\eta > \eta_c$.

The third term of Eq. (1.28) is the geometrical phase mismatch caused by focusing:

$$\begin{aligned} \Delta k_{\text{Gouy}} &= \frac{\partial}{\partial z}\left[q \arctan\left(\frac{2z}{b_1}\right) - \arctan\left(\frac{2z}{b_q}\right)\right] \\ &= q\frac{2b_1}{b_1^2 + 4z^2} - \frac{2b_q}{b_q^2 + 4z^2} \\ &\approx -(q-1)\frac{2b_1}{b_1^2 + 4z^2} \end{aligned} \tag{1.38}$$

where $b_1 = 2z_R$ is the confocal parameter and $z_R$ is the Rayleigh range. For the $q^{th}$ harmonic, we assume the nonlinear process obeys a power law $p$ and $b_q = b_1 p/q$ [77]. Note that $\Delta k_{\text{Gouy}}$ is negative for all values of $z$.

The fourth term arises from the intensity-dependent dipole phase acquired during the electron excursion [6, 54, 75]:

$$\Delta k_{\text{dipole}} = -\alpha_q \frac{\partial I}{\partial z} \tag{1.39}$$

The value of $\alpha_q$ depends on the quantum trajectory the electron takes during its excursion. For short trajectories, $\alpha_q = 2 \times 10^{-14}$ cm$^2$/W and for long trajectories, $\alpha_q = 22 \times 10^{-14}$ cm$^2$/W [5, 43]. The sign of $\Delta k_{\text{dipole}}$ is positive (negative) if the gas source is located upstream (downstream) of the focus.

Experimentally, the phase matching can be adjusted by tuning the laser parameters (wavelength $\lambda$, intensity $I$, pulse duration, focal spot size $w_0$), the gas species ($I_p, n$ and $k$) and interaction pressure $P$, and the gas location relative to the laser focus ($z$). Additionally, a variable aperture (iris) located just before the generation lens effectively tunes multiple laser parameters simultaneously, and is known colloquially as "the magic iris trick" [44]. Because $\Delta k$ is dependent on the harmonic order $q$, it is impossible to perfectly phase match the entire harmonic spectrum simultaneously. As a result, we adjust the phase matching parameters to optimize the useful part of the harmonic spectrum, usually at the expense of the rest of the spectrum.

Also note that the dispersive terms phase can be controlled by tuning the interaction pressure $p$, while the other terms are (to first order) pressure independent. If we place the gas medium at the focus, $\Delta k_{\text{dipole}} = 0$, and $\Delta k_{\text{Gouy}} = -(q-1)\lambda/(\pi w_0^2)$. In this case, the condition $\Delta k = 0$ can be met by setting to the density to the *optimal phase matching*

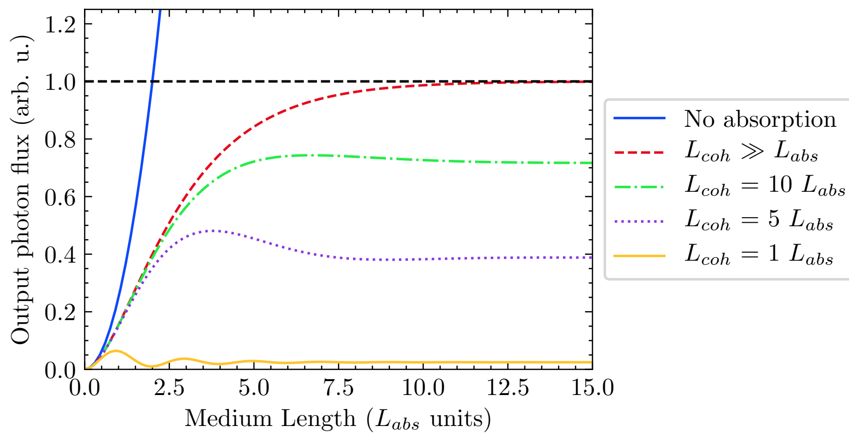


Figure 1.7: 1D absorption model from Eq. (1.42).

*density* $\rho_{\text{opt}}$ [74]:

$$\frac{\rho_{\text{opt}}}{\rho_0} = \left(\frac{q-1}{q}\right) \frac{2\lambda^2}{\Delta n w_0^2 \left(1 - \frac{\eta}{\eta_c}\right)} \tag{1.40}$$

We therefore arrive at the conclusion that the optimal phase matching density scales with the square of the fundamental wavelength. Furthermore, tighter focusing ($w_0 \to 0$) and higher ionization fractions ($\eta \to \eta_c$) require higher densities to achieve good phase matching. Therefore, creating bright harmonics from a long wavelength, relatively weak pulse requires significantly higher interaction pressures than a loosely focused 800 nm pulse. This is the motivation for designing a vacuum system and gas source that can deliver high interaction pressures (see Section 3.2).

### XUV Reabsorption

We now consider the effects of XUV absorption on the phase matching process using the 1-dimension model introduced by Constant et. al. [19]. In doing so, we restrict ourselves to the on-axis emission of the $q^{\text{th}}$ harmonic. That is, we consider only harmonics with a wave vector $k_q$ that is collinear to the fundamental ($k_0$). In this case, the number of photons emitted per unit time and area is:

$$N_{\text{out}} = \frac{\omega_q}{4c\epsilon_0\hbar} \left| \left[ \int_0^{L_{\text{med}}} \mathrm{d}z\, \rho(z) A_q(z) \exp\left(-\frac{L_{\text{med}} - z}{2L_{\text{abs}}}\right) \exp\left(i\varphi_q(z)\right) \right] \right|^2 \tag{1.41}$$

Here, $\rho(z)$ is the gas medium density, $A_q(z)$ is the amplitude of the harmonic response at frequency $\omega_q$ and $\varphi_q$ is its phase at the exit of the medium, which has length $L_{\text{med}}$. If we are using a loose focusing geometry, then the gas density and harmonic response amplitude are constant along the interaction volume: $\rho(z) = \rho$ and $A_q(z) = A_q$. With this restriction, Eq. (1.41) evaluates to:

$$N_{\text{out}} = \rho^2 A_q^2 \frac{4L_{\text{abs}}^2}{1+4\pi^2(L_{\text{abs}}^2/L_{\text{coh}}^2)}\left[1+\exp\left(-\frac{L_{\text{med}}}{L_{\text{abs}}}\right) - 2\exp\left(\frac{\pi L_{\text{med}}}{L_{\text{coh}}}\right)\exp\left(-\frac{L_{\text{med}}}{2L_{\text{abs}}}\right)\right] \tag{1.42}$$

Here, we use the notation $L_{\text{coh}} = \pi/\Delta k$ for the coherence length ($\Delta k = k_q - qk_0$) and $L_{\text{abs}} = 1/\sigma\rho$ for the absorption length.

Eq. (1.42) is plotted in Fig. 1.7. In the limit of good phase matching ($L_{\text{coh}} \gg L_{\text{abs}}$), short interaction length ($L_{\text{coh}} \gg L_{\text{med}}$) and low absorption ($L_{\text{med}} \gg L_{\text{abs}}$) the harmonic yield scales as [84]:

$$N_{\text{out}} \sim A_q^2 z_0(\rho L_{\text{med}})^2 \sim S_{\text{spot}}(PL_{\text{med}})^2 \tag{1.43}$$

where $z_0 = \pi w_0^2/\lambda_1$ is the Rayleigh length and $S_{\text{spot}} = \pi w_0^2$ is the spot area at the focus. In this limit, the photon yield is proportional to the square of the pressure-length product. Otherwise, the optimized conditions are $L_{\text{med}} > 3L_{\text{abs}}$ and $L_{\text{coh}} > 5L_{\text{abs}}$.

The dipole strength is assumed to follow $A_q \sim (1-\eta)I_0^5$, where $I_0$ is the intensity at the focus [48, 49].

Experimentally, $L_{\text{med}}$ is fixed by the geometry of the gas source, $L_{\text{abs}}$ is directly controlled by adjusting the backing pressure, and $L_{\text{coh}}$ is indirectly controlled by other parameters (gas source position relative to focus, focusing conditions, iris diameter, etc.). In Section 3.2, we will apply this simple model to the gas sources available in our lab to maximize our HHG yield.

**to do:**

now, find out where you are on this plot for the different gas cell geometries. that is, free jet, LPC and HPC have set medium lengths. given their pressure performance, you can calculate the range of interaction pressures achievable by each HHG source, and therefore you can calculate the Labs for a specific generating gas (Ar, for example). having done that, you know the Labs and the Lmed, so you know the x-axis position. you still don't know the coherence length, but it's a start.

motivation: in the LPC, we can't see pressure rollover. this plot helps show why. (assuming the LPC and the free jet are still on the rising edge of the curves). this plot explains why.

talk about choice of generating gas (He vs Ar) in terms of critical ionization fraction and Ip, as well as cross section $A_q$. He, with its low reabsorption, is great for showing interaction pressure scaling, and you can blast it with lots of 800 nm intensity. but overall it has a lower yield than argon b/c of the cross section. Ar performs poorly at 800 nm b/c of the cooper minimum; at longer wavelengths the cutoff extends past the cooper minimum and Ar is a good choice.

# Chapter 2
# Experimental Apparatus

## 2.1 Introduction

There are several major components of our experimental apparatus: the laser system, the vacuum system, the XUV-IR optics and interferometer, the target chamber and the XUV detector. Many of these subsystems were designed as improvements upon previously available equipment in the DiMauro lab, so comparisons will be made when applicable.

The laser system is the linchpin of our experiment. Its short mid-infrared pulse allows us generate XUV light via an extremely nonlinear process, photoexcite the sample and ultimately probe ultrafast dynamics in the samples. The pointing, power, and pulse duration stability of the laser system enables us to perform these sensitive experiments over extended periods of time. Details of the laser system and the general laboratory layout are discussed in Section 2.2.

XUV light cannot propagate in air. Therefore, much of the experiment is performed under high vacuum using a home-built vacuum apparatus, as shown in Figs. 2.9 and 2.10. Details of the vacuum system are discussed in Section 2.3.

After high harmonic generation, the XUV light needs to be spatially and spectrally manipulated before it can be used in our experiment. Most materials absorb strongly in this energy range, so special XUV optics are used for this purpose. Details of the XUV optics, along with a description of the XUV-IR interferometer, are discussed in Section 2.4.

The XUV light is focused on our sample in a target chamber, and the transmitted light is detected by a home-built XUV photon spectrometer. A brief overview of these systems can be found in Section 2.6. A detailed description can be found in Stephen Hageman's dissertation [34].

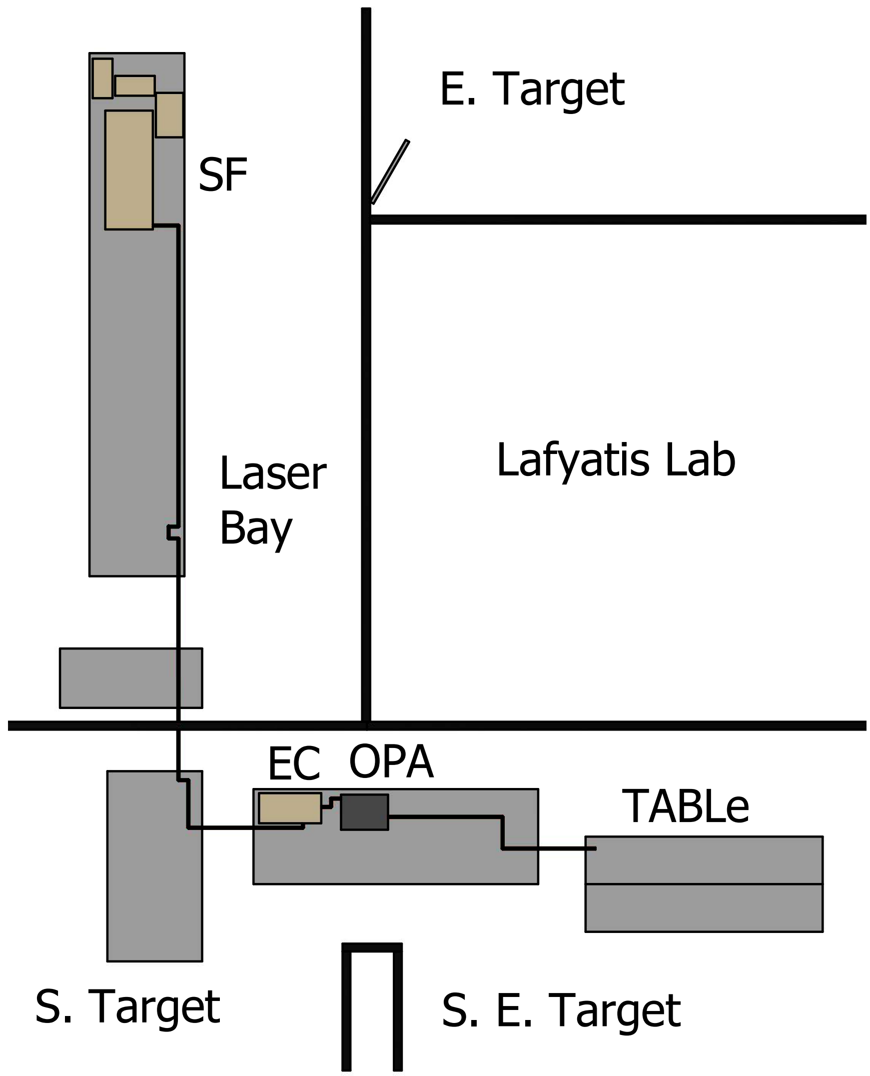


Figure 2.1: Block diagram of part of the DiMauro lab complex showing the laser path from the laser bay to the southeast target room. Other experiments and laser systems are ommitted for visual clarity. Optical tables are represented as gray boxes. SF: Spitfire laser system consisting of a MaiTai oscillator, two Empower pump lasers, interal stretcher, amplifier & internal compressor (bypassed for this experiment); EC: Spitfire external compressor; OPA: Light Conversion HE TOPAS Prime; TABLe: $4' \times 10'$ optical table for the transient absorption beamline.

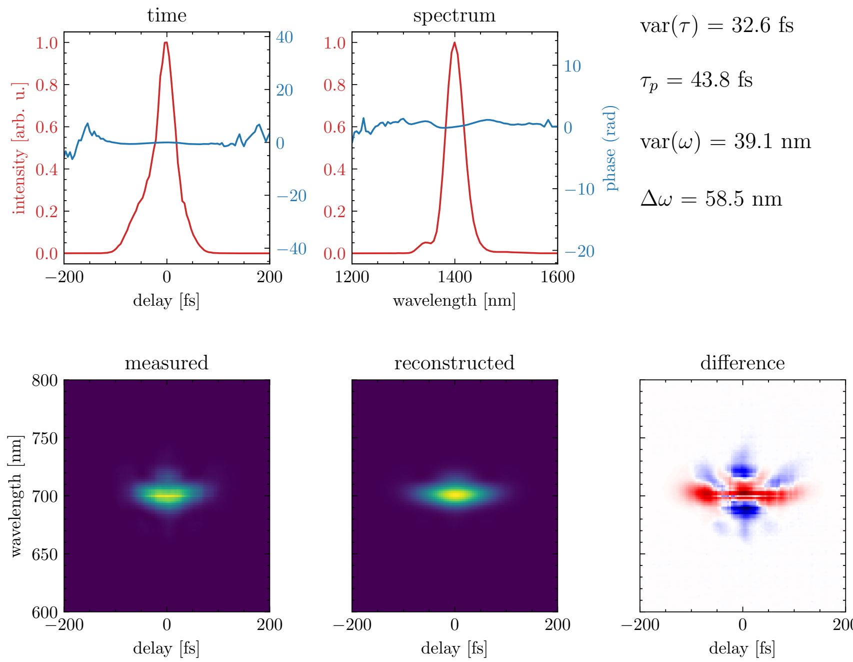


Figure 2.2: FROG analysis of the signal output of the TOPAS ($\lambda = 1400$ nm).

## 2.2 Laser System

### 2.2.1 Spitfire and TOPAS

We use a commercial mid-IR laser system (Spectra Physics Spitfire ACE), which delivers 12 mJ of 800 nm light at a variable $100 - 1,000$ Hz repetition rate with a 60 fs FMHM pulse duration. This system utilizes the chirped pulse amplification (CPA) technique to amplify the pulse energy from a weak seed pulse. In this scheme, a low energy femtosecond seed pulse is stretched in time, amplified and compressed [83]. As such, the Spitfire consists of an oscillator, a grating stretcher, a regenerative amplifier, a single-pass amplifier and a grating compressor.

The laboratory layout is shown in Fig. 2.1. All of the lasers in the DiMauro research group are located in a centralized laser bay, where walking traffic is kept to a minimum and air quality is nominally higher than the surrounding laboratory areas. This minimizes air disturbances around the laser systems and reduces the accumulation of dirt and debris on their optics. Experiments are performed in the adjacent target rooms which contain the vacuum systems and other experimental equipment. The Spitfire shares the laser bay with two home-built ultrafast laser systems (the “2 micron system” and the “4 micron system”, not shown in Fig. 2.1), as well as some laser development. The Spitfire is positioned so that its light can be directed to either the East, South or Southeast Target Rooms, depending on the needs of the researchers. To reduce air currents, welding curtains surround each optical table in the laser bay. When propagating the beam to target rooms, the beam path is enclosed in PVC tubing to reduce air curtains and to increase user safety. A $CaF_2$ window is used to block air currents between the laser bay and the target rooms.

Referring to Fig. 2.1, the transient absorption beamline (TABLe) is located in the south-east target room. Laser light from the amplifier must be propagated uncompressed to the target room to avoid nonlinear propagation effects. To understand why we can compute the $B$ integral, which provides a measure of the nonlinear phase accumulated during propagation:

$$B = \frac{2\pi}{\lambda} \int n_2 I(z)\; dz \tag{2.1}$$

The distance between the amplifier and the south target room is approximately 13 meters. For a propagation distance of 13 meters, a beam radius of 0.8 cm, a pulse energy of 12 mJ and a FWHM pulse duration of 60 fs, $B = 1.53$, which indicates that nonlinear propagation effects are significant [91]. On the other hand, the uncompressed pulse has slightly higher pulse energy (15 mJ, owing to the 20% transmission losses of the compressor), but a significantly longer pulse duration ($\sim 10^3$ longer), resulting in a negligible $B$ value. For this reason, we use an external compressor centrally located between the south and south east target rooms, as shown in Fig. 2.1. This positioning allows the Spitfire to be used for either the TABLe in the southeast target room or the RABBITT apparatus [16, 31, 46] in the south target room (not shown in Fig. 2.1). The external compressor has an efficiency of 80%, giving us 12 mJ of 800 nm light with a FWHM pulse duration of 60 fs at the entrance of the OPA.

The output of the external compressor is sent into a commercial optical parametric amplifier (Light Conversion HE TOPAS Prime), which converts the 800 nm light to longer wavelengths ranging from 1.2 to 2.2 $\mu$m while roughly maintaining pulse duration. To minimize nonlinear propagation effects, the TOPAS is located immediately after the external compressor with only two steering mirrors between the external compressor and the TOPAS. Details of the TOPAS operation, alignment and optimization can be found in the user manual. Briefly, it utilizes a nonlinear process called optical parametric amplification (OPA), where the 800 nm pump ($p$) is converted into two longer wavelength photons (the signal $s$ and the idler $i$) that obey the following energy conservation relation:

$$\frac{1}{\lambda_p} = \frac{1}{\lambda_s} + \frac{1}{\lambda_i} \tag{2.2}$$

Inside the TOPAS, a white light generation process creates a broadband seed pulse, followed by three stages of amplification in BBO crystals. The signal $\lambda_s$ and idler $\lambda_i$ wavelengths are determined by phase matching conditions inside the nonlinear crystals, which is controlled by setting the crystal angle relative to the incident laser light. The BBO crystals are mounted on encoded motorized stages, and the entire system is computer controlled and calibrated so the crystal angles change when the user specifies the desired wavelength. The conversion efficiency of the TOPAS ranges from 40 to 50 % (combined signal + idler pulse energy of 5 - 6 mJ), depending on the degree of optical alignment into the TOPAS and the desired wavelength. During the amplification process, all three beams are collinear. After the final amplification stage, a dichroic mirror inside the TOPAS separates the depleted 800 nm pump from the signal + idler, and a wavelength separator immediately outside the TOPAS splits the signal from the idler.

We use the *frequency resolved optical gating* (FROG) technique to measure the pulse duration of the TOPAS [41]. The result is shown in Fig. 2.2. At 1400 nm, we measure a pulse width (defined via the intensity FWHM) of $\tau_p = 43.8$ fs and a pulse bandwidth (defined as the spectral intensity FWHM) of $\Delta\omega = 58.5$ nm.

The interaction pulse duration used in experiments is longer than this measured quantity, as several chromatic optics in each arm of the interferometer add GDD to the pulse. In the generation arm, there are 3 lenses and a $CaF_2$ window. In the pump arm, the pulse travels through the delay wedges (approximately 2 mm of fused silica), two BK-7 lenses (7 mm total thickness), and a 3 mm thick $CaF_2$ vacuum window. Assuming a transform-limited pulse, if the initial pulse duration is $\tau_0$, then the group delay dispersion (GDD) of these optics increases the pulse duration to $\tau$ [22]:

$$\tau = \tau_0 \sqrt{1 + \left(4 \ln 2 \frac{GDD}{\tau_0^2}\right)^2} \approx 4 \ln 2 \frac{GDD}{\tau_0} \tag{2.3}$$

For the pump arm, Eq. (2.3) evaluates to $\tau = 63.7$ fs for an initial pulse duration of $\tau_0 = 43.8$ fs. The pulse duration of the generation interaction region is similar.

### 2.2.2 Active Pointing Correction Systems

As a nonlinear device, the performance of the TOPAS is extremely sensitive to input pointing, laser pulse parameters and laboratory environmental conditions. The large optical path length ($\approx 15.5$ m) between the amplifier and the TOPAS puts stringent requirements on the angular tolerances of the amplifier's output pointing. According to the specification sheet, the rms beam pointing stability of the amplifier at constant temperature is $< 5$ $\mu$rad ($\approx 75$ $\mu$m at 15.5 m) at constant temperature, which is sufficient for our purposes. Unfortunately, the temperature in the laser bay varies significantly throughout the day – sometimes by several degrees – as a function of the occupancy of the physics research building, building-wide energy conservation measures, and activity within the laser bay. Under these conditions, the amplifier's pointing changes by up to 20 $\mu$rad/°C (= 310 $\mu$m/°C at 15.5 m).

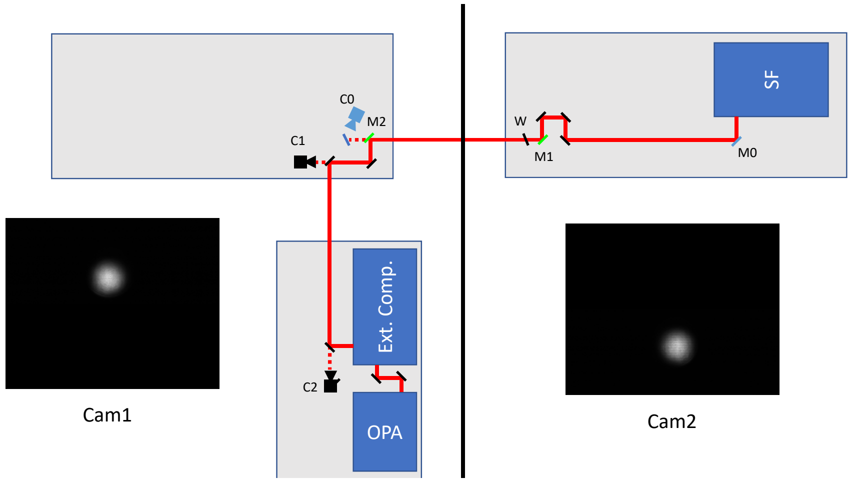


Figure 2.3: Implementation of active stabilization systems between the amplifier in the laser bay and external compressor in the target room (not to scale). M0 & C0 are the motorized mirror and digital camera used for the single-point correction scheme. M1, M2, C1 & C2 are the motorized mirrors and cameras used for the two-point correction scheme. W is an uncoated $CaF_2$ window used to reduce air currents between the laser bay and target rooms. PVC tubes that surround the beam path are omitted for visual clarity. Inset images show the attenuated beam as imaged by C1 & C2.

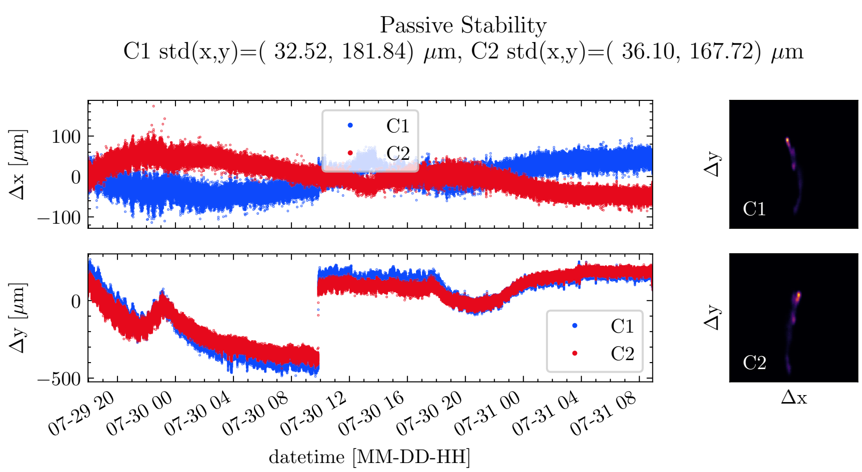


Figure 2.4: Typical passive pointing stability of the Spitfire's amplifier as measured on cameras C1 & C2. Left panels: $x$ and $y$ coordinates of the centroid vs. time; right panels: 2D histogram of beam centroid positions for the same time period. The 2-point correction scheme was activated between 09:00 (9 am) and 17:00 (5 pm) on 07-30; this system is responsible for the stable performance in the middle in the plot. Long term thermal drift is apparent at all other times.

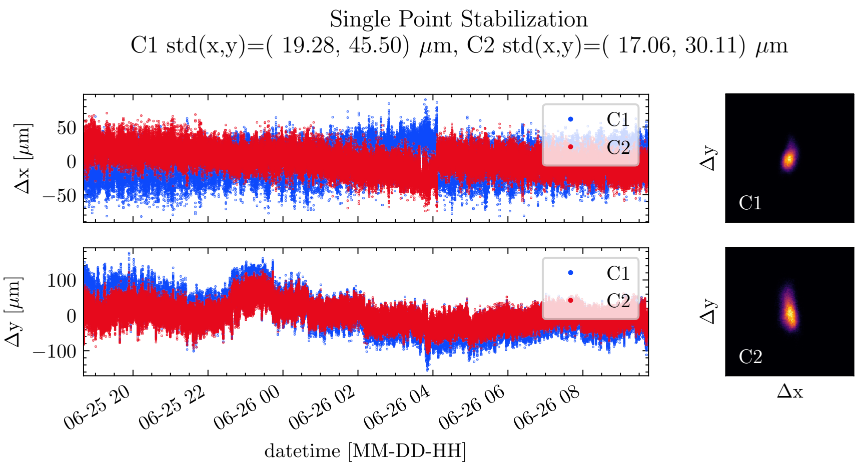


Figure 2.5: Single-point stabilization of the Spitfire's amplifier as measured on cameras C1 & C2. This dataset contains about 10 correction events, which are visible as abrupt jumps in the time series. The skew of the centroid distributions highlights the limitations of the single-point correction scheme.

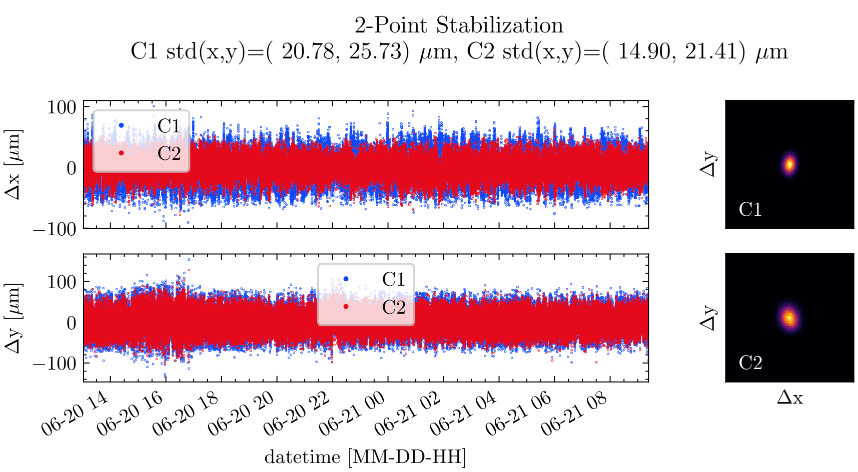


Figure 2.6: Two-point stabilization of the Spitfire's amplifier as measured on cameras C1 & C2.

To combat this slow pointing drift, we actively stabilize the beam pointing between the amplifier and the external compressor as shown in Fig. 2.3. Note that there is not enough space to implement a pointing solution between the external compressor and the TOPAS. Over the years, we have used both a home-built single-point correction scheme and a commercial two-point correction scheme.

Fig. 2.4 shows the passive pointing stability of the amplifier as measured by cameras C1 & C2 over the course of 28 hours. The left panel shows the $x$ and $y$ coordinates of the centroid (expressed as a deviation from the average position) sampled at 2 Hz. Note that the sign of $\Delta x$ is reversed between C1 and C2; this is an artifact of the camera geometry; otherwise the data from the two cameras is self-consistent. The thermal drift is most apparent in the vertical direction; from midnight to 9 am the beam drifts vertically nearly 500 $\mu$m. Between 9 am and 5 pm we activated the two-point stabilization system (described below), which accounts for the good performance during this time period. At 5 pm, the stabilization system was turned off and the slow drift resumes. The right panels show 2D histograms of the centroid position, calculated from the time series data. From these plots, it is apparent that the laser drifts in a large arc pattern, with the primary deviation occuring in the vertical direction.

The single-point correction system was programmed and implemented by Dietrich Kiesewetter, who was a graduate student at the time [46]. In this scheme, a digital camera (C0 in Fig. 2.3) located approximately 7.8 m after the amplifier monitors the transmitted light of a high reflective mirror incident on a card. The position of the centroid is calculated on a rolling average basis and compared to a saved set point. When the centroid position deviates from the set point by more than a minimum correction size, a correction signal is sent to a motorized mirror (M0, located 33 cm after the amplifier). The minimum correction size is set by the user to avoid frequent small corrections to the beam, which results in high-frequency pointing jitter. The correction time interval is also user-adjustable, with typical values of 1 - 60 seconds. If the correction signal requires too large of a step, or if the integrated intensity of the beam falls below a set value, then the locking algorithm assumes that something is wrong and breaks the correction loop without taking corrective action. This prevents the system from taking corrective action in the event the beam is partially blocked by a third party.

The performance of the single-point stabilization system as reported by cameras C1 & C2 is shown in Fig. 2.5. Here, we can see the limitations of a single-point correction scheme. The system is very good at maintaining the position of the beam at C0, but it has no control over the pointing of the beam. As a result, the beam centroid continues to drift on downstream optics, albeit with reduced magnitude compared to the uncorrected case. This is effect is apparent in the skewed 2D histograms in Fig. 2.5. The single-point stabilization system works well over short periods of time, but its geometry neccessitates weekly realignment of the external compressor and all other downstream optics. Given the technical demands of our experiments and the sensitivity of the TOPAS to input pointing, this can be a prohibitively time consuming process. Unlike a single-point correction system, a two-point system only needs to be set once.

For the two-point stabilization system, a commercial system was chosen over a home-built solution to reduce the development and implementation time. We use a Newport GuideStar II, which utilizes two cameras (C1 & C2 in Fig. 2.3) and two motorized mirrors (M1 & M2) to monitor the beam centroid and make corrections. A patented correction algorithm running on purpose-built computational hardware is applied to the output of the cameras to solve for the neccessary correction signals up to 3 times per second [26]. Beam pointing is usually recovered with a single corrective action, and even especially large pointing drifts are corrected well within 1 second. For numerical stability and increased sensitivity, the distance between M1 and M2 is made as large as possible (3.1 meters); the distance between C1 and C2 (1.75 meters) is also maximized and made similiar to the M1-M2 distance; the distance between C1 and M2 is made as small as possible (75 cm).

The passive and actively-controlled pointing stability of the amplifier is shown in Fig. 2.6. Owing to the high correction frequency, individual corrections are small and not visible in the time series. The two-point system maintains both the centroid position and propagation direction, so there is minimal correlation between the reported centroid positions on C1 & C2. As a result, the pointing into the TOPAS rarely needs to be optimized under normal operation, saving valuable time and making experiments more repeatable.

The GuideStar II performs extremely well, but its software lacks the safety features of our home-built system. Specifically, there is no maximum allowable correction size, intensity or beam mode quality monitoring to prevent run-away corrections. For example, it is common to insert a paper card into the beam path to inspect the beam mode just before the external compressor. As a result, camera C2 will briefly see a partially clipped beam with a centroid displaced by approximately the beam radius, and the GuideStar will take *immediate corrective actions* to adjust the pointing. These actions may result in a 15 mJ beam pointing in an unsafe direction. **Users are cautioned to keep clear of the beam path between the amplifier and the GuideStar cameras when the GuideStar locking algorithm is enabled.** To mitigate this issue, the GuideStar cameras are kept in a plastic enclosure and colleagues are made aware of the limitations of the GuideStar system.

**say something about the 2photon photodiode in the external compressor**

### 2.2.3 Beam routing into the TABLe interferometer

After selecting the wavelength (signal, idler or depleted pump), the output of the TOPAS is sent approximately 3 meters downsteam to the transient absorption optical table. Two

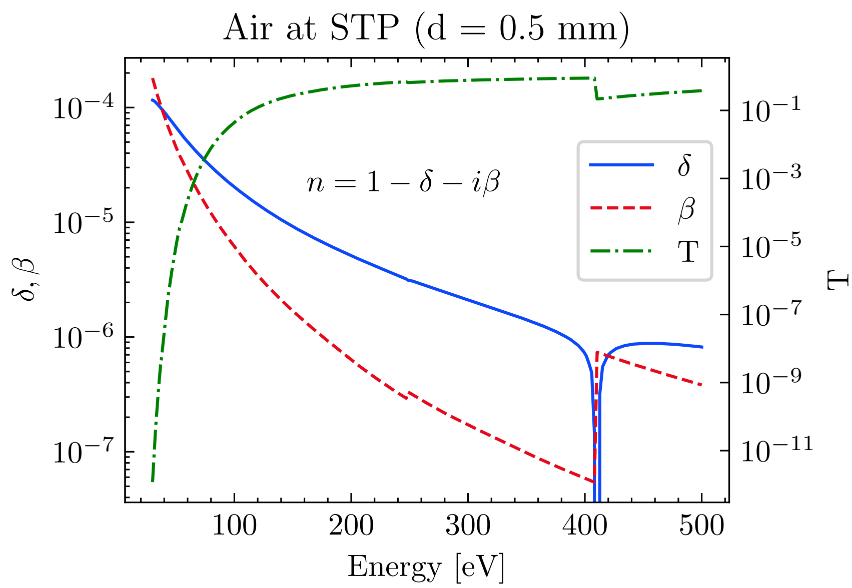


Figure 2.7: Estimation of XUV propagation losses through 0.5 mm of air at STP. Atomic scattering data obtained from [32, 36]. Calculation follows Eqs. (2.4) to (2.6).

motorized mirrors on the TOPAS optical table are used to align the laser into the TABLe interferometer. Unless otherwise noted, protected silver mirrors are used to propagate the TOPAS light for their broadband reflectivity, low absorption losses and high corrosion resistance.

## 2.3 Vacuum System

### 2.3.1 The Need for High Vacuum

The XUV light generated by the high harmonic process is absorbed strongly by air, as most gases have at least one electronic transition in the XUV regime. The magnitude of absorption can be estimated using the atomic scattering factors $f = f_1 + if_2$, which were taken from [36]. The photoabsorption cross section $\mu_a$, the transmission ratio $T$, and the complex index of refraction $\hat{n}$ of a gas can be calculated from these factors:

$$\mu_a = 2r_0\lambda f_2 \tag{2.4}$$

$$T = \exp\left(-N\mu_a d\right) \tag{2.5}$$

$$\hat{n} = 1 - \frac{1}{2\pi}Nr_0\lambda^2\left(f_1 + if_2\right) \tag{2.6}$$

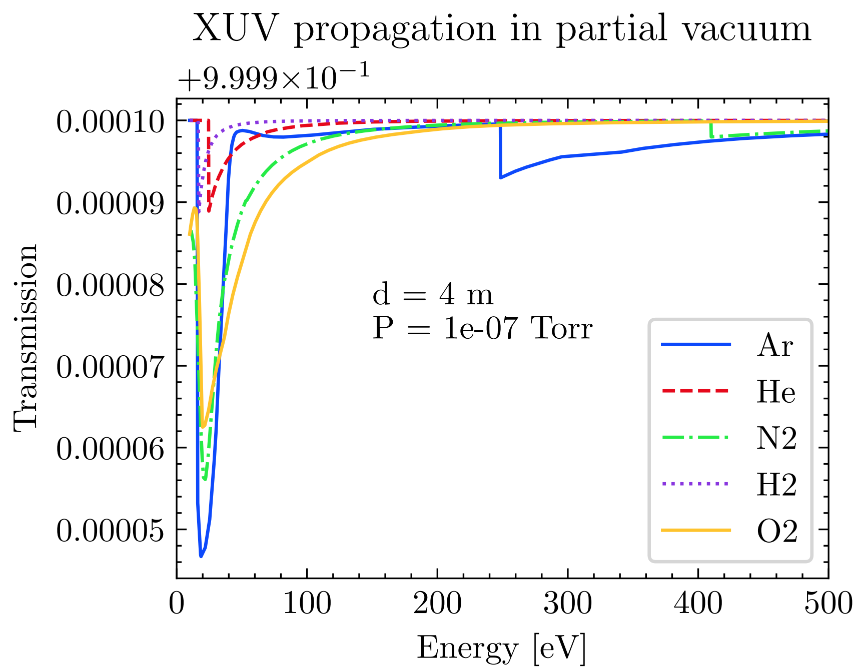


Figure 2.8: Estimation of XUV propagation losses through a vacuum level of $10^{-7}$ Torr and a distance of 4 meters. Transmission is well over 99.999% for this pressure-length product. Atomic scattering data obtained from [32, 36]. Calculation follows Eqs. (2.4) to (2.6).

In the above equations, $\lambda$ is the photon wavelength, $N$ is the number of atoms per unit volume, $d$ is the optical path length and $r_0 = 2.8179403227(19) \times 10^{-6}$ nm is the classical electron radius. The results for air at standard temperature and pressure are shown in Fig. 2.7. From this figure it is apparent that any XUV light we generate will be effectively attenuated to zero in less than 1 millimeter if the beam is propagated in air.

For reference, the XUV portion of the transient absorption beamline is about 4 meters long. Fig. 2.8 shows the expected XUV transmission losses for XUV propagation through a partial vacuum of common gases: argon and helium are often used for generation, while nitrogen, hydrogen and oxygen are common UHV system contaminants. From this figure, we can see that the XUV transmission exceeds 99.99% for an average pressure of $10^{-7}$ Torr. Note that this calculation does not include reflection losses from the ellipsoidal mirror, transmission losses from the metallic filter or the sample, or geometric losses from clipping. This simple analysis tells us that the XUV portion of the beamline must be kept under relatively high vacuum to avoid needlessly reducing the XUV flux.

The microchannel plate (MCP) assembly in the photon spectrometer (see Section 2.6) puts additional constraints on the vacuum level. Contaminants in the spectrometer chamber (originating from a finite chamber pressure) lower the effective electrical resistance between the highly charged plates, resulting in a somewhat periodic current surge between the plates. This effect manifests itself in the data as a bright point source at a random location on the detector. In addition to reducing the fidelity of the data, each current surge counts towards the lifetime limit of the MCP assembly, reducing its lifetime [50].

The low pressure condition required to minimize XUV absorption and instrumentation malfunction is in direct conflict with the requirements for high harmonic generation (HHG) and gas-phase attosecond transient absorption spectroscopy (ATAS) experiments. HHG requires a gas source to be placed near the IR focus in the generation chamber, and a gas-phase ATAS experiment requires a similar gas source to be placed near the XUV/IR focus in the target chamber. The gas from these sources will diffuse into neighboring chambers, raising the pressure of the entire beamline. In addition to the complications described above, higher pressures can overwhelm and damage the turbomolecular vacuum pumps used to keep the system at high vacuum. The vacuum apparatus was designed to localize the gas density at the interaction regions while allowing a range of optical configurations to be used.

### 2.3.2 Design Goals

The vacuum system was designed to be as modular as possible. In this sense, the TABLe apparatus can be thought of a permanently installed XUV light source & XUV-IR interferometer that has the ability to accept modular end stations. This design priniciple has already allowed the study of electron rescattering in strong infrared fields by another graduate student [46]; going forward, new target chambers can be designed to meet the needs of future experiments while maintaining the integrity of the XUV light source and interferometer.

We employ magnetically levitated turbomolecular pumps which were not commercially available at the time of the RABBITT apparatus' construction. These pumps are designed so that the vacuum side of the blade assembly does not make mechanical contact with the drive shaft and housing, which dramatically reduces vibrations during operation. Maglev turbopumps have a noise power spectrum an order of magnitude smaller than that of traditional turbopumps. This ultra-quiet operation allows us to mount the vacuum hardware directly on the interferometer's optical table. Likewise, we keep our rough vacuum system in an adacent pump room to minimize acoustics, vibrations and oil contamination in the target rooms.

Large vacuum chambers have the benefit of being able to accommodate a seemingly limitless amount of optics and internal hardware, but they are very uncomfortable and difficult to work around. For this reason, we tried to keep the physical size of the chambers as small as possible while still allowing sufficient internal space for our current and reasonable future equipment needs (*in vacuo* motorized stages, optics, gas and electric feedthroughs, etc.). Additionally, *in vacuo* optics are difficult to optimize. Vacuum compatible optic mounts exist, but they are expensive, cumbersome to work with and generally considered specialty items that need to be custom ordered. Adjusting a non-motorized optic requires a venting / pumping cycle, which can take several hours. Early on in the design process, we made the decision to keep as many optics as possible outside of the vacuum system, greatly reducing the overall size of the system. Excluding the modular endstations, our vacuum chambers have a footprint that is approximately one third that of the RABBITT apparatus, which leaves more than half of our $4' \times 10'$ optical table unoccupied.

### 2.3.3 Manufacturing Considerations

When we started this project, the DiMauro lab already had a working attosecond beamline: the RABBITT apparatus, located in the south target room [16]. We considered modifying this apparatus for our needs, but ultimately decided to build a second beamline. The RABBITT apparatus was being frequently used by more senior students working on projects with experimental requirements that were in conflict with those of a transient absorption experiment [31, 46]. At the minimum, we needed to build an XUV photon spectrometer and a condensed matter sample holder. We could have removed the electron spectrometer from the RABBITT apparatus and installed a condensed matter target chamber and photon spectrometer, but this would have been extremely disruptive to the rest of the group. Furthermore, the south target room was already crowded with the cluster apparatus [90], and our equipment would not fit in the room without significant modification to the existing laboratory environment. Also around the start of this project, the DiMauro lab complex was expanded by half a standard laboratory unit (one half of PRB 4115). A partial wall (about 12 feet high) was constructed in 4115, separating the Lafyatis lab from what would now be called the south east target room. Next, the wall separating the south and our half of 4115 was knocked down. The current lab layout can be seen in Fig. 2.1.

Modular aluminum vacuum chambers were not yet available on the commercial market [69], so we went with a welded design for our custom chambers. We considered both aluminum and stainless steel (SS) for the chamber material. Aluminum was preferred for our application, as it is lighter and therefore easier to mount to an optical table. Due to the presence of a natural oxide layer, aluminum chambers have difficulty reaching UHV vacuum; fortunately our experimental requirement of $10^{-7}$ Torr is well within reach of an aluminum chamber. The biggest concern of an all-aluminum chamber was the softness of an aluminum knife edge. Recalling the geometry of a conflat flange, the "knife edge" is used to form a semi-permanent metal-metal sealing surface between the conflat and a metal gasket. Any imperfections in the knife edge will result in a sub-optimal sealing surface and will leak. The concern was that an aluminum knife edge could be easily damaged while working in and around the chamber. The solution to this problem is to use SS conflats with an Al chamber body. However, Al and SS cannot be welded together using traditional welding techniques; they must be joined using a difficult technique called *explosive welding*. Few companies are able to explosively weld UHV chambers, and those that do charge a premium for their manufacturing services. A mixed-metal chamber would have been prohibitively expensive, so we decided to use an all stainless steel design.

We decided to have our custom chambers manufactured by the Physics and Astronomy Machine Shops. This allowed us to consult with the machinists frequently during the design phase, which allowed us to converge on a design that met our experimental requirements while minimized machining operations and cost. To this end, we used off-the-shelf vacuum hardware (standard vacuum crosses, full nipples, etc.) whenever possible. The physical size of the ellipsoidal mirror and the XUV spectrometer neccessitated a custom chamber design. To minimize engineering and machining complexity, we designed these chambers as simple "boxes", i.e., using plate geometry.

### 2.3.4 Vacuum System Details

In this section, we will provide a brief overview of each vacuum chamber in the TABLe vacuum system. A render of the final vacuum design is shown in Figs. 2.9 and 2.10. A cartoon of the beam path showing the beam path relative to the vacuum system is shown in Fig. 2.16.

The first half of the vacuum system (generation, differential pumping, diagnostic station, $1^{st}$ metallic filter and mirror chambers) sits atop a custom split-level 4' × 10' optical table (TMC Vibration Control). The lower deck of the table is 24" wide and 12" thick and the upper deck is 20" thick. With this design, we are able to place the vacuum chambers directly on the lower deck while keeping the beam height of the in-air components at a standard height above the upper deck of the table. Like all other optical tables in the DiMauro lab, this table is not pneumatically floated; it sits directly on a steel leg assembly. This maintains the relative position between the optical tables and allows us to put the weight of the chambers on top of the table.

The second half of the vacuum system (target, differential pumping, $2^{nd}$ metallic filter and spectrometer chambers) is not directly connected to the optical table, but instead sits on floor-mounted extruded aluminum frames. This modularity allows us to swap the endstations as dictated by experimental requirements. Although this makes these chambers less mechanically stable, this is an acceptable compromise as they are not part of the interferometer.

We use three gate valves to create four different vacuum regions in the beamline. This allows us to vent or pump down these sections independently, which is useful when trying to preserve air-sensitive components (MCP, metal filters, samples) or to minimize downtime when performing a "quick fix" that neccessitates venting a single section. All three gate

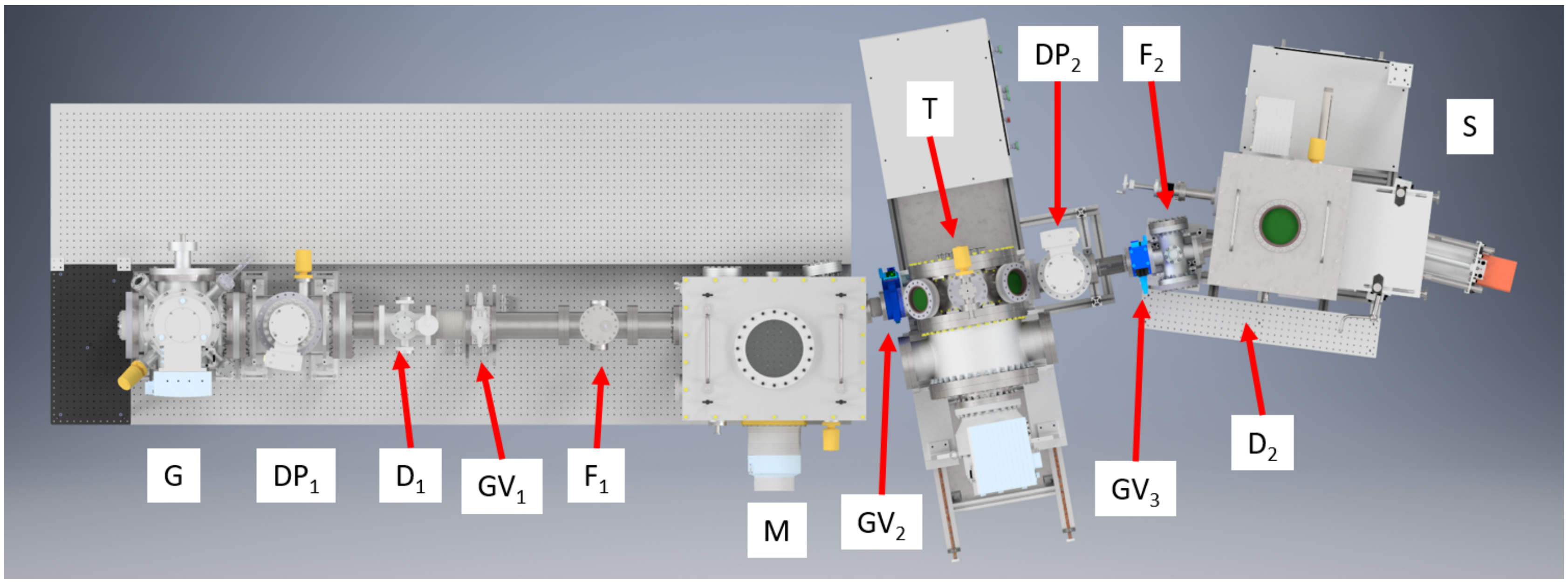


Figure 2.9: Overhead rendering of the TABLe's vacuum chambers. In-air optics are omitted for visual clarity. G: generation chamber; DP: differential pumping chamber; D: IR diagnostic station; GV: gate valve, F: metal filter; M: mirror chamber; T: target chamber; S: XUV photon spectrometer.

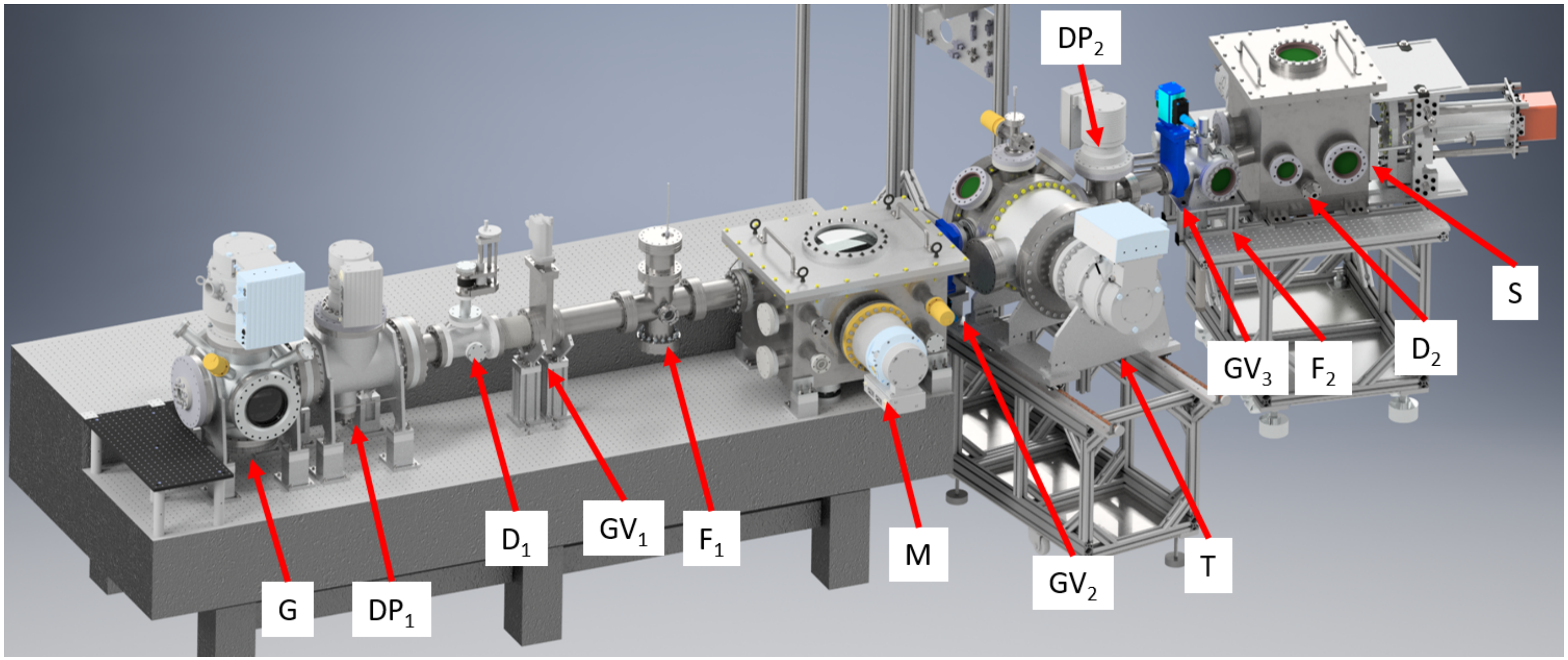


Figure 2.10: Angled rendering view of the TABLe's vacuum chambers showing the two-level 4' × 10' optical table. G: generation chamber; DP: differential pumping chamber; D: IR diagnostic station; GV: gate valve, F: metal filter; M: mirror chamber; T: target chamber; S: XUV photon spectrometer.

valves are electro-pneumatically powered so that they can be controlled via the OMRON safety system. $GV_1$ it is positioned between the IR diagnostic station and the metal filter, upstream of the ellipsoidal mirror. $GV_2$ is located between the mirror and target chambers. $GV_3$ is located between the target chamber's differential pump and the spectrometer's filter chamber. The four vacuum sections are colloquially referred to as the generation chamber, the mirror chamber, the target chamber and the spectrometer. Vacuum bellows are installed between the sections to facilitate chamber alignment.

Pressures in each chamber are monitored using a combination Pirahni / cold cathode pressure gauge (Leybold PTR90) that can read pressures from 750 Torr to $7.5 \times 10^{-9}$ Torr. Each vacuum section has a CF-to-KF adapter fitted with a blank KF flange, which is loosened while venting to prevent overpressurization of each vacuum section. The pressure in each turbo pump foreline is monitored by a thermocouple pressure gauge (Lesker KJL-6000) and analog controller.

### Generation and Differential Pump Chambers

The first chamber in the vacuum system is the *generation chamber* (G), where the XUV light is produced via HHG. Attached to this chamber and separated by a vacuum aperture is the *differential pumping chamber* ($DP_1$). The geoemtry of these two chambers localizes the high gas pressures required for HHG within the generation chamber.

The generation chamber is designed to house the HHG gas nozzle or cell, and short focal length optics. It is here that the XUV light is created for the ATAS experiments. As such, it must be large enough to house an XYZ translation stage, as well as the neccessary electric and gas line feedthroughs. The turbo pump must be large enough to maintain milliTorr or lower pressures while being subjected to large gas throughputs for the duration of an experiment. The geometry of the chamber must accommodate a range of focal lengths and optical layouts. To facilitate IR/gas nozzle alignment, there must be a clear line of sight from outside the chamber to the IR's focal spot (roughly, the center of the generation chamber).

The generation chamber is a standard 6-way 10" ConFlat (CF) cross that has been modified by the Physics Machine Shop to have four additional 2.5" CF ports. These so-called *radial ports* are positioned at the corners of the top flange and are directed towards the center of the generation chamber. The 10" CF flanges are populated as follows. A large turbo pump (Oerlikon Leybold Turbovac Mag W 1300 iP, 1300 Liter/sec) is mounted on the top 10" CF flange. The bottom flange has a 50-pin electric feedthrough and tapped holes for mounting an internal aluminum breadboard, which holds the motorized XYZ manipulation stage, gas nozzle / cell, and any focusing optics. The front flange has zero length adapter with a custom o-ring sealed optical window mount (2" diameter, 1.5" clear aperture, 3 mm thick $CaF_2$), which lets the laser light enter the chamber. A large 8" diameter viewport is mounted on the right flange, and a CF-to-KF adapting flange for the HPC (see Section 3.2.5) is mounted on the left flange. The rear flange holds the vacuum aperture assembly and a double-sided 10” CF flange, which connects to the front flange of the differential pump chamber. The 2.75” radial flanges hold a Leybold pressure gauge, a 2” diameter viewport and a 4-pipe 1/8” Swagelok gas feedthrough flange (Lesker).

The vacuum aperture assembly is modular, as it allows different sized apertures to be installed as neccessary. Currently, we use a 10 mm diameter aperture which was chosen to maximize the XUV transmission downstream. This setup yields a pressure drop of about 2 orders of magnitude across the aperture.

The differential pumping chamber is a standard 3-way 10” CF tee with two additional 2.75” CF flanges pointing towards the optical axis. The front 10” CF flange is connected to the generation chamber; the top CF 10” flange holds a small turbo pump (Oerlikon Leybold Turbovac Mag W 400 iP, 400 L/s) and the rear 10” CF flange connects to the IR diagnostic station. A KF blow-off assembly and a pressure gauge are mounted to the 2.75” CF flanges.

Typical operating pressures using a 200 $\mu$m diameter free expansion nozzle (Argon gas, $P_0 = -5$ psig backing pressure, 2.75 Torr-liter/second throughput) are about 3 mTorr in the generation chamber and $5 \times 10^{-5}$ Torr in the differential pump chamber.

#### IR Diagnostic Station

An *IR diagnostic station* ($\mathrm{D}_1$) is located after the differential pumping chamber. The diagnostic station houses a silver mirror mounted to a linear shift mechanism. When retracted, the mirror is out of the optical axis; when inserted the IR beam is diverted outside of the vacuum system through a window onto the upper deck of the split level optical table. This diagnostic station is used to measure the transmitted power of the generation arm when aligning the high pressure cell (HPC, see Section 3.2.5).

#### Filter Chamber

The generation arm’s IR light is blocked at the first spectral *filter chamber* $\mathrm{F}_1$, which is located after the diagnostic station and before the XUV mirror. This chamber houses a o-ring sealed insertable rod upon which a clamshell assembly is mounted, as shown in Fig. 2.11. This assembly was designed to hold standard metallic filters made by Luxel or Lebow, or achromatic MCP filters [93]. By changing the insertion of the rod into the chamber, the user can select which of the three filters is on the optical axis. A calibrated indicator located outside the chamber (not shown) has markings to indicate the approximate rod position for each filter. The precise height of the filter can be fine tuned while observing the spatial profile of the XUV beam, as reported by the XUV spectrometer. Note that using a mesh-supported filter will imprint a grid-like pattern into the XUV beam, which

Figure 2.11: Rendering of the metallic filter assembly in the spectral filter chamber. Metallic filters are shown with a false green color for visual clarity.

will be apparent in the spectrometer's readings. Retracting the rod fully allows the XUV-IR beam to continue down the beamline unattenuated. Users should are cautioned that unattenuated IR light from the generation arm will destroy condensed matter samples in the target chamber.

### Mirror Chamber

The *mirror chamber* (M) is located after the filter chamber at the end of the 4' × 10' optical table. This chamber houses the ellipsoidal and hole mirrors (discussed in Section 2.4). The ellipsoidal mirror (EM) reimages the XUV source onto the target, while the hole mirror (HM) collinearly combines the generation arm's XUV with the pump arm's IR, closing the interferometer. The two pulses leave the chamber through the exit flange, which is angled 10 degrees to the left to account for the 85 degree incident angle of the EM.

This chamber has windowed ports (2 inch diameter, 3 mm thickness $CaF_2$) that allow for positioning of the hole mirror before or after the ellipsoidal mirror, depending on experimental requirements. If the EM precedes the HM, then the IR pump arm focal parameters can be tuned arbitrarily, but this flexibility comes at the cost of having an additional optic in the interferometer. If the HM precedes the EM, then both the XUV and the IR pump

Figure 2.12: Photograph of the underside of the mirror chamber during installation showing the vibration-dampening bellows. Steel rods (not visible) connect the interior of the bellows feet to the interior breadboard. After installation, the flat metal disks were secured to the optical table using clamps.

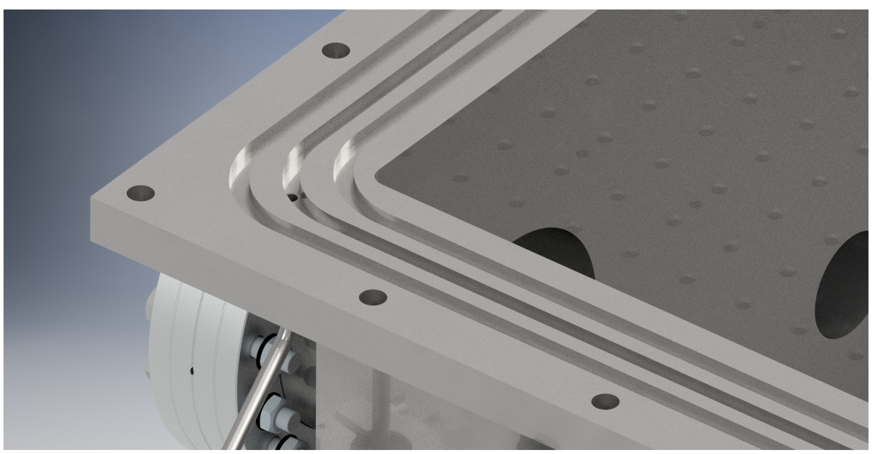

Figure 2.13: Rendering of the mirror chamber's sealing surface showing detail of the differentially pumped double o-ring. O-rings are not shown in this figure. The two o-ring glands, the central pumping channel and the welded 1/4" stainless steel pumping tube are visible. Four through holes for the 5/16" sealing bolts are visible at the perimeter of the chamber's sealing surface.

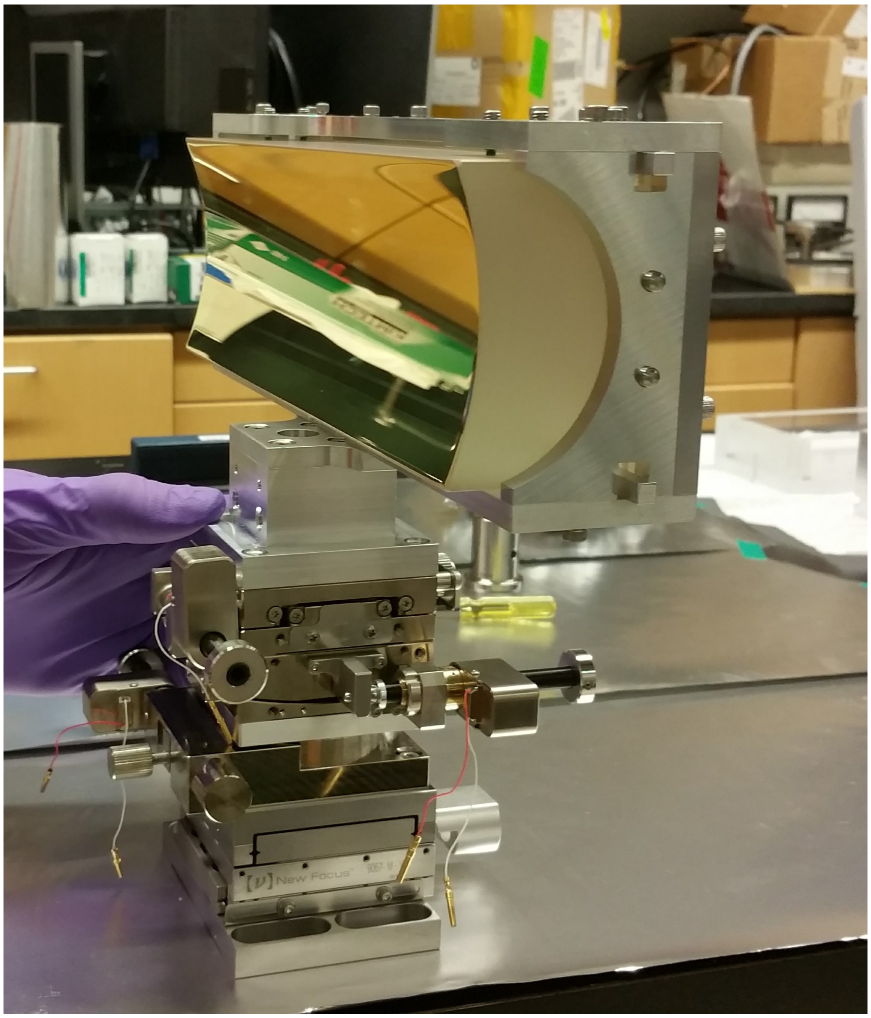


Figure 2.14: Photograph of the ellipsoidal mirror in its motorization stack prior to being installed in the mirror chamber. See text for details.

share a common focusing optic which is outside the interferometer, which can improve interferometric stability.

An internal reinforced aluminum breadboard supports the optomechanical components within the chamber. This breadboard is mechanically coupled directly to the 4' $\times$ 10' optical table using four stainless steel columns that run through openings on the underside of the mirror chamber, as shown in Fig. 2.12. Each port has a soft bellows housing that isolates chamber vibrations (originating from the pumping system) from the interferometrically stable optics within the chamber.

It is important to have remote *in vacuo* control of both the EM and the HM, as the final alignment must be done with the XUV light. The optomechanical support of the ellipsoidal mirror was designed to avoid the cantilevering present in the XUV mirror of the RABBITT apparatus, which eliminates a source of mechanical instability. This required the use of custom vacuum compatible stages and spacers. To this end, the ellipsoidal mirror is placed atop a 5-axis vacuum compatible motorized stack, as shown in Fig. 2.14. Starting from the breadboard, we have an XY crossed-roller bearing stage assembly (Newport) actuated by encoded stepper motors (Thorlabs). Next, a rotation stage (OptoSigma KSPS-606M-EN-N-2) controls the yaw. A matched pair of custom goniometers (OptoSigma, 85 & 105 mm radii) with a center of rotation corresponding to the optical center of the ellipsoidal mirror, control the roll and pitch of the EM. All three rotations are actuated by picomotors (Newport 8301-UHV). An aluminum bracket, constructed of 7075 aluminum and manufactured by the Physics Machine Shop, surrounds the optically inactive sides of the ellipsoidal mirror and secures it to the top of the optomechanical stack. The height of the ellipsoidal mirror is fixed by the combined height of the breadboard, optomechanical stack and aluminum bracket.

The hole mirror is mounted in 2 inch diameter gimballed beamsplitter holder (OptoSigma BHAN-50M-8-32UNC), modified to work with a pair of picomotors (Newport 8301-UHV) and to be vacuum compatible. This mount was chosen as it has a large clear aperture in both transmission and reflection at 45 degrees. This capability allows for the future implementation of an active interferometric control arm using a visible wavelength. Two extra 4.5" CF ports are available for a future implementation of this control system.

The interior of the mirror chamber is accessed by removing the top panel, which was constructed from aluminum to reduce the weight. Nevertheless, the lid assembly weighs about 66 lbs (30 kg), so a manual winch was installed above the chamber so that any members of the group could remove the lid if neccessary. When installed, the lid is sealed to the chamber body by use of a differentially pumped double o-ring face seal, as shown in Fig. 2.13. Three grooves are milled into the stainless steel face of the chamber for this purpose; the outer and innermost channels each hold a large o-ring, while the middle channel is continously pumped via the beamline's rough vacuum system. The rough vacuum line splits before this turbo and provides pumping speed to both the turbo (Oerlikon Leybold Turbovac Mag W 700 iP) as well as the mirror chamber's differential groove.

### Target and 2$^{\text{nd}}$ Differential Pump Chambers

The *target chamber* (T) is located immediately after the mirror chamber, with the center of the chamber roughly corresponding to the XUV focal spot (750 mm from the ellipsoidal mirror).

The chamber is an assembly of two 16" CF feedthrough collars populated with smaller radial flanges. The assembly is turned on its side so that the light enters and exits the chamber through the radial flanges.

The left collar has eight 6" CF radial flanges and serves as the interaction region. The interaction collar is mounted directly to the extruded aluminum frame (80/20 Inc.). The bottom radial flange supports an internal aluminum breadboard. The breadboard supports a motorized XYZ stage (Newport), upon which a sample holder can be attached. Encoded stepper motors (Thorlabs) are used for repeatable sample movement relative to the XUV/IR focus. The top radial port has a 6"-to-2.75" zero length reducer and a 2.75" CF tee which holds a KF blow off valve, a pressure gauge, and a gas line feedthrough for gas phase measurements. Viewports are installed on the two top diagonal radial ports. A 50-pin electrical feedthrough (Accuglass) is mounted on one of the bottom diagonal ports. The horizontal radial flanges serve as the entrance and exit ports for the light. A vacuum aperture (5 mm diameter) is mounted on the external side of the horizontal exit port to limit gas flow into the spectrometer chamber when gas phase experiments are performed. The left 16" CF flange holds a 16"-to-8" zero length adapter. Currently, this 8" port is used as an access port, but it was originally designed to accommodate an electron spectrometer to record simultaneous photon and electron measurements (not implemented).

The right collar has two 8" CF radial flanges which are used as access ports. A large turbo pump (Oerlikon Leybold Turbovac Mag W 1300 iP) is mounted via a 16"-to-10" reducing flange. The assembly was designed to be opened in the middle by breaking the 16" CF connection between the two collars. To facilitate this motion, the right collar and turbo pump are mounted to a rail system using sets of single and dual track roller bearings (Thomson).

The second differential pumping chamber ($DP_2$) is a 4.5"/6" reducing cross located immediately after the target chamber. A modified 6"-to-4.5" zero length reducing flange holds a 5 mm diameter vacuum aperture and connects the target and differential pumping chambers. This aperture size significantly reduces the IR flux and lowers the operating pressure in the photon spectrometer during gas phase measurements. An 8"-to-6" zero length reduces is used to connect a hybrid bearing turbo pump (Oerlikon Leybold Turbovac T450i) to the top of the $DP_2$ chamber.

For additional details on the target and differential chambers, see Stephen Hageman's dissertation [34].

**more detail on the sample holder (gas and condensed phase) on an XYZ stage. OR consider moving it to another section / chapter.**

### 2nd Filter and XUV Photon Spectrometer Chambers

A second filter chamber ($F_2$), is located after the target differential pumping chamber. Designed to filter out the residual IR light from the pump arm, it is very similar to the first filter chamber ($F_1$). The main difference is that we use an UHV-rated linear actuactor (Lesker LBD35-150-H) to control the filter's position in the beam, rather than an o-ring seal. This was to reduce ultimate pressure of the spectrometer chamber. The target chamber's vacuum aperture and the spatial mode from the hole mirror largely make this filter unneccesary, as most of the energy is blocked before it reaches the filter chamber.

The photon spectrometer's optics and chamber were custom built to meet our experimental needs. Stephen Hageman's dissertation [34] and Sierra O'Bryan's thesis [64] contain detailed discussions on these subsystems. Below, we provide a brief overview of the vacuum chamber and the optomechanics. For a brief overview of the photon spectrometer's optical design, see Section 2.6.

This chamber is a custom box design, with a removable lid sealed by a differential pumping groove similar to the mirror chamber. We have six-axis control over the positioning of the spectrometer's gratings. The gratings are mounted atop a 5-axis motion stack of linear, rotation and goniometric stages (Newport). The motion stack is mounted atop a linear insertion mount (Lesker LSM38-25-H), mounted on the floor of the chamber, which provides vertical translation via a manual, external control wheel.

A small turbo pump (Oerlikon Leybold Turbovac Mag W 400 iP) is mounted to the chamber wall in a horizontal configuration. An internal aluminum breadboard mounted to the floor and walls of the chamber provides support for ancillary optics, including diverting optics for external IR diagnostics. A linear actuator on the entrance wall pushes on a gearbox assembly to insert a 2" silver mirror into the beam path before the grating stack. When fully inserted, the beam is diverted out of the chamber through a viewport. An external breadboard, mounted to the chamber's extruded aluminum frame (8020 Inc.), holds IR diagnostic optics used for finding temporal overlap.

A third linear actuator mounted on the turbo pump wall inserts baffles before the XUV detector to block zero-order diffracted light. An 8" custom CF custom edge-welded bellows connects the exit chamber wall and the XUV detector flange assembly. A custom mechanical assembly (the "cage and crank" system) provides three-axis control over the detector flange (horizontal translation, separation, and angle). This system allows us to optimize the grating-detector geometry, depending on what part of the XUV spectrum we want to resolve.

**Caution:** The bellows have a limited range of motion that is smaller than the cage and crank's range. It is possible to tear the bellows by moving the system outside its safe operation range. Even with the OMRON safety system armed, a tear in the bellows while under the system is under vacuum would lead to the sudden and catastrophic venting of the entire beamline. Refer to [34] and the bellows calculator for additional details before using this system.

### Rough Vacuum Details and OMRON Safety System

The turbo pumps are backed by a pair of rough vacuum systems that are located in an adjacent pump room. A schematic of the system is shown in Fig. 2.15. The generation and differential pumping chambers share a high throughput system, and the remaining chambers (mirror, target, target differential pumping, spectrometer) share a smaller system.

The large rough pump system consists of a rotary vane (RV, Leybold D65B, 65 $m^3$/hr) and roots blower (Leybold WSU 501, 500 $m^3$/hr) pump stack. This rough vacuum system is connected to the beamline via a large diameter copper and PVC tube. The pressure at the inlet flange of the roots blower is remotely monitored using an thermocouple gauge (Agilent Type 0531 TC) an electronic gauge controller (Lesker KJL615TC-E), a wireless networking router, and a touchscreen-enabled Raspberry Pi running Lesker's web applet.

The smaller system uses the same model RV pump, but a smaller roots blower (Leybold WA 251, 250 $m^3$/hr). Although it has half the pumping speed as the generation pump stack, the gas load for these chambers is minimal compared to the generation chamber. The pressure at the inlet flange of the roots blower is remotely monitored using a copy of the system that monitors the generation roots blower pressure.

Owing to the complexity of the vacuum system, we decided to implement a "safety system", i.e., a programmable logic controller that controls the major components of the vacuum apparatus. The heart of this system is an OMRON PLC. Its design follows that of the RABBITT apparatus [16], although the new system controls significantly more equipment that its predecessor. Special thanks go to Andrew Piper [69], who programmed and implemented this system on our beamline. A full user manual is available on the group drive, and a quick start guide is available in Section A.1. In short, the OMRON safety system monitors the setpoints of the 5 UHV pressure gauges and controls the 6 turbo pumps, the 4 rough vacuum solenoid gate valves, the 3 UHV pneumatic gate valves and the 5 turbo pump solenoid vent valves according to simple set of logic rules. This automation enables three main features. First, the user can pump down or vent individual sections (or the entire beamline) with a few button presses. With the exception of actuating the manual valves and the KF blow off flanges, this process is almost entirely automated which greatly reduces the complexity of using the vacuum system. Second, the OMRON verifies that

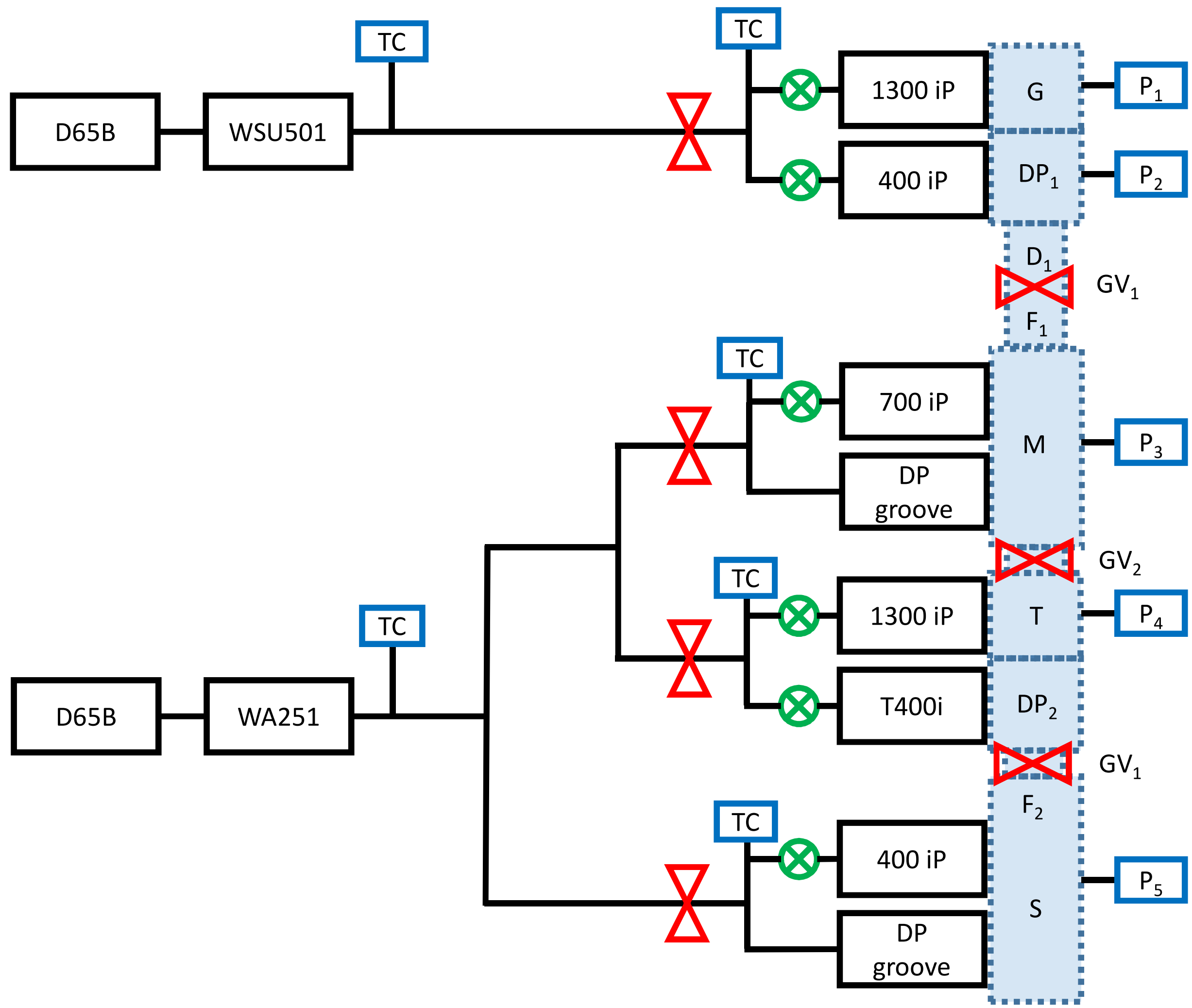


Figure 2.15: Block diagram of the TABLE's rough vacuum system showing rough and turbo pumps, control valves and pressure gauges. TC: thermocouple pressure gauge; P: UHV pressure gauge; ⊗: manual valve, ⋈: rough vacuum solenoid or UHV pneumatic gate valve. UHV is indicated by blue shaded region. G: generation chamber, DP: differential pumping chamber, M: mirror chamber, T: target chamber, S: photon spectrometer chamber.

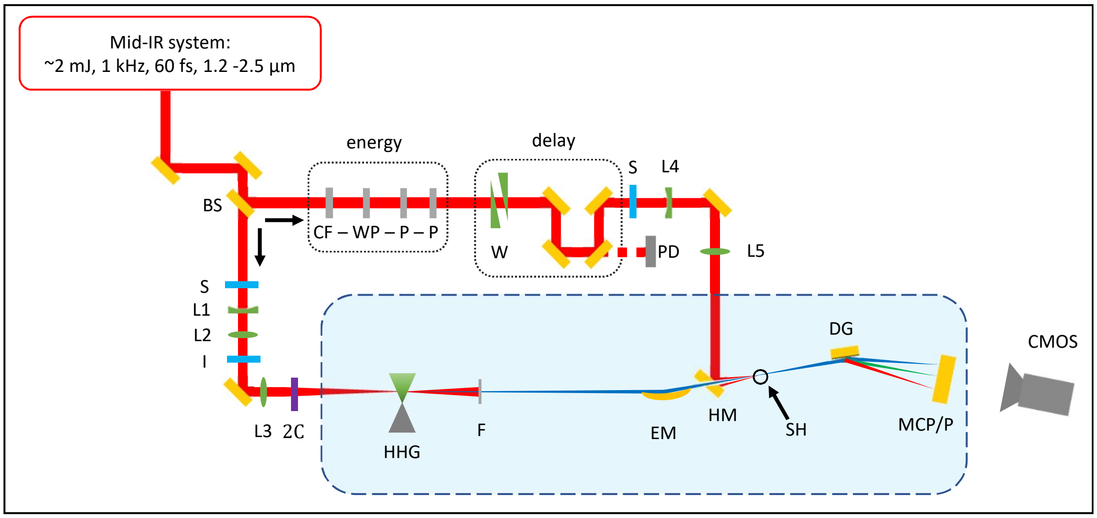


Figure 2.16: Schematic of the Transient Absorption BeamLine (TABLe). Blue shaded region represents vacuum. BS: beam splitter, S: computer-controlled shutter, L: lens, I: iris, 2C: optics for two-color generation, HHG: high harmonic generation, F: metallic filter, EM: ellipsoidal mirror, HM: hole mirror, SH: sample holder, CF: long-pass color filter, WP: $\lambda/2$ waveplate, P: wire-grid polarizer, W: delay wedges, PD: photodiode and associated optics, DG: dispersive grating, MCP/P: micro-channel plate and phosphor.

there is no pressure differential across the UHV gate valves before they are opened. If the pressure on either side of the gate valve is above a setpoint, the OMRON will prevent it from opening. Finally, when the OMRON is armed, it will monitor for the pressure in each chamber and perform an emergency shutdown/vent procedure if any pressure gauge reports pressures above a setpoint.

## 2.4 XUV Optics

In this section, we will discuss the XUV optical design of the TABLe system. We start with a statement of the design goals, followed by a general discussion of XUV focusing optics to motivate our choice of the Zeiss gold coated ellipsoidal mirror.

### 2.4.1 Design Goals

We started with several design requirements. First, we wanted to be able to deliver XUV light onto the sample with photon energies as high as 300 eV, which would enable us to study carbon containing materials such as graphene. However, we also wanted to preserve the lower energy portion of the harmonic spectrum, allowing the study of semiconductor and transition metal compounds. This broadband requirement restricts us to metal-coated reflective optics.

Condensed matter ATAS experiments have significantly higher XUV flux requirements compared to RABBITT experiments. This meant that our XUV focusing solution needed to have the highest reflectivity possible, and we needed to minimize any XUV losses elsewhere in the beamline. This restricts us to single optic solutions, and puts stringent requirements on the smoothness of the optic.

The IR intensity profile at the focus is an important parameter for every experiment. In a transient absorption experiment, the experimental signal originates from the spatial overlap of the sample, the XUV and the IR light in the interaction region. Ideally, neither pulse would have any spatial structure at the interaction plane. In the real world, we design the optics to minimize the intensity variation of the IR over the spatial extent of the XUV spot. For finite beam sizes, this is accomplished by focusing the XUV tighter than the IR while minimizing aberrations.

Although the primary scientific goal for this work was transient absorption experiments in condensed matter, the requirements of other experiments were considered during the design phase of the apparatus. Aside from general modularity, we wanted the beamline to be able to study strong field physics in helium, which has an IR intensity requirement in the target chamber on the order of $10^{14}$ W/cm$^2$. These intensities are neither required nor desired for condensed matter ATAS experiments, as sample damage can easily occur in condensed phase materials around $10^{12}$ W/cm$^2$. We chose to demagnify the XUV spot size by a factor of three, which reduces the XUV spot area by a factor of nine. This allows us to more strongly focus the IR pump pulse, resulting in a nine-fold increase of interaction intensity without changing the relative spot sizes of the XUV and the IR. This allowed us to reach our goal of $10^{14}$ W/cm$^2$ for the doubly ionized helium gas for $e - 2e$ experiments [46].

As we will discuss below, we are restricted to a reflective focusing geometry. As such, one relevant parameter is the ratio of the entrance and exit arms of the XUV optic. A desire to have modular endstations put a lower limit on the XUV optic's exit arm; too short and the mirror chamber would have to merge with the target chamber. Likewise, the footprint of the beamline had to fit within the south east target room, which put constraints on the length of the entrance arm.

**Reflective Optics**

The XUV light is divergent after its generation and needs to be focused onto a sample for the experiment. The short relatively wavelength of the XUV puts strong requirements on the surface quality of the focusing optic, raising the cost and manufacturing time significantly. Alignment of the optic is frustrated by the need for in-vacuum propagation and the invisible nature of XUV light. These factors lead us to pursue a "one size fits all" broadband optic rather than a series of interchangeable narrow bandwidth optics tailored for individual experiments.

The presence of strong absorption edges over the bandwidth of the XUV pulse precludes the use of transmissive optics for most applications. Narrow bandwidth transmissive optics have been designed to exploit the dispersion near an absorption edge [23]. However, these techniques cannot be extended to support the entire bandwidth of our XUV pulses. Reflective dielectric coatings have been designed for the XUV but they have a bandwidth of only $10 - 20$ eV [46]. These considerations leave reflective optics as the only good choice for broadband XUV light.

XUV and x-ray reflective optics consist of highly polished curved substrates with a thin (typically 40 nm) metal coating applied to the polished surface. As a reflective optic, the precise shape of the surface (discussed below) determines the focusing properties, and the coating influences the spectral reflectivity and overall performance. The high tolerances and custom nature of these optics makes them very expensive (tens of thousands of dollars) with a long manufacturing lead time (12 months), so it was important to make an informed decision about this purchase. In the following sections we will briefly introduce the physics relevant to XUV optics, namely Fresnel reflection from a rough surface. We will use these results to motivate the selection of our XUV optic.

### 2.4.2 Fresnel Reflection from a Rough Surface

We use the familiar Fresnel equations to model reflection from the surface of a conductive surface [92]. In the equations that follow, the vacuum is denoted by $j = 1$ and the conductive material is $j = 2$. The incident electric field is $E_I$ and the reflected component is $E_R$. We use the standard convention to denote the polarization[1]: $p$-polarized light has an incident electric field parallel to the plane of incidence; $s$-polarized has an incident electric field perpendicular to the plane [3]. The complex reflection amplitudes $\hat{r}_{s,p}$ are written in terms of the complex impedance $\hat{Z}_j = \mu_j c/\hat{n}_j$ and the angle measured from the normal in each medium $\theta_j$:

$$\hat{r}_s \equiv \left[\frac{E_R}{E_I}\right]_s = \frac{\hat{Z}_2 \cos\theta_1 - \hat{Z}_1 \cos\theta_2}{\hat{Z}_2 \cos\theta_1 + \hat{Z}_1 \cos\theta_2} \tag{2.7}$$

$$\hat{r}_p \equiv \left[\frac{E_R}{E_I}\right]_p = \frac{\hat{Z}_1 \cos\theta_1 - \hat{Z}_2 \cos\theta_2}{\hat{Z}_1 \cos\theta_1 + \hat{Z}_2 \cos\theta_2} \tag{2.8}$$

Next, we assume non-magnetic media ($\mu_1 = \mu_2 = \mu_0$) and that the initial medium is vacuum ($\hat{n}_1 = 1$). We can express the reflection amplitudes using the complex index of refraction $\hat{n}_2 = n_2 + ik_2$:

$$\hat{r}_s = \frac{\cos\theta_1 - \hat{n}_2 \cos\theta_2}{\cos\theta_1 - \hat{n}_2 \cos\theta_2} \tag{2.9}$$

[1]The designations $s$ and $p$ follow from the German words for perpendicular (*senkrecht*) and parallel (*parallele*).

$$\hat{r}_p = \frac{\cos\theta_2 - \hat{n}_2\cos\theta_1}{\cos\theta_2 + \hat{n}_2\cos\theta_1} \tag{2.10}$$

The reflectance $R$ is the modulus squared of the reflection amplitudes:

$$R_s = \left|\frac{\cos\theta_i - \hat{n}_2\cos\theta_t}{\cos\theta_i - \hat{n}_2\cos\theta_t}\right|^2 \tag{2.11}$$

$$R_p = \left|\frac{\cos\theta_t - \hat{n}_2\cos\theta_i}{\cos\theta_t + \hat{n}_2\cos\theta_i}\right|^2 \tag{2.12}$$

We introduce the *glancing angle* $\phi \equiv \pi/2 - \theta$, which is the compliment to $\theta$. Total external reflection, where the incident rays do not penetrate the medium but rather propagate along the interface at angle $\phi_2 = 0$, occurs at incident glancing angles below the *critical incident angle* $\phi_c$:

$$\cos\phi_c = 1 - \delta \tag{2.13}$$

where $\delta$ is defined via $\tilde{n} = (1-\delta) - i\beta$. The x-ray optics literature often makes approximations to the above reflectance equations using either the small angle approximation ($\delta \ll 1$ and $\cos\phi_c \sim 1$, or $\phi_1 \ll 1$), or the assumption that we are operating near the critical angle ($\phi_1 \sim \phi_c$) [3]. Note these assumptions are not neccessarily true for our geometry, especially at photon energies below 200 eV, where the critical angle for gold exceeds 10 degrees.

The above is valid for a perfectly smooth interface, but real optics have finite roughness. The effect of surface roughness on the reflection amplitude $\hat{r}$ is commonly treated by either the *Debye-Waller* or *Névot-Croce* factors. The relative sizes of the extinction length $(1/k_2)$ and the in-plane characteristic length scale $(\delta r)$ of the surface roughness determine which formalism is appropriate [30, 79]. For XUV light at a grazing angle on a gold surface, the extinction length is on the order of 10 nm, which is much smaller than the length scale of the surface roughness of highly polished materials (micron or mm scale). In this case, $\delta r$ is large enough for the incident and reflected fields have a precise phase relationship and the Debye-Waller formalism is appropriate [82]. Thus, the reflectance of our mirror can be modelled as:

$$\hat{r}^{rough} = \hat{r}^{smooth}\exp\left(-2k_{1,z}^2\langle z^2\rangle\right) \tag{2.14}$$

where $\langle z^2\rangle$ is the variance of the interface height and $k_{1,z} = 2\pi\cos\theta_i/\lambda$ is the normal component of the wave vector in medium 1 (in our case, vacuum). To get a sense of scale, a high quality off-the-shelf optic will have a surface roughness of $\langle z^2\rangle = \lambda/10 = 63.2$ nm, which is 5 times larger than the wavelength of a 100 eV photon. It is clear that we need to take advantage of specialized manufacturing techqniques while working in the XUV. Below, we apply this basic framework to guide the selection of the basic materials and geometric properties of our XUV focusing optic.

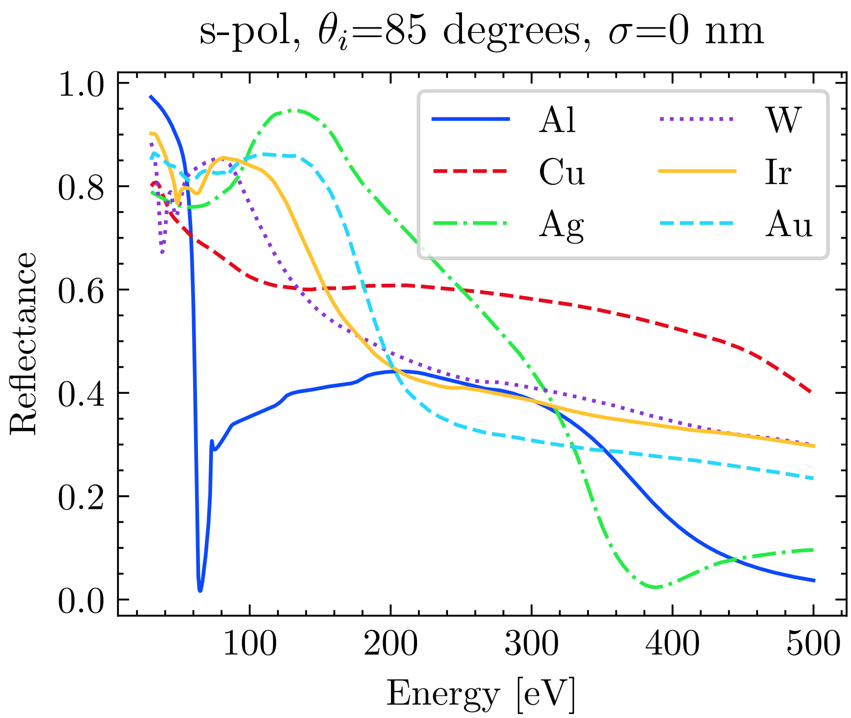


Figure 2.17: Fresnel reflectance for s-polarized light on smooth metal mirrors at a grazing angle of 5 degrees. Refractive index data obtained from [32, 36]. Calculation follows Eqs. (2.11) and (2.14).

**The Metallic Coating**

Fig. 2.17 shows the Fresnel reflectance for various materials at a fixed 5 degree grazing angle (85 degree incident angle). From this figure, we can see that the materials properties strongly influence mirror perforance at these energies. Aluminum (Al) has a sharp absorption feature at 72 eV which is undesirable for a reflective optic; tungsten (W) and iridium (Ir) have extended spectral features between 35 and 50 eV. Silver (Ag) has the best reflectance below 250 eV. Copper (Cu) has the flattest performance out to 400 eV, with very few spectral features. Gold (Au) has good performance below 200 eV and a relatively flat spectral response outside the 150 - 200 eV region.

Gold, silver and copper are good candidates for our desired spectral range. However, silver and copper can tarnish when exposed to atmosphere, which would change their reflectivity over time. Although the optic will be stored under vacuum, it will inevitably be exposed to air during transport, installation and whenever the beamline is vented. Due to the extremely thin and fragile optical coating, it is not possible to clean the XUV optic if it becomes dirty, damaged or tarnished. Gold was chosen to maximize the lifetime of the optic.

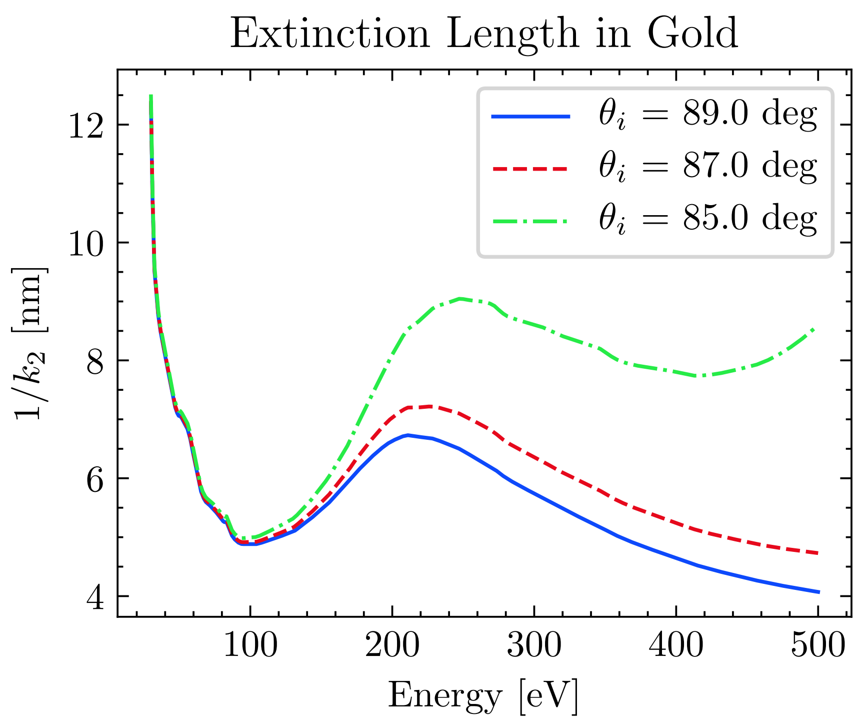


Figure 2.18: Extinction length in gold at various incident angles. Refractive index data obtained from [32, 36].

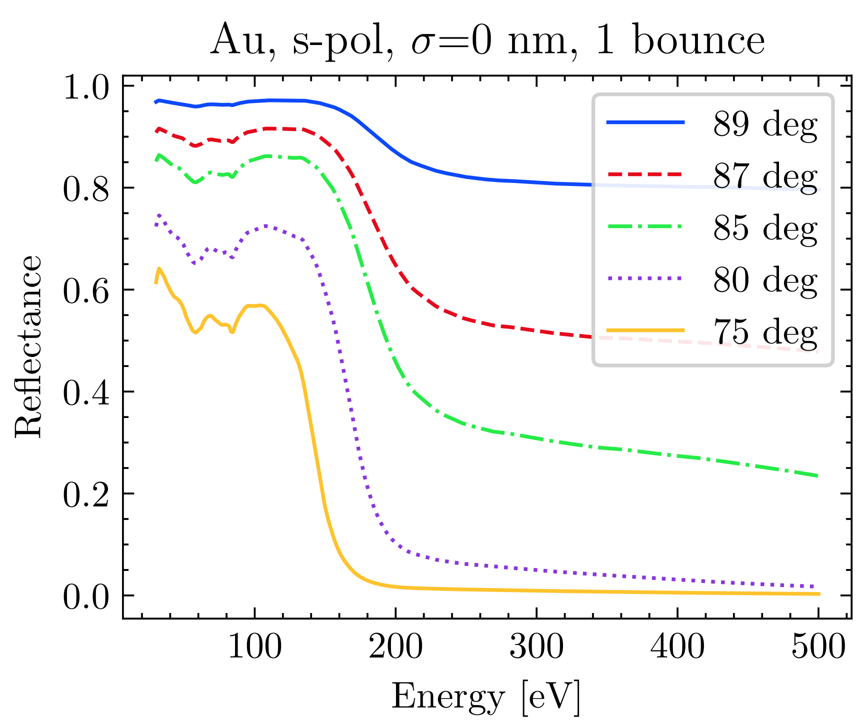


Figure 2.19: Fresnel reflectance for $s$-polarized light from a single smooth gold mirror as a function of incident angle. Calculation follows Eqs. (2.11) and (2.14).

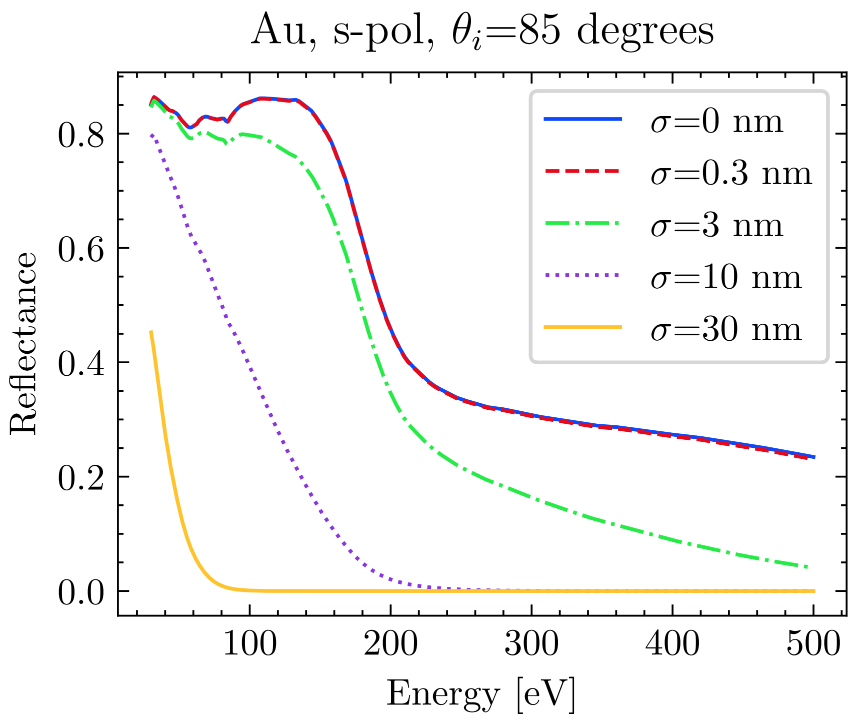


Figure 2.20: Effect of surface roughness on reflectance. Calculation follows Eqs. (2.11) and (2.14).

The Fresnel analysis used above is valid for an infinitely thick medium, but one must question whether this is valid for a thin film gold coating. To answer this question, we plot the extinction length ($1/k_2$) in Fig. 2.18, with $k_2$ defined as $k_2 = (2\pi/\lambda)\sqrt{\sin\theta_i^2 - \mathrm{Re}\,\hat{n}_2}$ [92]. We can see that above 30 eV, the extinction length remains below 13 nm; above 40 eV the extinction length is bounded by 10 nm. Based on this information, we decided to use the standard 40 nm coating offered by Zeiss. An adhesion layer (Cr) was applied to the substrate to prevent flaking of the gold coating. It should be noted that over time, the adhesion layer will diffuse into the gold and change the reflectivity.

Fig. 2.19 shows the reflectivity of a single gold mirror for various incident angles. As expected, the best performance occurs at small grazing angles. However, for a fixed beam size, the required optic size increases as the grazing angle decreases. The footprint (area) $F$ of a rectangular beam on the optic is given by the geometric projection [30]:

$$F = \frac{t_1}{\cos\theta_i} t_2 \tag{2.15}$$

Here, $t_1$ and $t_2$ are the rectangular dimensions of the input beam and $\theta_i$ is the incident angle of the light. If we do not scale the mirror size with the incident angle, we will clip the beam and lose XUV flux. Our desire to have a modular vacuum apparatus with a demagnifying

XUV optic is in direct conflict with our desire to have high XUV flux. The exit arm of the mirror, which is proportional to the demagnification factor, must be large enough so that the interaction region can be contained within a separate chamber from the rest of the beamline. We clearly cannot achieve the specifications of a typical x-ray mirror in a synchrotron facility ($\approx 0.5$ degree grazing angle, $\approx 1$ m lateral dimension). Returning to Fig. 2.19, we can see that an 87 degree mirror drastically outperforms an 85 degree mirror above 200 eV, but according to Eq. (2.15), it will be 67% larger in the horizontal dimension. Larger mirrors have more mass, which increases the requirements for the *in vacuo* motorization, further increasing the cost and required chamber size. Finally, the manufacturing cost and lead time of the mirror is proportional to the polished area. Through an interative design process involving the optical, motorization and vacuum chamber design elements, as well as Zeiss' manufacturing considerations, we decided to use an 85 degree mirror in the TABLe. This allowed us to place the interaction region in a separate chamber, minimized the cost of the mirror, and delivered better than 50% reflectivity below 200 eV while utilizing small form factor motors and stages.

The effect of the surface roughness is shown in Fig. 2.20. When polishing glass surfaces, a surface roughness of 0.3 nm is considered state of the art and approaches a height variation of a single atomic layer. Below 500 eV, the difference between a surface with 0.3 nm roughness and an ideal interface is negligible.

### 2.4.3 Aberration-Free Focusing

XUV mirrors are typically simple rotational solids (cylinder, toroid, ellipsoid, etc.), and we considered several configurations during the planning stage. It is well known that reflective optics operating at grazing angles can cause abberations at the focus. These abberations introduce phase nonuniformity, smearing the XUV pulse out in time and reducing the effective temporal resolution of the apparatus [7]. Additionally, abberations change the shape of the XUV focal spot, which results in a larger range of IR intensities throughout the XUV-IR interaction volume for a fixed IR focusing geometry. Therefore it is critical to minimize or eliminate abberations through optical design.

#### The Light Path Function

Abberations are mathematically analyzed using the *light path function* [38, 62, 70]. Consider a reflective optic with an optical surface in the $yz$ plane as shown in Fig. 2.21. The height of the optic surface $x$ can be described by the following power series:

$$x = \sum_{i=0}^{\infty} \sum_{j=0}^{\infty} a_{ij} y^i z^j, \quad a_{00} = a_{10} = 0, \quad j = \text{ even} \tag{2.16}$$

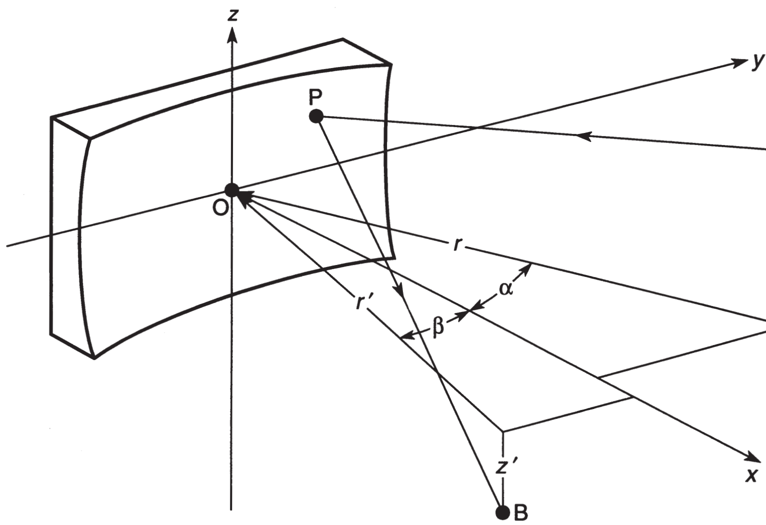


Figure 2.21: Coordinate system used for the light path function $F$. Source point $A$ is located a distance $r$ from the center of the mirror at angle $\alpha$ and height $z$. Focus point $B$ is located a distance $r'$ away, with angle $\beta$ and height $z'$. Impact point $P$ is located on the mirror surface at point $(y, z) = (w, l)$ and height $x$. Figure adapted from [38].

| i \ j | **0** | **1** | **2** | **3** | **4** |
|---|---|---|---|---|---|
| **0** | $0$ | $0$ | $S$ | $0$ | $\frac{4a_{02}^2 - S^2}{r} - 8a_{04}\cos\alpha$ |
| **1** | $-\sin\alpha$ | $0$ | $\frac{S\sin\alpha}{r} - 2a_{12}\cos\alpha$ | $0$ | $*$ |
| **2** | $T$ | $0$ | $\frac{4a_{20}a_{02} - TS - 2a_{12}\sin 2\alpha}{r} + \frac{2S\sin^2\alpha}{r^2} - 4a_{22}\cos\alpha$ | $0$ | $*$ |
| **3** | $\frac{T\sin\alpha}{r} - 2a_{30}\cos\alpha$ | $0$ | $*$ | $0$ | $*$ |
| **4** | $\frac{4a_{20}^2 - T^2 - 4a_{30}\sin 2\alpha}{r} + \frac{4T\sin^2\alpha}{r^2} - 8a_{40}\cos\alpha$ | $0$ | $*$ | $0$ | $*$ |

Table 2.1: Values of $E_{ij0}(\alpha, r, 0)$ up to $4^{\text{th}}$ order, used in the calculation of the light path function $F$. Terms in excess of $4^{\text{th}}$ order are indicated by *. See text for definitions of $S$ and $T$. Table adapted from [38].

This expansion can be used to describe spherical, cylindrical, toroidal, ellipsoidal, or other aspheric surfaces given proper values of the coefficients $a_{ij}$.[2] Now consider the situation shown in Fig. 2.21, where a ray is emitted from a point source $A$ and focused at point $B$ after reflecting off the surface of the optic at point $P$. The distance this ray travels is called the light path function, $F = \overline{AP} + \overline{PB}$. We are primarily concerned with abberations at the focus which are proportional to the derivative of $F$ with respect to impact coordinates $w$ and $l$. So, we drop the zeroth-order constant $r + r'$ and perform a power series expansion with respect to the impact point $P(w, l)$:

$$\begin{aligned} F = wF_{100} + wF_{102} + lF_{011} + \frac{1}{2}w^2F_{200} + \frac{1}{2}l^2F_{020} \\ + \frac{1}{2}w^3F_{300} + \frac{1}{2}wl^2F_{120} + wlF_{111} + \frac{1}{8}w^4F_{400} + \frac{1}{4}w^2l^2F_{220} \\ + \frac{1}{4}w^2F_{202} + \frac{1}{2}l^2F_{022} + \frac{1}{2}l^3F_{031} + \frac{1}{2}w^2lF_{211} + \cdots \end{aligned} \tag{2.17}$$

This expression is valid for both mirrors and gratings, but it can be greatly simplified for our application. For a non-holographic grating, the coefficients of $F$ must take the form $F_{ijk} = E_{ijk}(\alpha, r, z) + E_{ijk}(\beta, r', z')$. Next, if points $A$ and $B$ are within the symmetry plane of the mirror ($z = z' = 0$), then subscript $k$ must be equal to zero. Finally, from the law of reflection, we have $\alpha = -\beta$. Putting it all together, the coefficients of the series expansion of $F$ have the form:

$$F_{ij0} = E_{ij0}(\alpha, r, 0) + E_{ij0}(-\alpha, r', 0) \tag{2.18}$$

The values of $E_{ij0}(\alpha, r, 0)$ can be found in the literature and in Table 2.1. The terms $S$ and $T$ used in this table are defined below:

$$T = \frac{\cos^2\alpha}{r} - 2a_{20}\cos\alpha \tag{2.19}$$

$$S = \frac{1}{r} - 2a_{02}\cos\alpha \tag{2.20}$$

Note that information about the shape of the mirror is connected to the $F_{ij0}$ expansion coefficients via the $a_{ij}$ mirror surface expansion coefficients. Therefore, we can apply this framework to calculate the abberations at the focus for a given mirror shape and geometry.

A consequence of Fermat's Principal of Least Time is that $F$ will be an extrema for any point $P$ on the mirror's surface. Therefore, abberation-free image focusing can be obtained if $\delta F/\delta w = \delta F/\delta l = 0$. This condition must hold for any value of $w$ and $l$ on the mirror's surface, from which it follows that all $F_{ij0}$ terms are identically zero. We can quantify aberrations at the focus using a geometric ray approximation, in which we calculate the

[2]Tables 2 and 3 in reference [38] provide $a_{ij}$ values for an ellipsoidal and toroidal mirror, respectively.

displacements of the rays from the image point $B$:

$$\begin{aligned}\Delta y'_{ij0} &= \frac{r'}{\cos\alpha}\left(\frac{\delta F}{\delta w}\right)_{ij0} \\ \Delta z'_{ij0} &= r'\left(\frac{\delta F}{\delta l}\right)_{ij0}\end{aligned} \tag{2.21}$$

The total ray abberation in the $\Delta y'$ ($\Delta z'$) direction is the algebraic sum of the above terms for all values of $i$ and $j$. Therefore, the total ray abberation (to 4$^{\text{th}}$ order) is:

$$\begin{aligned}\Delta z' &= r'\left(F_{020}l + F_{120}wl + \frac{1}{2}F_{220}w^2 l + \frac{1}{2}F_{040}l^3\right) \\ \Delta y' &= \frac{r'}{\cos\alpha}\left(F_{100} + F_{200}w + \frac{1}{2}F_{120}l^2 + \frac{3}{2}F_{300}w^2 + \frac{1}{2}F_{400}w^3 + \frac{1}{2}F_{220}w^2 l^2\right)\end{aligned} \tag{2.22}$$

We now have expressions for the abberations as a function of the shape of the XUV mirror, which will be applied to different mirror configurations.

### Toroidal Mirrors

A toroidal mirror is a section of the interior surface formed by a torus (similar to a bicycle tire) described by radii $R$ and $\rho$. There are many advantages to using a toroid in an XUV beamline. Toroidal mirrors operated in a $2f-2f$ configuration can re-image the source point without introducing any aberrations at the focus [16]. Additionally, the toroid's constant curvature allows it to be manufactured to a higher degree of accuracy than other shapes [38]. As a result they are very affordable, starting as low as $5,000.

The toroidal mirror can be designed to reduce abberations. Owing to its symmetry, a toroid naturally has $F_{100} = F_{120} = 0$. An analysis of the $F_{ij0}$ expansion coefficients reveals $F_{200}$ and $F_{020}$ will also equal zero if the toroid's radii are set to the following values:

$$\begin{aligned}\rho &= \frac{2rr'\cos\alpha}{r+r'} \\ R &= \frac{2rr'\sec\alpha}{r+r'}\end{aligned} \tag{2.23}$$

With these radii, the remaining non-zero terms of Eq. (2.17) are $F_{040}, F_{220}, F_{300}$ and $F_{400}$. Introducing the demagnification factor $M = r/r'$, the non-zero terms have the following

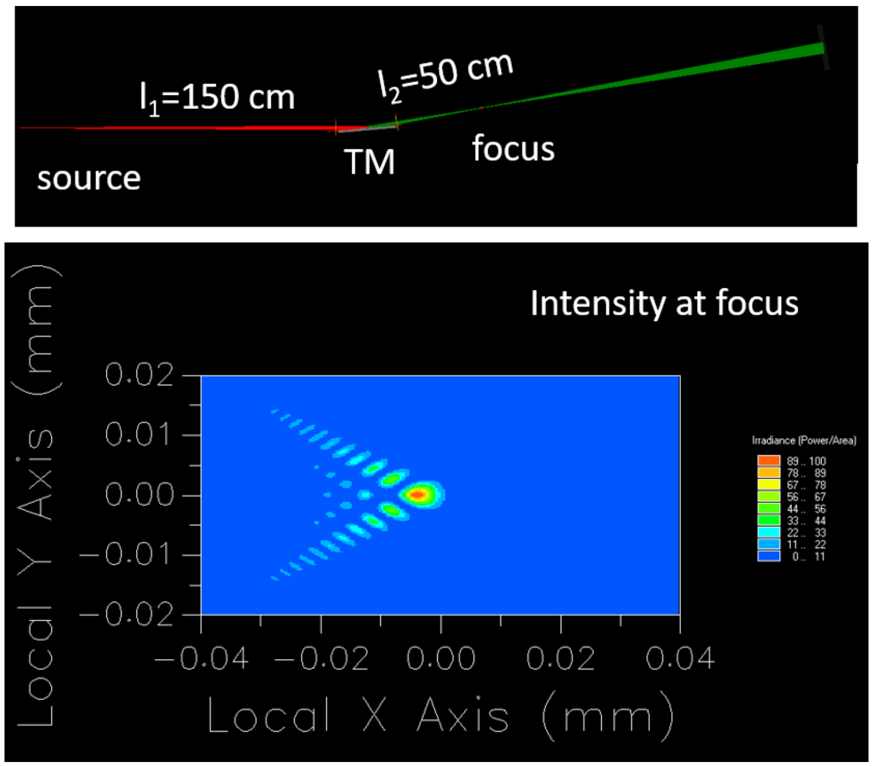


Figure 2.22: Complex raytracing simulation showing severe abberations at the focus of a demagnifying toroidal mirror (TM). The entrance arm $l_1$ is 150 cm, the exit arm $l_2$ is 50 cm, and the grazing angle is 5 degrees. Top panel: overhead view of the simulation showing the source rays (red) and the focused rays (green). Bottom panel: intensity at the focal plane in arbitrary units. Calculations were performed using Photon Engineering's FRED software [68].

values:

$$\begin{aligned}
F_{300} &= -\left(\frac{M^2-1}{M}\right)\frac{\cos^2\alpha\sin\alpha}{2(r')^2} \\
F_{040} &= -\frac{(M^2-1)(M+1)}{M^3(r')^3} \\
F_{220} &= \frac{2(M^3+1)-(3M^3-M^2-M+3)\cos 2\alpha}{4M^3(r')^3} \\
F_{400} &= -\frac{(1+M)\cos^2\alpha\left[-4+6M-4M^2+(5+M(-8+5M))\cos 2\alpha\right]}{4M^3(r')^3}
\end{aligned} \tag{2.24}$$

Recalling Eq. (2.22), we see that $F_{300}$ corresponds to a second-order aberration, and $F_{040}, F_{220}$ and $F_{400}$ correspond to third-order and fourth-order aberrations. For the special case of $M = 1$, Eq. (2.24) simplifies to:

$$\begin{aligned}
F_{300} &= 0 \\
F_{040} &= 0 \\
F_{220} &= \frac{2\sin^2\alpha}{(r')^3} \\
F_{400} &= \frac{2\cos^2\alpha\sin^2\alpha}{(r')^3}
\end{aligned} \tag{2.25}$$

So, the toroid only has third-order aberrations if $M = 1$, but second-order aberrations exist if $M \neq 1$.

Simulations of a demagnifying ($M = 3$) toroidal mirror were performed using numerical complex ray tracing techniques, implemented via Photon Engineering's FRED software [2, 68]. The results of this simulation are shown in Fig. 2.22. We can see strong abberations are present at the focus that would be detrimental to the performance of the TABLe apparatus. For this reason, we decided against using a toroid in our beamline.

### Spherical Mirrors

It is well known that spherical mirrors introduce significant aberration when operated away from normal incidence [38]. This is because a spherical mirror is simply a toroidal mirror with equal radii of curvature ($R = \rho$). For this reason, we did not pursue a spherical mirror solution.

### Dual Mirror Configurations

Introducing a second XUV optic can counteract the abberations introduced by the first [38]. The most common configuration is the Kirtpatrick-Baez (KB) mirror pair, which is commonly used in synchrotrons [47]. A KB mirror pair consists of two cylindrical mirrors

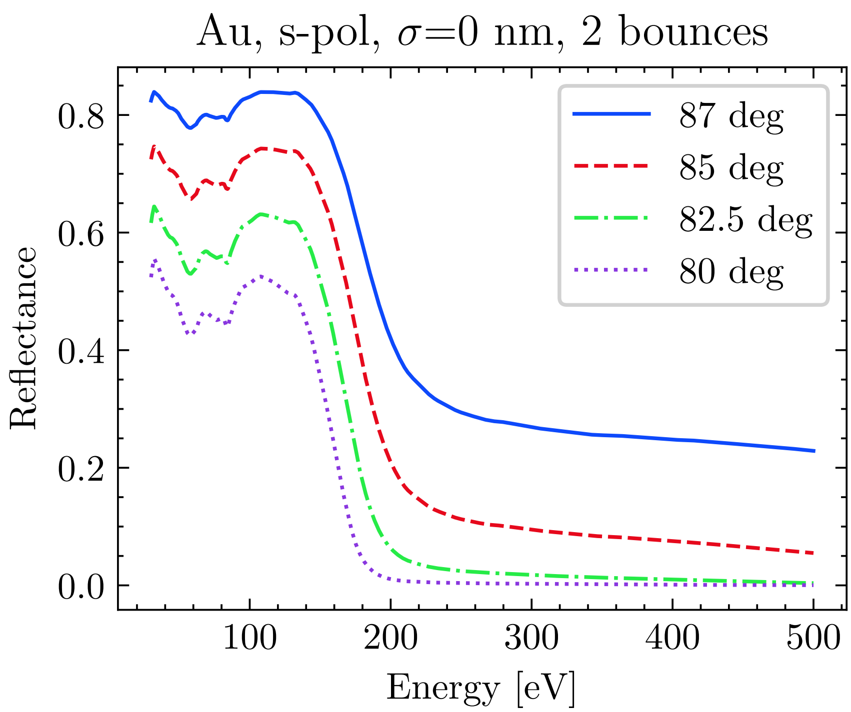


Figure 2.23: Fresnel reflectance for $s$-polarized light from two smooth gold mirrors as a function of incident angle. Calculation follows Eqs. (2.11) and (2.14).

with the normal direction of their optical surfaces placed orthogonally to each other and the beam propagation direction. In this geometry, each mirror focuses along one direction, and together they act as a single optic that focuses in both transverse directions. Another option is a dual toroid configuration, which has a real focus located between the two mirrors [70]. Both of these ideas were considered but ultimately deemed impractical.

Fig. 2.23 illustrates the problem with a dual optic design design. Two 85 degree optics have a reflectance of only 20% at 200 eV, and have at least twice the footprint as a single 85 degree optic. To achieve the performance of a single 85 degree optic at 200 eV, the mirror pair needs to be operated at 87 degrees. As discussed above, this 87 degree pair will be 3.33 times larger than a single 85 degree optic in the beam propagation direction. On the other hand, if we want our two mirror configuration to maintain the footprint of a single 85 degree optic, it needs to be operated at 80 degrees. This geometry yields a reflectivity of only 1% at 200 eV, which is insufficient for our experimental requirements. Clearly, a single-optic solution is preferrable.

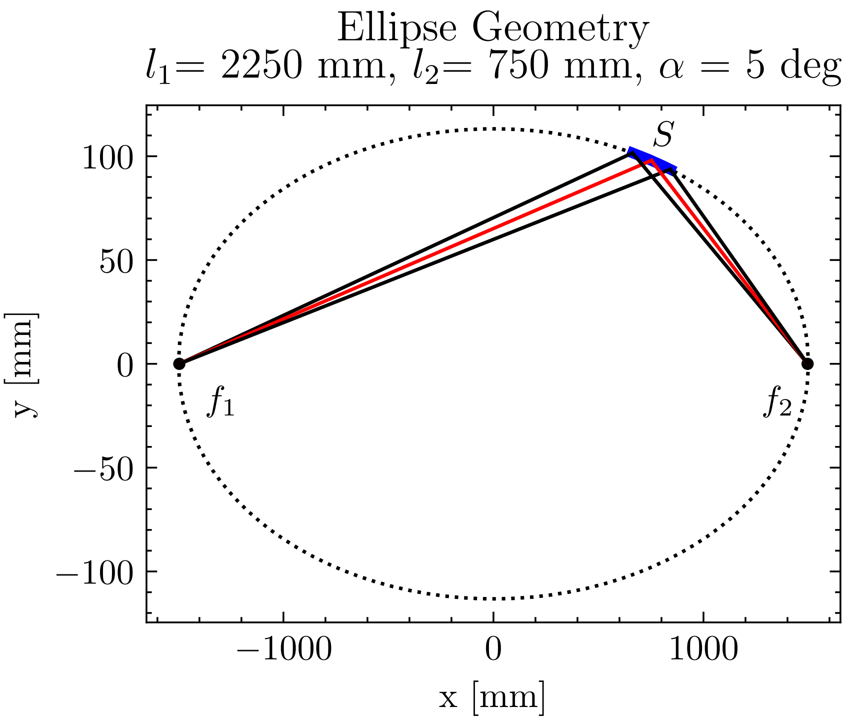


Figure 2.24: Overhead view of the ellipsoidal mirror geometry used in our beamline. Mirror surface $S$ is shown in blue; foci $f_{1,2}$ are represented by black dots. Rays that strike the center (red) and the edges (black) of the mirror are depicted as lines. Vertical scale is enlarged to show detail. Drawing is otherwise to scale to match the dimensions in Table 2.2.

### Ellipsoidal Mirrors

We can apply the same light path function analysis to the ellipsoidal mirror. If we do the analysis, we will see that most of the terms in Eq. (2.17) are identically zero. The only non-zero term is $F_{220}$, which evaluates to:

$$F_{220} = \frac{(1+M)\left[-3 - M(2+3M) + 3(M-1)^2 \cos 2\alpha\right](\cot\alpha + \tan\alpha - 2)}{16M^3(r')^3} \tag{2.26}$$

As a result, the light path function for an ellipsoid is simply $F = \frac{1}{4}w^2 l^2 F_{220}$. Therefore, the largest abberations from an ellipsoid are third-order in the abberation expansion, which is a significant improvement upon the performance of a toroidal mirror.

We have shown that an ellipsoidal mirror is able to demagnify a point source without introducing significant abberations at the focus. As a single optic solution, it avoids the reflectivity losses of a dual mirror configuration. However, its variable radius of curvature provides manufacturing challenges that have only been overcome in the past several years [60]. This requires the use of special manufacturing techniques thats significantly raise the cost and lead time of the optic. At the time of purchase, Carl Zeiss Laser Optics GmbH was the only company that could manufacture and verify the shape of an ellipsoidal mirror that met our technical requirements.

The shape of the rotational ellipsoid can be completely described by three parameters: the two semiaxes ($a$, $b$) and the horizontal[3] off-axis position $y_M$. An alternative set of parameters are the entrance and exit arm lengths ($l_1$, $l_2$) and the grazing angle $\alpha$. Additionally, the spatial extent (clear aperture) of the optic is specified by the tangential length $L$ and the out-of-plane width $W$. Below, we will show how these quantities are related.

In a Cartesian coordinate system, an ellipsoid of revolution is described by parameters $a$ and $b$:

$$\frac{x^2}{a^2} + \frac{y^2 + z^2}{b^2} = 1 \tag{2.27}$$

where the $xy$ plane is the (horizontal) optical plane and $z$ is the direction orthogonal to the optical plane (vertical).[4] Due to the symmetry between $y$ and $z$, much of the analysis can be done in the optical plane ($z = 0$):

$$\frac{x^2}{a^2} + \frac{y^2}{b^2} = 1 \tag{2.28}$$

In the $xy$ plane, the surface of the mirror is a segment of the curve formed by Eq. (2.28), which is shown in Fig. 2.24. The center of the mirror (off-axis position) is denoted by

[3] Our mirror has vertical symmetry, so $y_M = 0$.

[4] Note that this coordinate system differs from the one used to describe the mirror surface in the previous section.

| | | | |
|---|---|---|---|
| **substrate** | | | |
| surface geometry | concave rot. ellipsoid | | |
| material | fused Silica HOQ310 | | |
| dimensions ($L \times W \times H$) | $240 \times 76 \times 45 \pm 0.2$ mm | | |
| **optical surface** | | | |
| clear aperture ($L \times W$) | $180 \times 16$ mm | | |
| footprint geometry | rectangular | | |
| **geometry parameters** | | **alternative set** | |
| semiaxis $a$ | 1500 mm | entrance arm $l_1$ | 2250 mm |
| semiaxis $b$ | 113.219 mm | exit arm $l_2$ | 750 mm |
| off-axis position $x_M$ | 752.146 mm | grazing angle | 5 deg |
| **surface quality** | | **spatial sampling rate** | |
| tangential slope error | $\leq 2.0$ arcsec (rms) | $2 - 180$ mm | |
| sagittal slope error | $\leq 10.0$ arcsec (rms) | $2 - 16$ mm | |
| mid spatial frequency roughness | $\leq 0.3$ nm (rms) | $1.0 - 200$ $\mu$m | |
| **coating material** | | | |
| $40 \pm 5$ nm Au w/ Cr binding layer | | | |

Table 2.2: Specifications of the ellipsoidal mirror. Data provided by Carl Zeiss Laser Optics GmbH.

$(x, y) = (x_M, y_M)$. The ellipse has eccentricity $\epsilon$,

$$\epsilon = \sqrt{1 - \frac{b^2}{a^2}}, \tag{2.29}$$

and focal points at positions $(x, y) = (\pm a\epsilon, 0)$. Consider a light source at the first focal point, $f_1 = (-a\epsilon, 0)$: rays emanating from $f_1$ will strike surface of the ellipse at some point $S = (x_0, y_0)$ and focus to $f_2 = (a\epsilon, 0)$. This optical system has an entrance arm $l_1 = f_1S$, exit arm $l_2 = Sf_1$, and demagnification $M$ given by:

$$l_1 = \sqrt{(x_0 + a\epsilon)^2 + y_0^2} \tag{2.30}$$

$$l_2 = \sqrt{(x_0 - a\epsilon)^2 + y_0^2} \tag{2.31}$$

$$M = \frac{l_1}{l_2} \tag{2.32}$$

Once the $f_1$, $f_2$ and $S$ are defined, the grazing angle $\alpha$ of reflection can be found by applying the Law of Cosines:

$$\alpha = \frac{1}{2} \arccos\left(\frac{(2a\epsilon)^2 - l_1^2 - l_2^2}{2l_1l_2}\right) \tag{2.33}$$

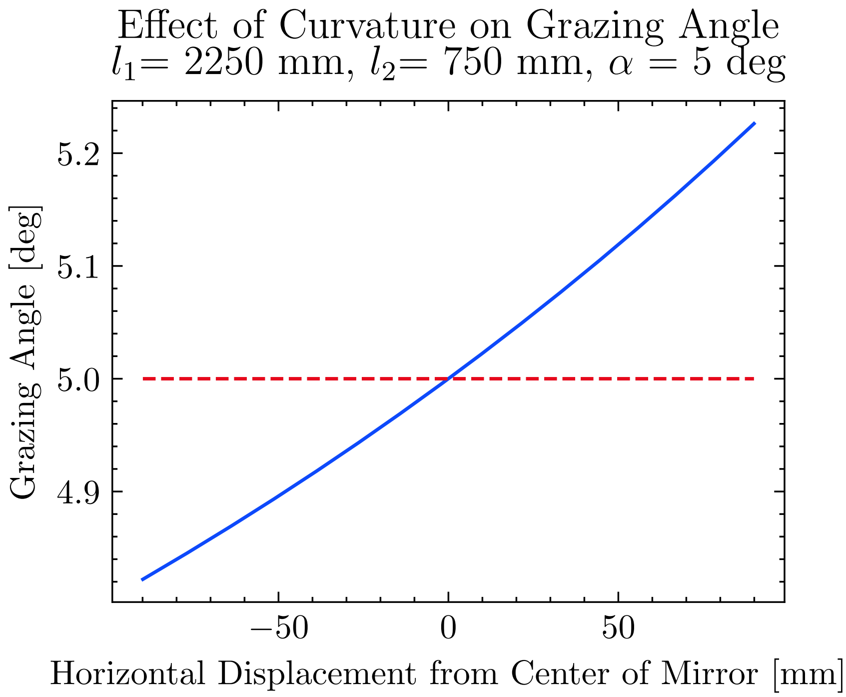


Figure 2.25: The effect of curvature on the local grazing angle along the mirror's symmetry axis ($z = 0$). Light that strikes the edges of the mirror will experience a slightly different grazing angle than the design angle.

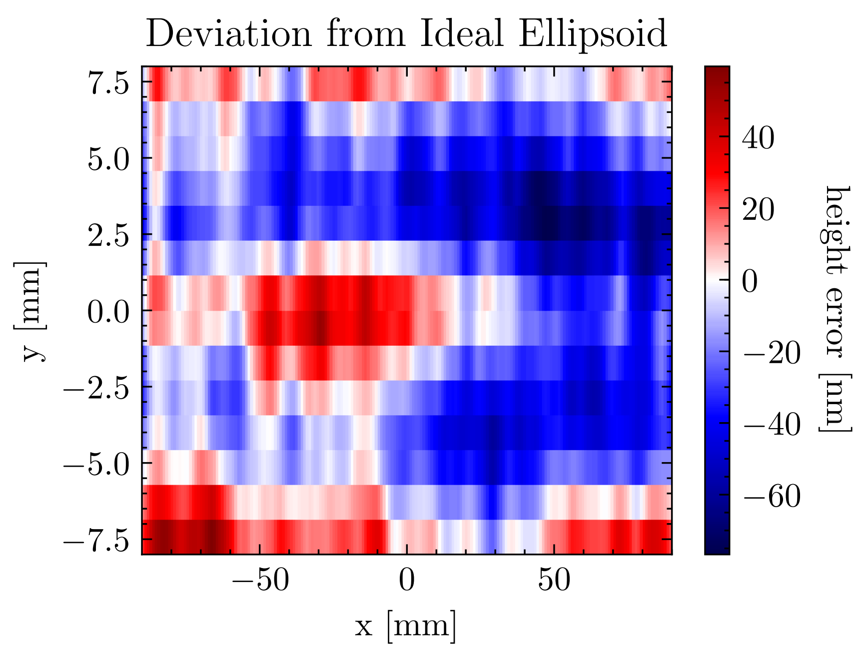


Figure 2.26: Height deviation of our ellipsoidal mirror from an ideal surface, as measured by a Carl Zeiss M400 precision tactile measurement device. Data provided by Carl Zeiss Laser Optics GmbH.

#### Our Ellipsoidal Mirror

We used the results of the previous sections to specify the parameters of our XUV mirror, which can be found in Table 2.2. A picture of the mirror can be seen in Fig. 2.14. A rotational ellipsoid was chosen for its aberration-free focusing when used in a demagnifying geometry. A demagnification factor of $M = 3$ and a grazing angle of 5 degrees were chosen because they represent a compromise between our optical requirements of high flux at high photon energies and the mechanical limitations of a modular beamline. The exit arm was set to be as short as possible while keeping the mirror and target chambers separate, which resulted in an exit arm of 750 mm. A substrate with a 0.3 nm microroughness and a gold coating delivers excellent reflectivity out to 300 eV.

The clear aperture was chosen to match the expected footprint of the harmonics on the optic divergence of the harmonics, which we assumed would have a half-angle divergence of 3.5 mrad. This resulted in a polished region of size $180 \times 16$ mm with an rms roughness of 0.3 nm. A 30 mm border region surrounds this area with a moderately high polish. Zeiss estimates that the surface roughness smoothly increases from the specified 0.3 nm at the edge of the clear aperture to 3 nm at the edge of the substrate.

The finite spatial extent of a physical mirror will result in a range of grazing angles across its surface, as shown in Fig. 2.25. For our mirror, the grazing angle ranges from 4.8 to 5.25 degrees, which does not significantly change the reflectance shown in Fig. 2.19. Finally, the spatially resolved height error is shown in Fig. 2.26, which shows the excellent manufacturing tolerances of our mirror's surface.

### 2.4.4 Metallic Filters

We use a thin metallic filter to block the infrared field after the HHG process (located in chamber $F_1$ in Fig. 2.9). The XUV transmission of the most commonly used filters is shown in Fig. 2.27. Aluminum is favored for experiments below 100 eV, zirconium is useful between 70 and 160 ev, and tin is best above 160 eV.

## 2.5 IR Optics

Next, we discuss the infrared optics used in the generation and pump arms. This includes the optics used for generating harmonics in the generation arm; in the pump arm we have the pulse energy and delay control optics and the focusing optics. We also have the beam splitter and the hole mirror, which mark the beginning and end of the interferometer, respectively.

We wanted the infrared optics to be as achromatic as possible, which would allow us to perform wavelength scans using the TOPAS, or to switch from the signal to the idler or the depeted 800 nm pump without having to completely rebuild the interferometer.

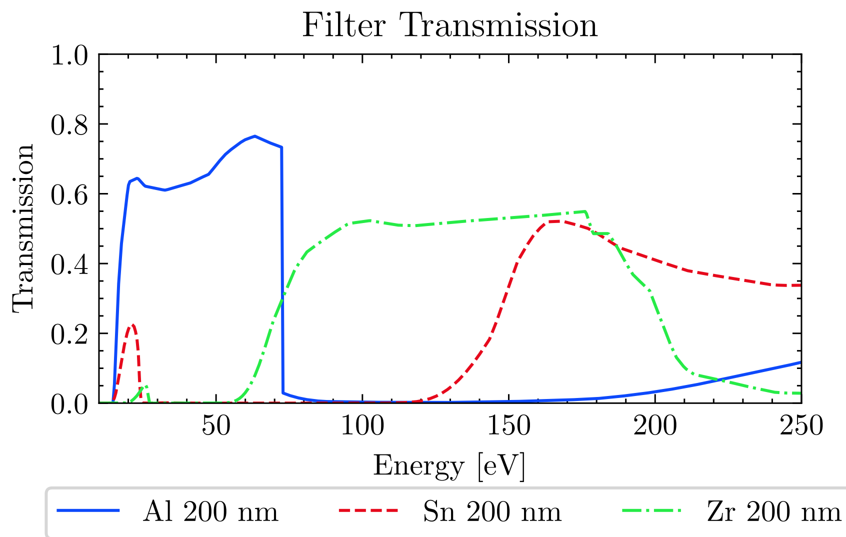


Figure 2.27: Calculated XUV transmission of various metallic filters. Data from [32].

Additionally, we wanted the ability to easily access the pump arm's optics, which meant keeping the pump arm out of vacuum until right before recombination with the XUV arm. This has the extra benefit of allowing future exotic upgrades to the pump arm, such as THz generation, DFG, SHG, etc. With the exception of the hole mirror, all IR optics are outside the vacuum system.

### 2.5.1 The Generation Arm

We use 2" diameter silver optics throughout the beamline unless otherwise specified. As a future upgrade, we purchased high reflectivity dielectric mirrors (Lambda Optics BHR-5012B-1200-1600-45U, coated for $\lambda = 1.2 - 1.6\ \mu$m) for use with the signal wavelengths.

The generation arm takes the transmitted light from a 4/96% beamsplitter (BS, Thorlabs UVFS BSF20-C). A telescope (L1, $f = -300$ mm, L2, $f = +500$ mm) enlarges the beam, allowing for tighter focusing in the generation chamber, which is useful when operating at longer wavelengths. A focusing lens (L3, $f = 400$ mm) and an adjustable aperture (iris) are located immediately before a $CaF_2$ window (3 mm thick) on the entrance flange of the generation chamber. The distance between the outer surface of the $CaF_2$ window and the center of the chamber is 23.8 cm. This geometry supports focal lengths 30 cm or longer outside the chamber. It is possible to mount shorter focal length optics inside the generation chamber using the internal breadboard. There is enough room outside the chamber to implement an $f = 40$ cm reflective focusing setup, but reflective setups using shorter focal lengths will require in-vacuum optics or modifications to the chamber. A metallic filter blocks the IR light about 1 meter after the IR focus (chamber $F_1$ in Fig. 2.9).

A computer controlled home-built shutter (S in Fig. 2.16) is located before telescope. This shutter is used to block the laser, which is useful when performing certain operatings (finding overlap, moving the sample holder in the target chamber, manipulating the filter assembly, etc.).

For experiments that require additional harmonic bandwidth, we insert additional optics (a BBO crystal, 200 $\mu$m of calcite, and a zero-order 1310 nm $\lambda/2$ waveplate) between $L3$ and the vacuum window. When aligned correctly, these optics create a spatially and temporally overlapped $\omega$ and $2\omega$ fields at the focus.

### 2.5.2 The Pump Arm

The pump arm takes the reflected light (4%) from the beamsplitter and propagates in air on the upper deck of the split-level optical table.

A 1 $\mu$m longpass filter (Thorlabs FELH1000, OD $> 5$) is positioned before the waveplate-polarizer assembly to filter out the OPA's visible parasitic wavelengths. This is neccessary to suppress short-wavelength excitation of condensed matter samples. The IR intensity incident on the sample is controlled by a motorized achromatic $\lambda/2$ waveplate (Thorlabs AHWP10M-1600, $\lambda = 1100 - 2000$ nm) and a pair of ultra broadband wire grid polarizers (Thorlabs WB25M-UB, each with a 1000:1 extinction ratio for $\lambda = 0.6 - 4$ $\mu$m) in the pump arm (see Fig. 2.16).

The XUV-IR delay is coarsely adjusted using a retroreflector on a manual translation stage, with $\Delta\tau = 2\Delta x/c = 6.67$ [fs/$\mu$m] $\Delta x$. Motorizing this retroreflector could enable the study of ps-scale dynamics. Fine delay control is achieved by sending the laser through a pair of fused silica (Infrasil) opposing wedges. The insertion amount of one wedge into the beam path is controlled by a stepper motor, while the other wedge is fixed in place. Inserting the wedge by an amount $\Delta x$ increases the thickness of glass in the beam path, delaying the pump arm by an amount $\Delta\tau$ [34]:

$$\Delta\tau = \frac{\Delta x}{c}\left[n\tan\theta - \frac{\sin\theta}{\cos\varphi} - n\tan\theta\left(\frac{\sin(\varphi-\theta)}{\cos\theta}\right)\right] \tag{2.34}$$

where $n$ is the refractive index of the wedge material, $\theta$ is the wedge angle and $\varphi \equiv \arcsin(n\sin\theta)$ is calculated from Snell's law. For $\lambda = 1430$ nm and $\theta = 4.5$ degrees, $n = 1.4454$ [55] and Eq. (2.34) evaluates to:

$$\Delta\tau = \left(102\left[\frac{\text{as}}{\mu\text{m}}\right]\right)\Delta x \tag{2.35}$$

A translation range of $\Delta x = 14$ mm provides a delay range of $\Delta\tau = 1.4$ ps.

During an experiment, the intensity is measured using an InGaAs photodiode (Thorlabs DET10D) mounted with a 2.0 absorptive neutral density filter and 1 $\mu$m longpass filter

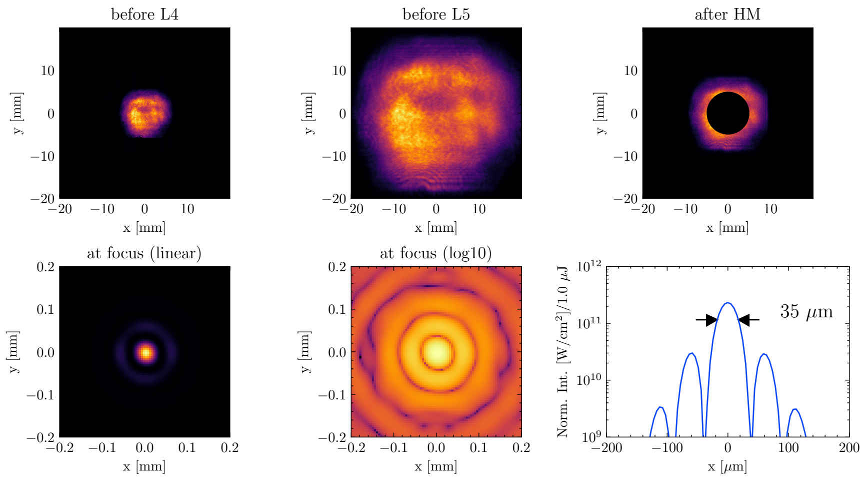


Figure 2.28: Numerical propagation of the IR ($\lambda$=1500 nm) beam through the pump arm. Beam path layout follows Fig. 2.16. Each panel shows the intensity of the beam as the beam propagates towards the focus. The first panel shows the measured intensity (Electrophysics PV320 thermal camera), all other panels are calculations. The arrows on the lineout indicate the FWHM. All calculations are for vacuum ($n = 1$). See text for details.

(Thorlabs FELH1000), which detects light scattered off a mirror in the pump arm and is monitored using an oscilliscope (LeCroy). Absolute measurements of the average IR power are taken with a power meter (Gentek) located before the diverging lens L4. A computer controlled home-built shutter S is located after the photodiode so that the intensity can be adjusted while the pump arm is blocked.

We use a pair of AR-coated N-BK7 lenses ($\lambda = 1050 - 1700$ nm) in the pump arm to minimize the losses from the hole mirror. Diverging lens L4 (Thorlabs LF1015-C, $f = -300$ mm) expands the beam and converging lens L5 (Thorlabs LA1380-C, $f = +500$ mm, located 68.5 cm after L4) focuses it into the target chamber. After L5, the IR beam passes through a 3 mm thick $CaF_2$ window to enter the mirror chamber.

The two arms of the interferometer are combined using a hole mirror (HM), located 53 cm after L5 and 20 cm after the ellipsoidal mirror. The hole mirror is a 2” diameter silver mirror with a 10 diameter aperture in the center [66]. The XUV light passes through the aperture from the backside of the mirror, and the IR light reflects off the annular disk on the front face. This geometry allows us to have a collinear XUV-IR geometry without having to resort to bandwidth limiting XUV-IR optics. However, this geometry clips the center of the IR beam and is responsible for IR diffraction at the focus.

### Calculation of IR intensity at Focus

The spatial profile of the TOPAS output at $\lambda$=1500 nm was measured immediately before the pump arm's diverging lens (L4 in Fig. 2.16) using an Electrophysics PV320 thermal camera. The beam was propagated numerically using the Python package *Lightpipes for Python* [87] through the remainder of the pump arm to the focus using a grid size of $2^{13} \times 2^{13}$. The result of this calculation is shown in Fig. 2.28. Clear apertures of 22.86 mm (L4), 45.72 mm (L5) and 50.8 mm (HM) were used for this calculation. A 65 fs Gaussian temporal profile containing 1 $\mu$J of energy was assumed.

Reflection losses from 2 Ag mirrors, 2 AR-coated lenses and uncoated $CaF_2$ vacuum window are responsible for a 26.2% reduction in transmitted power. Additionally, the geometry of the hole mirror causes only 56% of incident power to be incident on a reflective surface (the rest is lost to the central aperture). In total, the pump arm transmits 41.3% of the power from before L4 to the focus.

The IR intensity makes an Airy-like diffraction pattern at the focal plane. There is an intense bright spot surrounded by a series of rings, with the intensity of each ring as the distance from the center increases. The rings exhibit a periodic modulation in intensity with respect to angle $\phi$. This four-fold symmetry is due to the square-like spatial profile of the TOPAS output, whereas the clipping from the hole mirror's aperture is responsible for the central peak and ring structure. The central lobe has a peak intensity of $\sim 2.3 \times 10^{11}$ W/cm$^2$ per 1 $\mu$J input pulse energy and a FWHM of 35 $\mu$m. The first ring has a radius of 59 $\mu$m and a peak intensity $\sim 2.9 \times 10^{10}$ W/cm$^2$ per input $\mu$J pulse energy. Thus the central lobe's peak intensity is about an order of magnitude larger than the ring's intensity. However, the central spot only contains about 49% of the total power, as the rings cover a much larger area.

Note that the above calculations assume perfect alignment into the hole mirror (i.e., the IR beam is centered on the central aperture of the hole mirror). If the IR beam is misaligned to the hole mirror, then the transmission to the focus will increase as the most intense part of the beam is no longer clipped by the central aperture. Therefore, a drift in the laser's pointing during an experiment can effect the sample's interaction intensity.

## 2.5.3 Aligning into the TABLe Interferometer

We use an Electrophysics PV320 thermal camera for daily alignment into the TABLe interferometer.[5] The camera is located between S and L4, and we use two irises (the 1$^{st}$ is located between BS and CF, the 2$^{nd}$ is located just before S) to define the aligned beam path. Two motorized mirror mounts located on the TOPAS table control the pointing of the input beam. The beam is considered to be aligned when the Airy rings from the partially

[5] Special thanks to Eric Moore who wrote a LabVIEW program to semi-automate this process.

closed 1$^{st}$ iris are centered on the 2$^{nd}$ iris, and when the centroid of the beam is centered on the 2$^{nd}$ iris. Alignment is achieved by iteratively correcting the beam pointing while checking these two metrics.

## 2.6 XUV Photon Spectrometer

### 2.6.1 Optical Description

Below is a brief overview of the XUV photon spectrometer's optics. For a complete description, see [34].

The XUV spectrometer utilizes one of two available concave variable line spaced (VLS) Hitachi gratings, depending on the desired spectral range. Owing to their small grazing angles (1200 lines/mm: 3 deg, 2400 lines/mm: 1.3 deg), they spectrally disperse the light in the horizontal plane while maintaining the vertical spatial profile. The groove spacing is engineered to a flat field across a wide spectral range (1200 lines/mm: 5 - 20 nm, 2400 lines/mm: 1-5 nm). Outside this spectral range, the gratings continue to disperse the light but the focal plane is no longer within the specified flat field. By adjusting the incident angle, we can control both the entrance arm and the flat field spectral range.

The dispersed light hits a 75 mm diameter imaging microchannel plate array (MCP, Photonis) which converts the XUV photons into an electron shower via an avalance process [27, 51]. A type P47 phosphor screen (P, Photonis) converts the spatially-resolved electron shower into light (370 - 480 nm range, peaked at 400 nm), which is sent outside the chamber via a glass window. The MCP-P assembly is mounted directly to an 8" flange, which is connected to the chamber via an edge welded bellows. An external mechanical assembly controls the angle and position of the detector array relative to the grating. The detector position is adjusted in conjunction with the grating's incident angle to make the flat field coincident with the detector plane for a given spectral range.

A computer-controlled digital 16-bit CMOS camera (Andor Neo DC-152Q-C00-FI) is equipped with a Rodagon 50 mm lens and modular focus (QI Optiq) to image the output light of the phosphor. The camera image is recorded to the TABLe computer's hard drive. The camera images have a maximum resolution of $2560 \times 2160$ (6.5 $\mu$m pixel size) with a sensor size of $16.6 \times 14.0$ mm.

**energy resolution of ???, spatial resolution of ??**

### 2.6.2 Spectral Calibration

The photon spectrometer measures XUV counts as a function of position along the camera sensor (i.e., in the spectral pixel basis $p$). Owing to the grating equation, the position in the spectral pixel basis is proportional to the photon wavelength $\lambda$ and inversely proportional to the photon energy $E$. However, the position of the detector relative to the grating (set

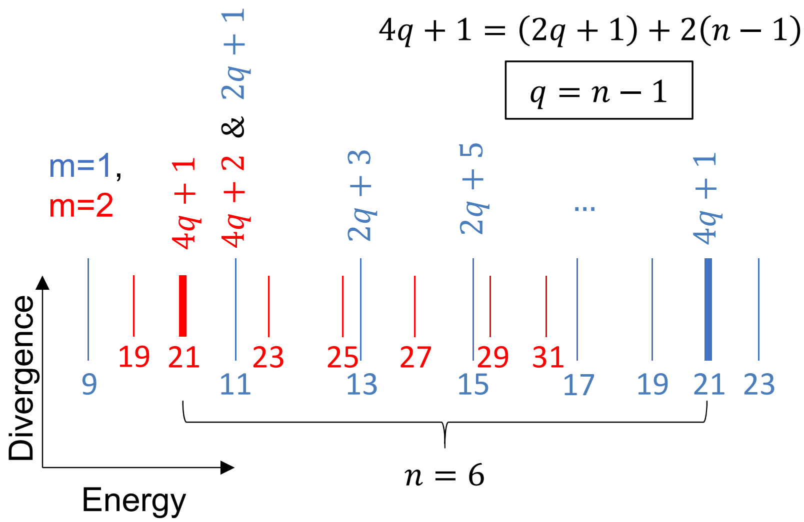


Figure 2.29: Counting scheme to determine the absolute harmonic order. See text for details.

by the cage & crank and the grating's piezo motors) introduces geometric factors which shift and skew the position of the light on the sensor. It is not practical to measure the exact distances between these two elements, so we perform a numerical fit.

Generally speaking, we calibrate the spectrometer by assigning energies $E_i$ to known spectral features in the data located at spectral pixel $p_i$. These features can be absorption features, resonances, or the harmonics themselves. This yields a set of coordinate pairs $\{(p_i, E_i)\}$ that can be fit to a polynomial $E(p)$. Below, we will discuss the methods used to create these coordinate pairs.

### One-Source Harmonic Counting Scheme

The most prominent spectral features on the detector are the harmonics themselves. If we have more than an octave of XUV bandwidth, then we can exploit the grating equation and the regularity of the harmonics to determine the harmonic order of every harmonic on the detector. Below, we will explain this process.

First, consider the grating equation:

$$d(\sin\theta_i - \sin\theta_m) = m\lambda \tag{2.36}$$

where $\theta_i$ is the incident angle, $\theta_m$ is the diffraction angle, $m$ is the diffraction order, and $\lambda$ is the photon wavelength. Inspection of Eq. (2.36) reveals that a light of a particular wavelength will appear at multiple locations on the detector, corresponding to each diffraction order ($m = 1, 2, 3, \ldots$). The grating is designed to deliver most of the light to the 1st order, but an appreciable amount of energy winds up in the 2nd and 3rd orders ($\eta_2 \approx 0.4\eta_1, \eta_3 \approx 0.4\eta_1$) [34, 64].

**question: what is the diffraction order efficiency of m=1, m=2, m=3, etc.? can you get it from the data?**

We will assume that over the spectral region of interest, the wavelength of the $i^{th}$ harmonic is $\lambda_i = \lambda_1/i$, where $\lambda_1$ is the effective fundamental wavelength. That is, we assume that all of the harmonics on the detector have the same fundamental wavelength and are evenly spaced in energy. Furthermore, we will assume that only odd-order harmonics are present during the calibration step.

As a result of the equal harmonic spacing and having more than an octave of XUV bandwidth, there will be regions of the detector that have light from both 1st and 2nd order diffraction. From the grating equation, a 1st order diffraction of the $i^{th}$ harmonic will coincide with the 2nd order diffraction of the $(2i)^{th}$ harmonic. This is shown in Fig. 2.29.

Fig. 2.29 schematically shows the effect of having more than an octave of XUV bandwidth is on the detector. The vertical axis is proportional to divergence (unused in this application) and the horizontal axis is proportional to wavelength, with photon energy increasing to the right. The harmonics are denoted as vertical line segments, with 1st order harmonics colored blue and 2nd order harmonics colored red. In this cartoon, each harmonic order is labeled with its harmonic order, $i = 11, 13, \ldots$, but we have not determined these numbers yet.

If we are able to identify a matched pair of diffraction orders, then we can determine the absolute harmonic order as follows. Let the harmonic order of this matched pair be $i = 4q + 1$. This pair is bolded in Fig. 2.29. If we look at the $m = 2$ copy of the $4q + 1$ harmonic, there will be an $m = 1$ harmonic immediately to the right of it. In $m = 2$ space, this position would correspond to $i_{m=2} = 4q + 2$, which is even. However we are only creating odd harmonics, so this light must be from an odd diffraction order ($m = 1, 3, \ldots$). Of the odd diffraction orders, $m = 1$ is the brightest, so this harmonic order is $i_{m=1} = (4q + 2)/2 = 2q + 1$. We now count the number of $m = 1$ harmonics harmonics between the matched pair (including the right endpoint), which we will call $n$. In doing so, we are counting the number of $m = 1$ harmonics between $i = 2q + 1$ and $i = 4q + 1$. We therefore determine $q$ via the following relation:

$$(m = 1) : 4q + 1 = (2q + 1) + 2(n - 1) \rightarrow q = n - 1 \tag{2.37}$$

In the cartoon, we count $n = 6$ 1st order harmonics (blue line segments) between the bolded matched pair. From Eq. (2.37), we determine that $q = 6 - 1 = 5$, and therefore the matched pair has harmonic order $4q + 1 = 21$. Once we know the numerical value of $4q + 1$, we can label the remaining harmonics sequentially, as shown in the figure.

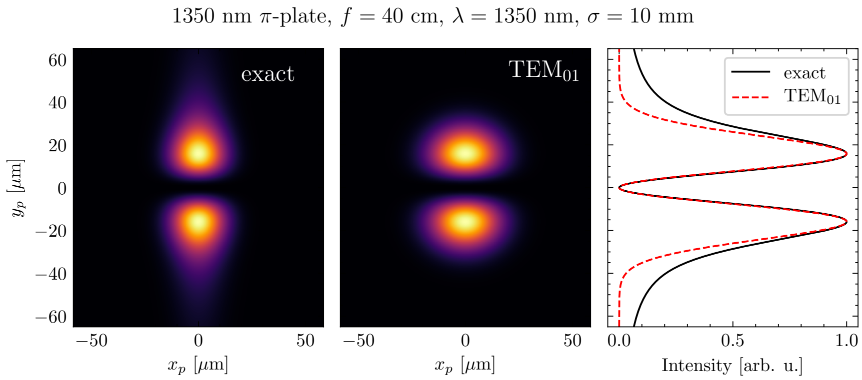


Figure 2.30: Simulation of the $\pi$-plate focus, following Eqs. (2.44) and (2.45).

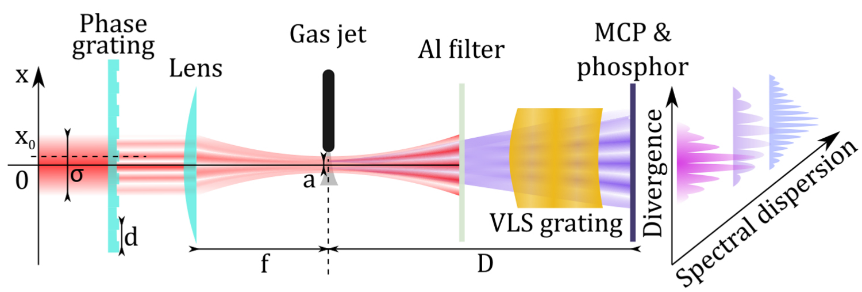


Figure 2.31: Two-source harmonic generation scheme. See text for details. Figure adapted from [12].

At this point, we have a set of $N$ coordinate pairs of spectral pixel and harmonic orders $\{(p_i, HO_i)\}$. We can now fit to a polynomial function and create a functional map between the spectral pixel and the harmonic order, $HO(p)$. If we can identify a single spectral feature located at pixel $p_i$ with a known energy $E_i$, then we can scale the harmonic order function to an energy function: $E(p) = (E_i/HO(p_i)) \times HO(p)$. Usually, the sharp aluminum $L$-edge at 72.3 eV is used for this purpose.

### Two-Source Harmonic Counting Scheme

We can use the divergence axis of the spectrometer to help identify matching pairs of harmonic orders. We do this by inserting a phase mask into the laser beam upstream of the generation lens. It can be shown that if the phase mask is a $0 - \pi$ phase plate (a step function in phase), then the spatial mode will be converted from a Gaussian $\mathrm{TEM}_{00}$ to a $\mathrm{TEM}_{01}$ in the focal plane [10–13, 34].

The phase plate is a planar transmissive optic with a thickness step of size $h$ at its

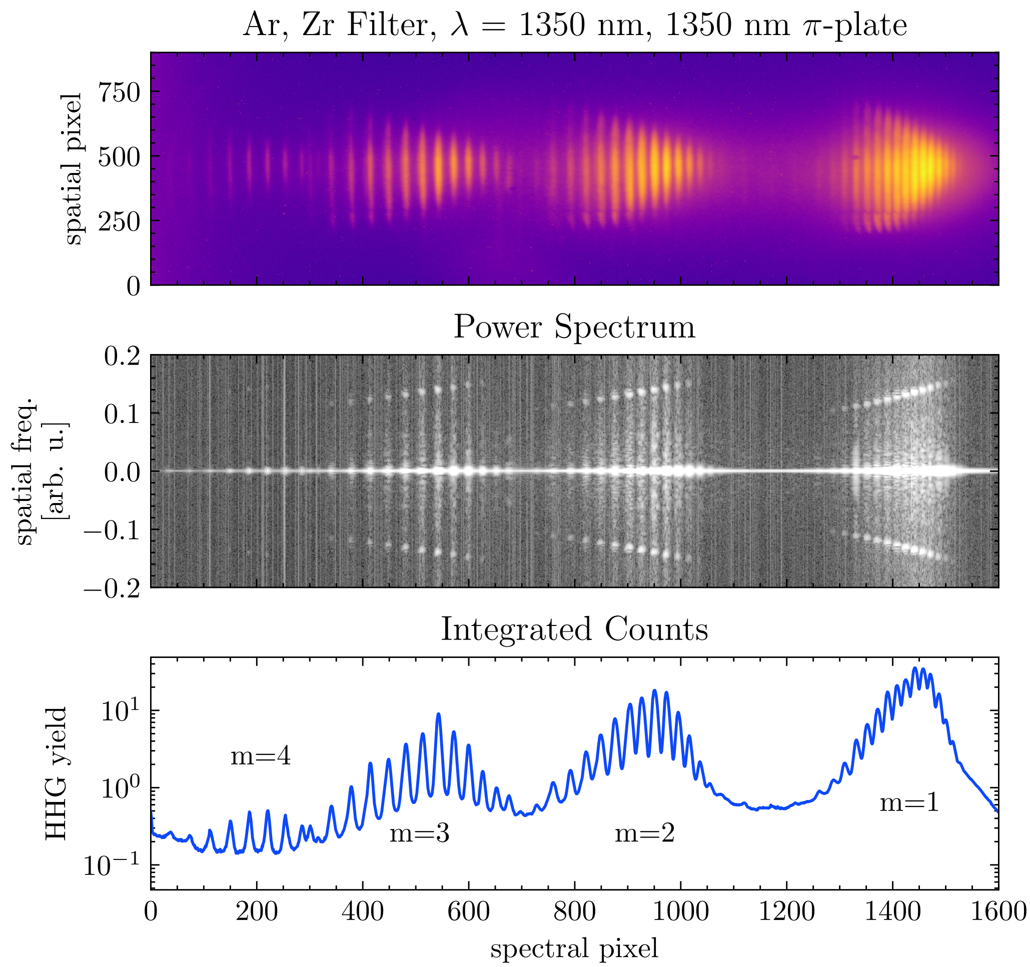


Figure 2.32: Two-source harmonic spectrum. Top panel: log scale 2D detector image. Middle panel: log scale of the power spectrum, computed by taking the FFT of the top panel along spatial dimension. Bottom panel: vertical integration of the top panel.

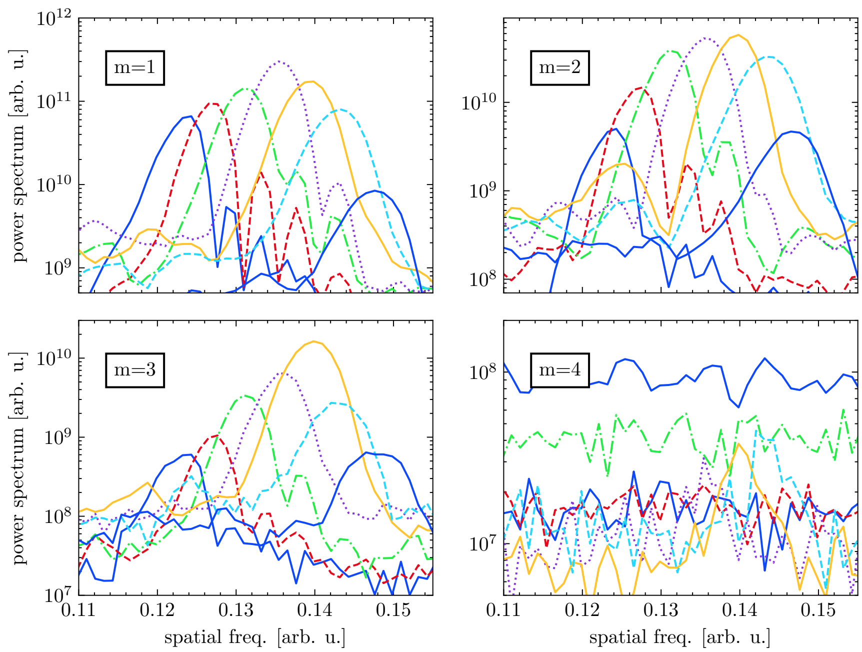


Figure 2.33: Integrated power spectrum (see middle panel of Fig. 2.32) for selected harmonic orders and different diffraction orders. Harmonics with the same spatial frequency are assigned the same color triangle.

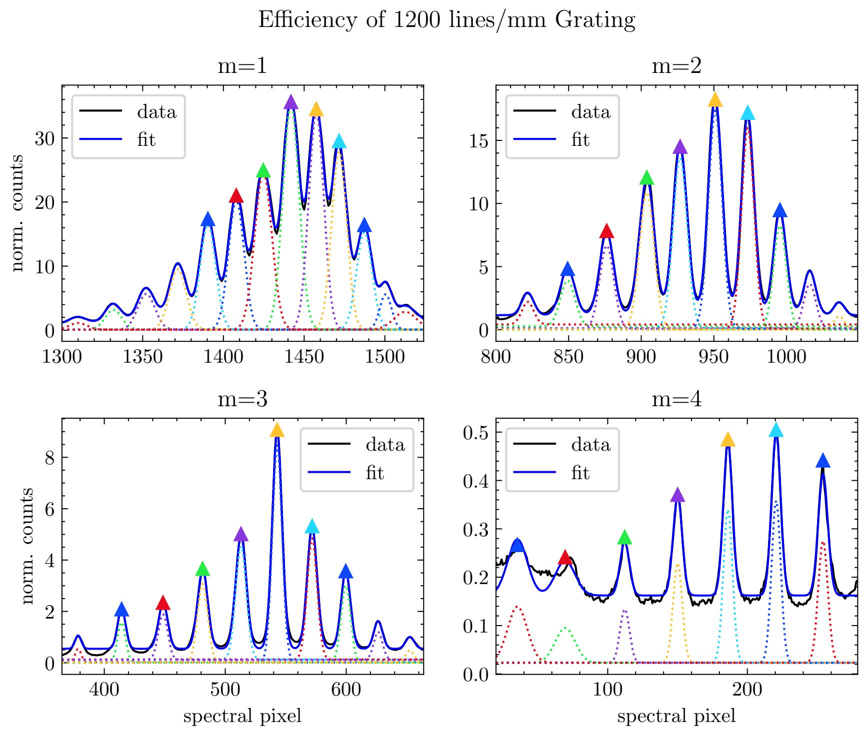


Figure 2.34: Gaussian fit to the spectrum in Fig. 2.32. Triangles indicate the harmonics used in the grating efficiency calculation; matching colors indicate matching harmonic order, following Fig. 2.33.

center. Light passing through the thicker half of the plate experiences a phase shift of $\phi = 2\pi h(n-1)/\lambda$ relative to the light transmitted through the thinner half of the plate, where $n$ is the refractive index of the glass. Ignoring Fresnel losses and absorption, the phase plate has a complex transmittance of $\tau_{pp}$:

$$\tau_{pp}(x,y) = \begin{cases} 1, & \text{for } y > y_0. \\ \exp(-i\phi), & \text{for } y \leq y_0. \end{cases} \tag{2.38}$$

The plate is manufactured so that $\phi = \pi$ for $\lambda = 1350$ nm. Immediately after the phase plate, we place a lens of focal length $f$, which imparts a quadratic phase onto the beam. The complex transmittance of the lens is given by $\tau_L$:

$$\tau_L = \exp\left(-\frac{k}{2f}(x^2+y^2)\right) \tag{2.39}$$

We assume an input laser field that is Gaussian with radius $\sigma$:

$$E_{in}(x,y) = \exp\left[-\left(\frac{x^2+y^2}{\sigma^2}\right)\right] \tag{2.40}$$

We will assume that the laser beam is centered on the phase step ($y_0 = 0$), and we will use scalar diffraction theory to evaluate the electric field at a point $P = (x_p, y_p, z_p)$ located downstream of the phase plate [65]:

$$E(x_p, y_p, z_p) = \frac{i}{\lambda}\int_{+\infty}^{-\infty}\int_{+\infty}^{-\infty} \tau_L(x,y)\tau_{pp}(x,y)E_{in}(x,y)\frac{e^{-ikr}}{r}\,\mathrm{d}x\,\mathrm{d}y \tag{2.41}$$

where $r = \sqrt{(x_p-x)^2 + (y_p-y)^2 + z_p^2}$. We apply the Fresnel and the paraxial approximations:

$$\frac{e^{-ikr}}{r} \approx \frac{1}{z_p}\exp\left[-ik\left(z_p + \frac{(x_p-x)^2+(y_p-y)^2}{2z_p}\right)\right] \tag{2.42}$$

this is valid if $P$ is close to the optical axis (**what are the specific validity requirements?**). With this approximation, we can evaluate the integral Eq. (2.41) and find the intensity $I \propto |E|^2$ at point $P$:

$$\begin{aligned} I(x_p,y_p,z_p) \propto\ & \frac{(fk\sigma^2)^2}{(k\sigma^2(f-z_p))^2 + (2fz_p)^2}\times \\ & \exp\left[-\frac{2(fk\sigma)^2}{((f-z_p)k\sigma^2)^2+(2fz_p)^2}(x_p^2+y_p^2)\right]\times \\ & \left|\mathrm{erfi}\left[\frac{k\sigma f}{\sqrt{2ik\sigma^2(f-z_p)fz_p + (2fz_p)^2}}y_p\right]\right|^2 \end{aligned} \tag{2.43}$$

where $\mathrm{erfi}(x) \equiv -i\,\mathrm{erf}(ix)$ is the complex error function. When evaluated at the focus, the above equation simplifies to the following:

$$I(x_p, y_p, f) \propto \left(\frac{k\sigma^2}{\sqrt{\pi}f}\right)^2 \exp\left[-\left(\frac{k\sigma}{\sqrt{2}f}\right)^2 x_p^2\right] D\left(\frac{k\sigma}{2f}y_p\right)^2 \tag{2.44}$$

where $D(x) \equiv \exp\bigl(-x^2\bigr)\int_0^x \exp\bigl(y^2\bigr)\,\mathrm{d}y$ is the Dawson integral. Note that $D(x)^2$ has maxima at $x \approx \pm 0.924$, so the intensity in the focal plane has maxima at $x_p = 0$ and $y_p \approx \pm 0.294(\lambda f/\sigma)$. An inspection of Eq. (2.44) reveals that it is very similar to the intensity profile of a $\mathrm{TEM}_{01}$ mode with an appropriate choice of the beam waist $w_0$:

$$I_{01}(x_p, y_p, f) \propto \frac{8y_p^2}{w_0^2}\exp\left[-\frac{2(x_p^2+y_p^2)}{w_0^2}\right] \tag{2.45}$$

$$\text{with} \quad w_0 \approx 0.294\sqrt{2}\left(\frac{\lambda f}{\sigma}\right)$$

Eqs. (2.44) and (2.45) are shown in Fig. 2.30.

This technique can also be done using a phase grating, see [34].

It can be shown that if the phase mask is a $0-\pi$ phase plate (a step function in phase), or a $0-\pi$ phase grating, then the spatial mode will be converted from a Gaussian $\mathrm{TEM}_{00}$ to a $\mathrm{TEM}_{01}$ in the focal plane [10–13, 34]. At the focal plane, there will be a series of intensity maxima located at transverse positions $x_i = i\lambda f/d$, where $i$ is the diffraction order of the phase element, $\lambda$ is the fundamental wavelength, $f$ is the focal length, and $d$ is the spatial extent of the input beam (groove spacing) if the phase element is a phase plate (phase grating). Only the $i = \pm 1$ orders contain sufficient intensity to generate harmonics (41% each), and they are separated by a distance $\Delta x = 2\lambda f/d$. By placing a gas jet at the focus, we create two spatially separated phase-locked HHG sources that will interfere in the far field with a spatial frequency $\tilde{k}_q$ [11]:

$$\tilde{k}_q = q\frac{2\pi a}{\lambda_1 D} \tag{2.46}$$

where $D$ is the source-to-screen distance, $a$ is the distance between the two sources, $\lambda_1$ is the fundamental wavelengths.

$n\lambda f/d$, where $n$ is the harmonic order. This is schematically shown in Fig. 2.31. By performing a Fourier transform along the spatial dimension, we can identify matching pairs ($m = 1, 2, 3, 4$) of harmonics. Once we have identified these pairs, we can apply the method described above to find the absolute harmonic order. For more details on two-source harmonic generation, see Stephen Hageman's dissertation [34].

**need more detail / introduction to two-source generation.**

The top panel of Fig. 2.32 shows a harmonic spectrum generated with the 1350 nm $\pi$-plate using argon gas in the low pressure cell (see Section 3.2.4), a fundamental wavelenth of $\lambda = 1350$ nm, a zirconium filter, and an exposure time of 650 seconds. Along the spectral axis, we see four "clusters" of harmonics spanning the horizontal axis. We will show below that each "cluster" corresponds to a different grating diffraction order, with $m = 1$ on the right and $m = 4$ on the left of the sensor. As $m$ increases, the counts decrease and the dispersion changes, but the clusters are otherwise identical to each other. The finite noise floor of the detector limits our ability to resolve the weakest harmonics. Normally, the $m = 3$ and $m = 4$ harmonics are too faint to be seen, but they are visible here due to the combination of the Zr filter (which blocks light below 60 eV, see Fig. 2.27) and an abnormally long exposure time. The cutoff energy of this spectrum is approximately 80 eV.

A discrete Fourier transform (FFT) is performed along the spatial dimension of the data shown in the top panel, and the power spectrum is shown in the middle panel of Fig. 2.32. As discussed above, we expect the spatial frequency of the interference pattern to be proportional to the harmonic energy, and this is exactly what we see. Within a given diffraction order, the spatial frequency increases as the harmonic number increases. Across the harmonic clusters, we see the same increase of spatial frequency with respect to increasing harmonic order, which confirms our suspiscion that each harmonic cluster corresponds to a unique grating diffraction order.

The bottom panel of Fig. 2.32 shows the spatial integration of the detector image. We can see that the efficiency of the grating decreases with increasing $m$, and only a few $m = 4$ harmonics are visible.

Any two harmonic orders with the same dominant spatial frequency must have the same wavelength and therefore must be the same harmonic order. We can use this fact to match harmonic orders across the different diffraction orders. Fig. 2.33 shows the power spectrum, integrated around the width of each harmonic, for seven matching harmonics orders. The $m = 4$ harmonic signal is too weak to resolve most of the spatial frequencies, except for two harmonics.

Now that we have identified matching harmonics, we can calculate the relative grating efficiency, but we must take care in doing so. First, the spectral dispersion is different for each diffraction order, so the height of the harmonic is not a valid metric – we must use the integrated harmonic yield[6]. Secondly, only a few $m = 4$ diffraction orders are visible, so we should take care to integrate over the same spectral region for each diffraction order. Finally, the harmonics overlap each other, and we can see the amount of overlap varies for each diffraction order – so we can't just numerically sum the signal over a discrete number of harmonics. We get around this problem by fitting the harmonic spectrum to a sum of Gaussians and using the fitted values to analytically integrate the contribution of a subset of common harmonics.

[6]Note that for this calculation, there is no need to include the Jacobian or convert the spectral axis to the energy basis, as the following quantity is conserved: $\int f_p(p)\,\mathrm{d}p = \int f_E(E)\,\mathrm{d}E$. See below for a more detailed disccusion.

This analysis is shown in Fig. 2.34. For each diffraction order, we fit the spectra to a series of Gaussians (dashed lines, each of the form $y_i = a_i \exp\left[(x-b_i)^2/(2c_i^2)\right] + d_i$). The matching harmonics, identified in Fig. 2.33, are indicated with red triangles. For each diffraction order, we integrate the total yield of the tagged harmonics via $\eta_i = \Sigma_i \sqrt{2\pi} a_i |c_i|$. Next, we calculate the grating efficiency (relative to the $m = 1$ diffraction). The result is:

$$\frac{\eta_2}{\eta_1} = 42.2\%$$
$$\frac{\eta_3}{\eta_1} = 13.0\%$$
$$\frac{\eta_4}{\eta_1} = 0.6\%$$

If we ignore the contributions of higher diffraction orders ($1 = \Sigma_{i=1}^{4}\eta_i$), then we can calculate the absolute diffraction efficiency of the grating:

$$\eta_1 \simeq 64.2\%$$
$$\eta_2 \simeq 27.1\%$$
$$\eta_3 \simeq 8.4\%$$
$$\eta_4 \simeq 0.4\%$$

**Argon Fano Resonances**

argon fano resonances - what are they?

fano cross section $\sigma$:

$$\sigma = \frac{(q+\epsilon)^2}{1+\epsilon^2}\sigma_a + \sigma_b \tag{2.47}$$

where $\sigma_a$ is the intensity of the resonance and $\sigma_b$ is the background scattering, $q$ is the asymmetry parameter and $\epsilon$ is defined as:

$$\epsilon = \frac{\hbar\omega - E_r}{\Gamma/2} \tag{2.48}$$

where $\hbar\omega$ is the photon energy, $E_r$ is the resonance energy and $\Gamma$ is the width. this resonance has extrema at photon energies:

$$\hbar\omega = E_r + \frac{\Gamma}{2q} \tag{2.49}$$

$$\hbar\omega = E_r - \frac{q\Gamma}{2} \tag{2.50}$$

We can see two Fano resonances in the Fig. 2.35, corresponding to $n = 4, 5$ in the $3s3p^6np$ resonance series.

references for this section: [14, 81]

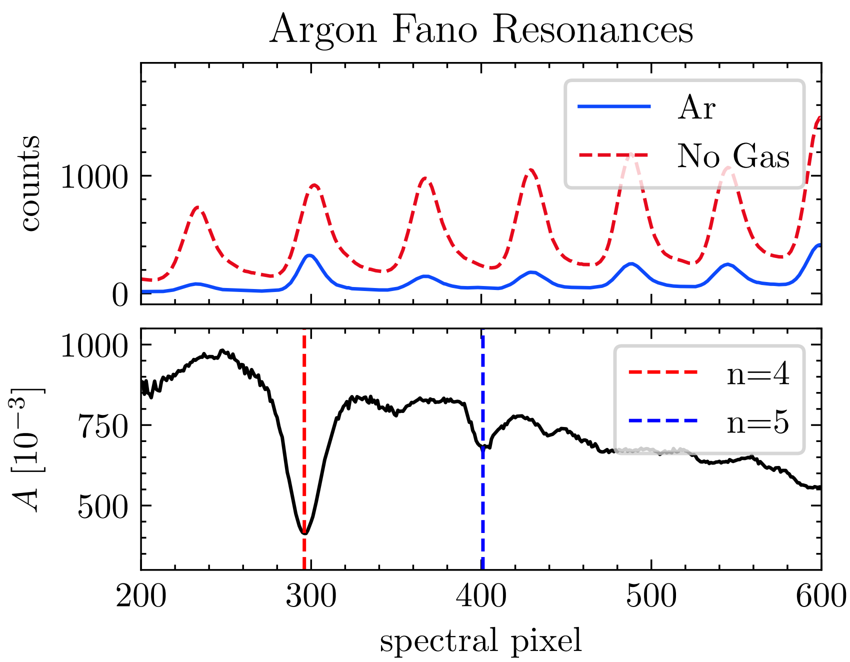


Figure 2.35: Fano resonances used for calibration. Top panel: XUV spectra with and without argon gas in the XUV focus (target chamber). Bottom panel: measured absorbance $A$ of argon showing the prominent $n = 4$ and $n = 5$ $3s3p^6np$ resonances.

### The Jacobian

Once we have the calibration function, we need to scale the measured signal by the Jacobian in order to conserve energy [59]. Let $f_p(p)$ be the function that represents the measured XUV counts at spectral pixel $p$:

$$f_p(p): \text{ spectral pixel} \rightarrow \text{counts} \tag{2.51}$$

During the calibration step, we convert the spectral pixel axis to energy [eV] using a function $E(p)$, usually a polynomial:

$$E(p): \text{ spectral pixel} \rightarrow \text{energy [eV]} \tag{2.52}$$

$$E(p) = a_0 + a_1 p + a_2 p^2 + a_3 p^3 + a_4 p^4 + ... \tag{2.53}$$

Likewise, we define the inverse of $E(p)$ to be:

$$p(E): \text{ energy [eV]} \rightarrow \text{spectral pixel} \tag{2.54}$$

$$p(E) \equiv E^{-1}(p) \tag{2.55}$$

We want calculate the XUV counts in the energy basis. That is, we want to convert $f_p(p)$ to $f_E(E)$ using the Jacobian. By conservation of energy, we have the relation:

$$f_p(p)\,\mathrm{d}p = f_E(E)\,\mathrm{d}E \tag{2.56}$$

Rearangement of the above equation leads us to the desired result:

$$f_E(E) = f_p(p)\frac{\mathrm{d}p}{\mathrm{d}E} = f_p(p)\frac{\mathrm{d}}{\mathrm{d}E}p(E) \tag{2.57}$$

# Chapter 3
# XUV Light Source Design and Apparatus Performance

## 3.1 Introduction

Compared to RABBITT measurements, condensed matter transient absorption experiments require a high XUV photon flux. First, the sample thickness is usually chosen such that the XUV transmission is roughly 50% near the spectral feature of interest. This optical density represents a compromise between the incompatible goals of having a strong ground state absorption (enabling the detection of small changes in the optical density) while simultaneously avoiding the noise floor of the detector (which is required for good statistics). Second, a high XUV flux will reduce the number of laser shots required for a given data point, which in turn reduces the total IR flux on the sample and minimizes sample heating. Finally, a high flux reduces the overall time required to complete an experiment. This increases data fidelity by reducing the effects of unavoidable experimental noise sources such as long-term laser drift (either pointing or energy) and environmental changes caused by the building's HVAC system.

This chapter will detail the developement of bright XUV sources which were required for ATAS experiments. It will also quantify the performance of the available XUV sources and the TABLe beamline as a whole.

## 3.2 HHG Gas Sources

### 3.2.1 Scaling of Harmonic Yield

you have a discussion of the scaling in chapter 1. consider deleting this section, or moving chap1's discussion to this location.

### 3.2.2 Gas Flow Considerations

- pressure in chamber requires a balance of pumping speed and gas throughput

- different gas source geometries are available: free expansion nozzle, LPC, HPC, amsterdam valve

Depending on the energy of the spectral feature, obtaining a high photon flux can range from trivial to challenging. There are many (usually interdependent) experimental parameters (gas type, interaction pressure and length, wavelength, intensity, confocal parameter, focal position relative to gas source, etc.) that can be tuned to optimize photon flux. Physically, these parameters can change the microscopic single atom response, the macroscopic coherent addition of dipole emitters (via phase matching), or both. Each experiment will usually require a unique combination of experimental settings to achieve a usable light source. For example, optimizing the harmonic yield at 100 eV for a Si L-edge measurement will usually come at the expense of harmonics yield in the 30-50 eV range, which are used to measure the transition metal M-edges.

In general, an experimentalist has neither perfect knowledge nor control over all the variables that contribute towards phase matching. Setting aside the complicated topic of phase matching, the one dimensional on-axis phase matching model[19] shows that the photon flux is proportional to the square of the pressure-length product of the interaction gas. That is, so long as we can remain phase matched and below the critical phase matching pressure[71], we can universally increase the harmonic flux of our experiments by increasing the pressure-length product.

Unfortunately, one cannot ignore phase matching. Oftentimes, the spectral feature of interest lies beyond the harmonic cutoff when using the more convenient shorter wavelengths. In this case, the fundamental wavelength is increased to extend the cutoff (which scales as $\lambda^2$). However, the critical phase matching pressure also scales as $\lambda^2$ [71], and the single atom response scales as $\lambda^{-(5-6)}$ [85]. These two combined effects result in a dramatically decreased photon flux if intensity and pressure are kept constant with increasing wavelength, often to the point that the resulting flux is insufficient for a transient absorption experiment, even though your cutoff has been extended to the proper energy. While some of the flux can be recovered by increasing the backing pressure of the continuous free expansion nozzle, the generation chamber's finite pumping speed limits the efficacy of pressure tuning at the longer wavelengths. Even at 800 nm, the maximum backing pressure of the continuous free expansion nozzle results in an interaction pressure below the critical phase matching pressure. Practically speaking, the continuous free expansion gas nozzle is not suitable for transient absorption experiments using the signal wavelengths ($\lambda > 1.6$ $\mu m$) or with spectral features greater than the aluminum edge at 72 eV.

Providing the lab with a brighter harmonic source was the ultimate goal of the high pressure cell, and for the most part this goal was achieved. Below, we will review the basic design considerations, drawbacks and advantages of the four main types of gas sources used in this thesis: the free expansion nozzle, the low pressure cell (LPC), the high pressure cell

| Source | $j$ | $\gamma$ | $C_1$ | $C_2$ | $C_3$ | $C_4$ | $A$ | $B$ |
|---|---|---|---|---|---|---|---|---|
| 3D | 1 | 5/3 | 3.232 | -0.7563 | 0.3937 | -0.0729 | 3.337 | -1.541 |
| 3D | 1 | 7/5 | 3.606 | -1.742 | 0.9226 | -0.2069 | 3.190 | -1.610 |
| 3D | 1 | 9/7 | 3.971 | -2.327 | 1.326 | -0.311 | 3.609 | -1.950 |
| 2D | 2 | 5/3 | 3.038 | -1.629 | 0.9587 | -0.2229 | 2.339 | -1.194 |
| 2D | 2 | 7/5 | 3.185 | -2.195 | 1.391 | -0.3436 | 2.261 | -1.224 |
| 2D | 2 | 9/7 | 3.252 | -2.473 | 1.616 | -0.4068 | 2.219 | -1.231 |

Table 3.1: Gas parameters used in Eq. (3.3). Table recreated from Ref [58].

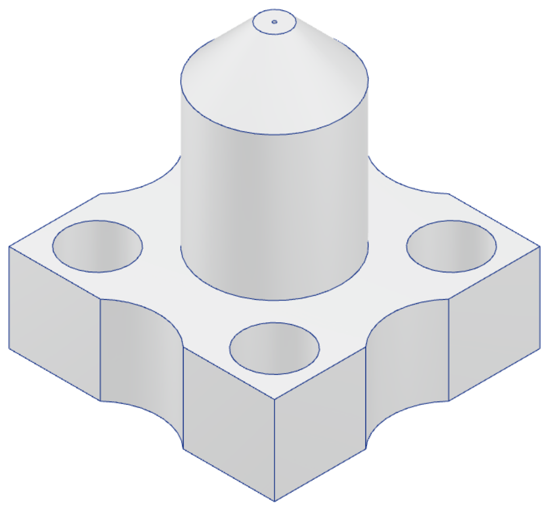

Figure 3.1: Rendering of the continuous free expansion nozzle. Gas flows from the base of the nozzle (bottom) and out of the 200 $\mu$m aperture (top). The top surface is beveled so the nozzle can be brought closer to the IR focus without clipping the beam.

(HPC) and the Amsterdam pulsed piezovalve. A primer on how to install and use the high pressure cell can be found in Appendix A.

### 3.2.3 Free Expansion Nozzle

We use an *in vacuo* gas nozzle to deliver a localized plume of gas near the IR focus. Generally, when gas flows from a high pressure region ($P_0$) to a low pressure region ($P_b$) through a small aperture of diameter $d$, a supersonic plume may form in the low pressure region. If the pressure ratio $P_0/P_b$ exceeds a critical value $G$, given by

$$G \equiv ((\gamma+1)/2)^{\gamma/(\gamma-1)} \leq 2.1, \tag{3.1}$$

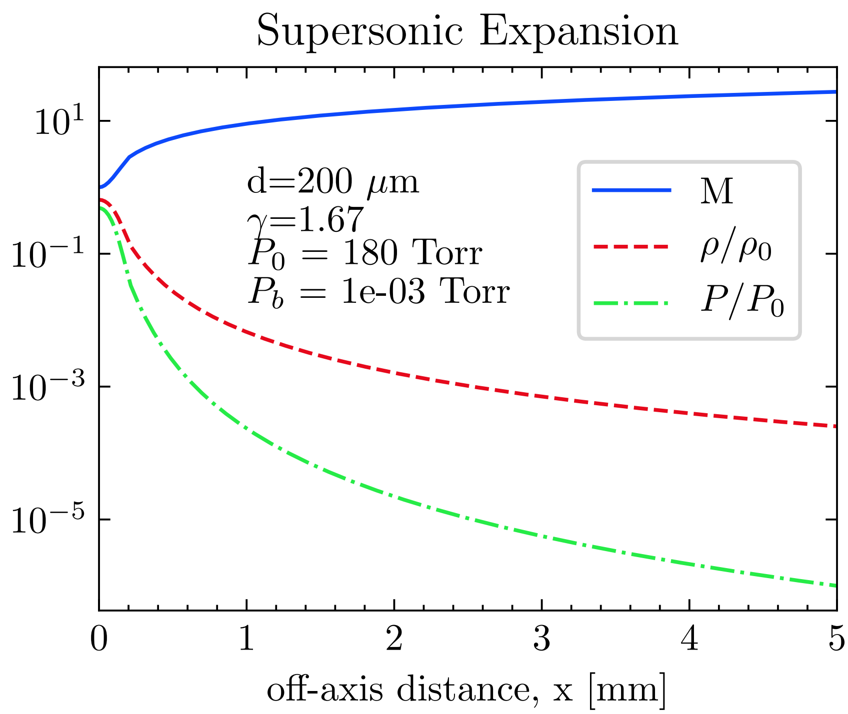


Figure 3.2: On-axis Mach number $M$, mass density $\rho$ and pressure $P$ for a free expansion nozzle.

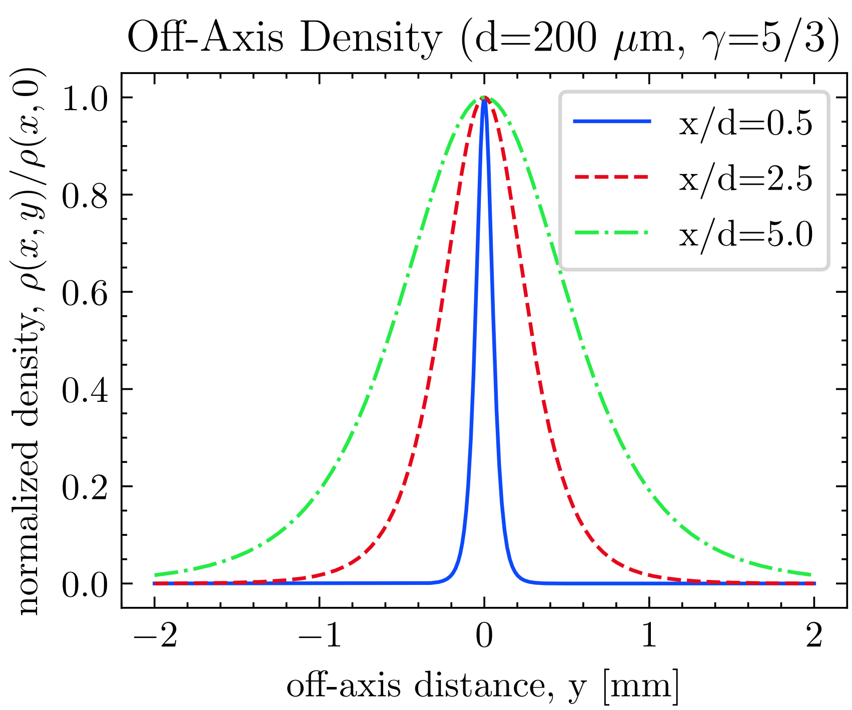


Figure 3.3: Off-axis mass density $\rho(x, y)$ for various on-axis distances $x$. For an aperture size of $d = 200$ $\mu$m, the FWHM of the plume density is 120 $\mu$m at $y = 100$ $\mu$m.

then the gas flow at the aperture will be equal to the speed of sound, and the pressure will be equal to $P_0/G \approx P_0/2$. The highest chamber pressures in our experiments are on the order of $P_b \approx 10$ mTorr, and typical backing pressures for harmonic generation generally exceed 50 Torr, so we are always operating with a supersonic jet. The on-axis spatial extent of the supersonic gas plume is given by the Mach disk location, given by $x_M/d = 0.67\sqrt{P_0/P_b}$. For a chamber pressure of 3 mTorr and a backing pressure of 450 Torr, $x_M = 260d = 51.9$ mm for a 200 $\mu$m diameter aperture. As will be shown below, our laser-gas interaction region is well within the structure of the gas jet.

The physics of supersonic gas flow have been discussed at length in the literature, so we will only go over the revelant highlights [58]. The ratio of the velocity of the gas $V$ to the speed of sound $a$ is called the *Mach number* $M = V/a$. It can be shown that all thermodynamic parameters within the supersonic structure (density, pressure, velocity and temperature) can be expressed in terms of the Mach number and the heat capacity ratio $\gamma$. For harmonic generation, we are primarily concerned with the on-axis ($y = 0$) mass density $\rho$ and pressure $P$:

$$\frac{\rho}{\rho_0} = \frac{n}{n_0} = \left(\frac{T}{T_0}\right)^{1/(\gamma-1)} = \left(1 + \frac{\gamma-1}{2}M^2\right)^{-1/(\gamma-1)} \tag{3.2a}$$

$$\frac{P}{P_0} = \left(\frac{T}{T_0}\right)^{\gamma/(\gamma-1)} = \left(1 + \frac{\gamma-1}{2}M^2\right)^{-\gamma/(\gamma-1)} \tag{3.2b}$$

Here, $\rho_0$ is the mass density at the nozzle aperture ($x = 0$), and $n$ is the number density. The Mach number is found by solving the fluid mechanics equations dealing with the conversation of mass, momentum and energy for a given nozzle geometry. For a complete discussion, see [58]. Below we present the on-axis result, which is an analytic fit to a numerical solution of the thermodynamic equations:

$$\frac{x}{d} > 0.5: \qquad M = \left(\frac{x}{d}\right)^{(\gamma-1)/j}\left[C_1 + \frac{C_2}{\left(\frac{x}{d}\right)} + \frac{C_3}{\left(\frac{x}{d}\right)^2} + \frac{C_4}{\left(\frac{x}{d}\right)^3}\right] \tag{3.3a}$$

$$0 < \frac{x}{d} < 1.0: \qquad M = 1.0 + A\left(\frac{x}{d}\right)^2 + B\left(\frac{x}{d}\right)^3 \tag{3.3b}$$

The fitting coefficients for Eq. (3.3) are listed in Table 3.1. We can see that $M$ scales with powers of $x/d$, the number of nozzle diameters away from the nozzle aperture. Likewise, the off-axis density $\rho(x, y)$ is given by:

$$\frac{\rho(x,y)}{\rho(x,0)} = \cos^2\theta\cos^2\left(\frac{\pi\theta}{2\phi}\right) \tag{3.4}$$

$$\tan\theta \equiv \frac{y}{x} \tag{3.5}$$

where $y$ is the distance from the centerline axis, and $\phi$ is a gas constant with values

$\phi = 1.365, 1.662$, and 1.888 for $\gamma = 5/3, 7/5$ and 9/7, respectively.

The gas nozzle throughput $\hat{T}$ is proportional to the area of the aperture and the backing pressure:

$$\hat{T}\ (\text{Torr} \cdot \text{l/s}) = C \left(\frac{T_C}{T_0}\right) \sqrt{\frac{300}{T_0}} P_0 d^2 \tag{3.6}$$

where $C$ is a gas constant[7], $T_C$ and $T_0$ are the vacuum chamber and backing temperatures, respectively, and $d$ is the nozzle diameter in cm. Ignoring the effect of the generation chamber's vacuum aperture, we can estimate the operating pressure of the generation chamber using the following equation [33]:

$$P_b\ (\text{Torr}) = \frac{\hat{T}}{S} \tag{3.7}$$

where $S$ is the pumping speed of the turbo pump. To avoid overloading our turbo pumps, we are limited to operating pressures below 5 - 10 mTorr.

The basic design of our continuous free expansion nozzle is shown in Fig. 3.1. The nozzle is an aluminum cylinder with a small diameter hole drilled into the top surface. Gas is delivered to the aperture via a universal gas receiver, which attaches to base of the nozzle. To reduce the gas load on the pumps, we used 200 $\mu m$ diameter aperture, which was the smallest size hole the machine shop could readily drill into aluminum. A 200 $\mu$m diameter aperture backed with 180 Torr of argon will deliver a gas throughput of approximately 1 Torr $\cdot$ l/s. With a pumping speed of $S = 1000$ L/s, the generation chamber pressure will be around $P_b = 1$ mTorr. For a monatomic gas, $G = 2.05$, and the pressure at the nozzle aperture is $P_0/G \approx 87$ Torr.

The on-axis Mach number, density and pressure for a monoatomic gas are shown in Fig. 3.2. We can see the on-axis gas density drops off precipitously with increasing distance from the nozzle $x$. Recalling Fig. 1.7, we want to bring the nozzle as close to the optical axis to maximize the interaction density. However, if nozzle face enters the focal volume it will be drilled by the high intensity light and the resulting metallic plume will coat the generation chamber's vacuum window. Under normal operating conditions, we estimate the optical axis is located at $x = 100$ $\mu$m. Using the numbers from our previous example, this gives us an argon interaction pressure of about 45 Torr and a number density of $2.67 \times 10^{24}$ m$^{-3}$.

The normalized off-axis gas density is shown in Fig. 3.3. At $x/d = 0.5$, the FWHM of the density is $L_{med} = 120$ $\mu$m, which is smaller than the width of the laser spot size ($w_0 \sim 30$ $\mu$m), and the Rayleigh range ($z_R \sim 300$ $\mu$m).

We can now calculate the absorption length $L_{abs} = 1/\rho\sigma$ for this jet. The photoabsorption cross section is relatively constant for argon in the range 45 - 150 eV [32]. For argon at 100 eV, $\sigma = 2r_0\lambda f_2 = 1.3 \times 10^{-4}$ nm$^2$. Therefore the absorption length of the gas jet

[7] Values of $C$ for common species are listed here: 45 [He], 20 [Ne], 14 [Ar], 16 [$N_2$] l/cm$^2$/s. For a full table of values, see Table 2.5 in [58].

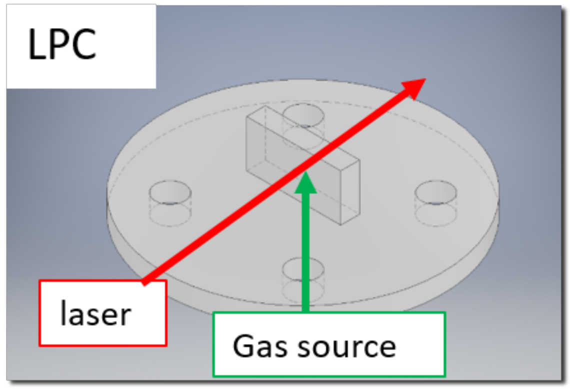


Figure 3.4: Rendering of the low pressure cell (LPC).

backed by 180 Torr of argon is $L_{abs} = 2.9$ mm, and $L_{med}/L_{abs} = 0.04$. Referring back to Fig. 1.7 and Eq. (1.42), we can see that we are well within the quadratic regime of the HHG reabsorption model, regardless of the coherence length $L_{coh}$. Increasing the backing pressure by a factor of 5 will yield only $L_{med}/L_{abs} = 0.20$, still within the quadratic regime. This leaves significant room for HHG yield improvement.

### 3.2.4 Low Pressure Cell

The interaction region of the free expansion nozzle would have much higher pressures if the laser could be sent down the symmetry axis of the gas plume, but this is not possible given the nozzle's geometry. The low pressure cell (LPC), shown in Fig. 3.4, was designed to solve this problem.[8] The LPC consists of an aluminum disk with rectangular block at the center of the top surface. Gas flows from the universal gas receiver (which is mated to the bottom of the disk) through a thin capillary and into the rectangular block. A through hole drilled into the front face of the rectangular block intersects the capillary and serves as the gas-laser interaction volume. Below, we will model the gas density profile of the LPC and show that the thickness of the block ($W = 2.032$ mm) sets the gas-laser interaction length.

#### Calculating the Interaction Pressure

Fig. 3.5 shows a gas flow model of the LPC. The green arrows indicate the direction of gas flow, and the red shaded region indicates the laser focus. The gas receiver is considered to be an infinite reservoir of gas with pressure $P_1$. This region supplies the laser interaction region with gas via a thin capillary of diameter $R = 101.5$ $\mu$m, length $L = 5$ mm and volumetric flow rate $Q_2$, modelled as an ideal isothermal gas [28, 53, 88]. The interaction

[8] Special thanks to Zhou Wang [90] for designing the original LPC. The LPC used in this work has been slightly modified to work with our universal gas receiver.

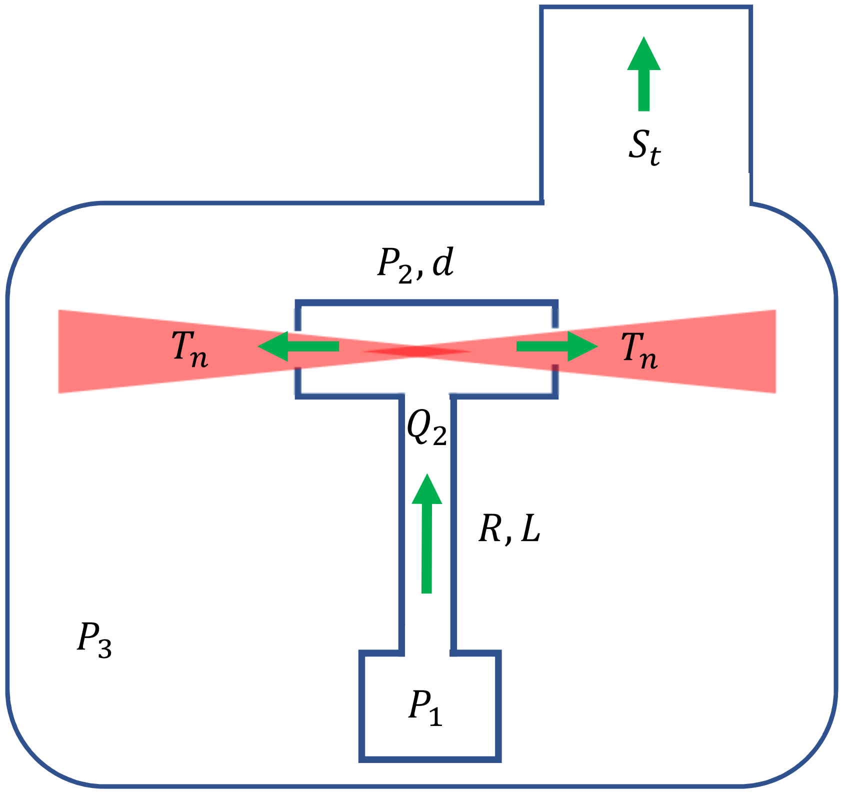


Figure 3.5: Gas flow schematic of the LPC.

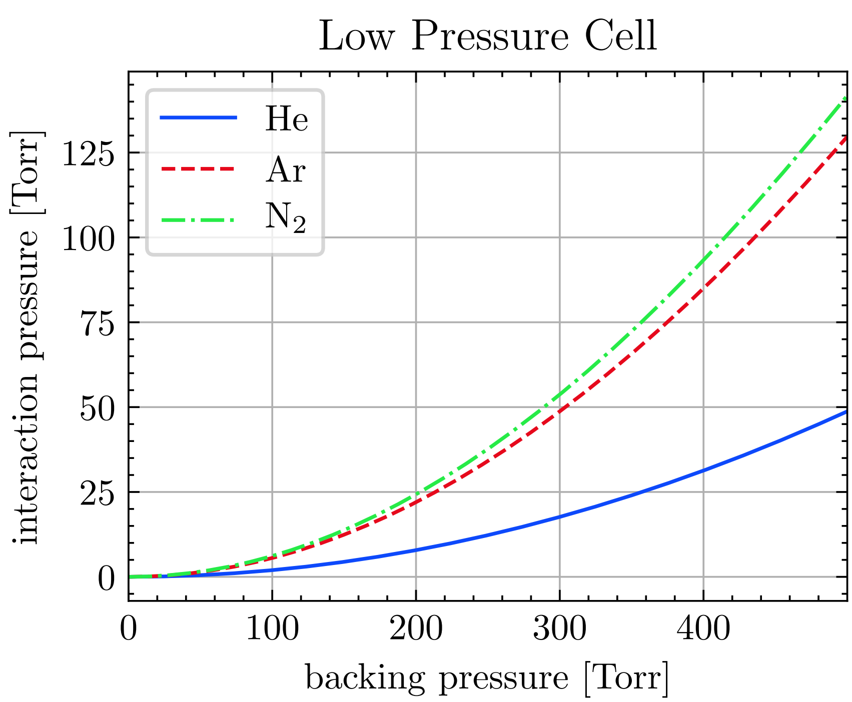


Figure 3.6: Calculated pressure in the LPC interaction region.

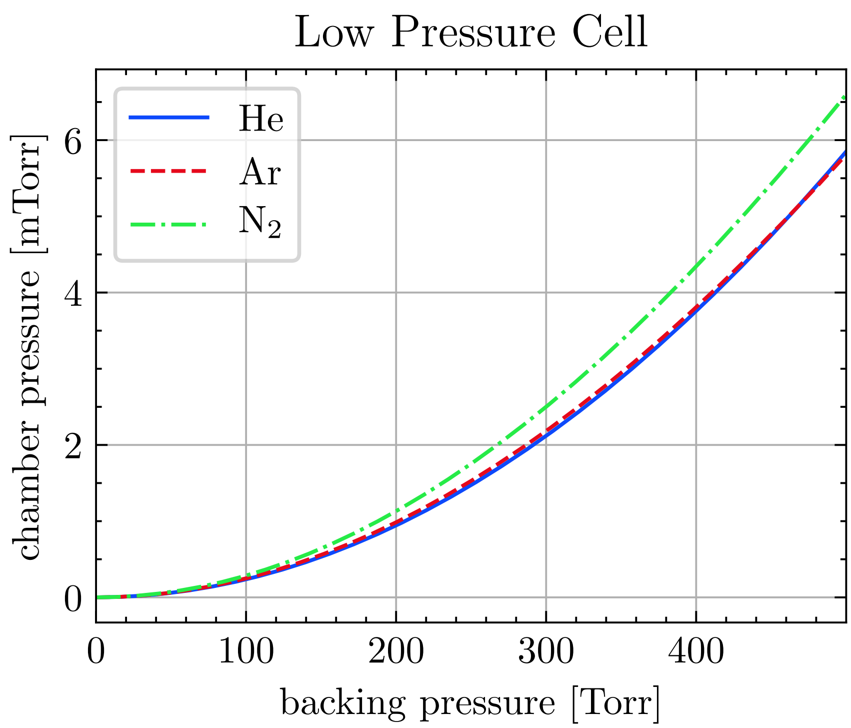


Figure 3.7: Calculated pressure in the target chamber using the LPC.

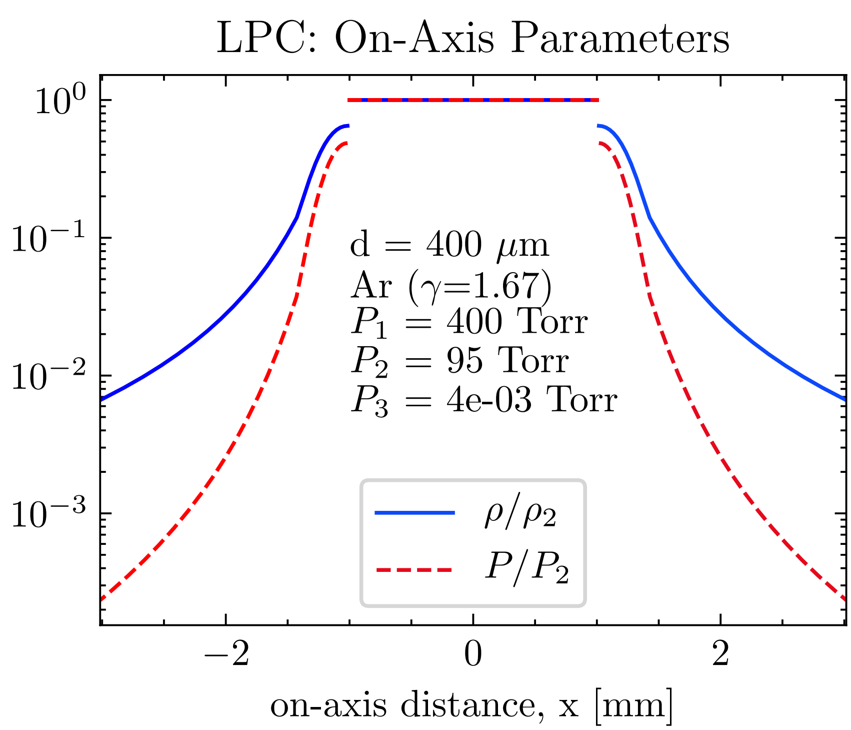


Figure 3.8: On-axis density and pressure for the low pressure cell.

region with pressure $P_2$ acts as a pressure source for two diametrically opposed supersonic gas jets [58], each with diameter $d = 400\ \mu$m and throughput $\hat{T}_n$. The generation chamber has a turbopump with pumping speed $S_t$ and an equilibrium pressure $P_3$. This results in the following coupled equations (SI units):

$$p_1^2 - p_2^2 = \frac{16\mu L Q_2 p_2}{\pi R^4} \tag{3.8}$$

$$Q_2 p_2 = 2T_n \tag{3.9}$$

$$p_3 = \frac{2\hat{T}_n}{S_t} \tag{3.10}$$

$$\hat{T}_n = c p_2 d^2 \tag{3.11}$$

where $c$ is a gas constant expressed in m/s (see Eq. (3.6)) and $\mu$ is the dynamic viscosity in Pa s. Solving for the interaction pressure $p_2$ and chamber pressure $p_3$, we obtain:

$$p_2 = -\frac{16cd^2 L\mu}{\pi R^4} + \sqrt{p_1^2 + \frac{256c^2 d^4 L^2 \mu^2}{\pi^2 R^8}} \tag{3.12}$$

$$p_3 = \frac{2cd^2}{S_t}\left(-\frac{16cd^2 L\mu}{\pi R^4} + \sqrt{p_1^2 + \frac{256c^2 d^4 L^2 \mu^2}{\pi^2 R^8}}\right) \tag{3.13}$$

These functions are shown in Figs. 3.6 and 3.7. Experimentally, we are limited to backing pressures of about 400 Torr or less in the LPC, which yields interaction pressures below 100 Torr for argon or nitrogen, and below 30 Torr in helium. Somewhat counterintuitively, the interaction pressure is lower for helium than the other species for a given backing pressure. This is because helium has a larger value of $c$ that prevents it from being trapped in the interaction region.

Eq. (3.2) can be used to calculate the on-axis density and pressure of the LPC, which are shown in Fig. 3.8. Note that due to the $G$ factor (Eq. (3.1)), the FWHM of the pressure and density is simply the width of the LPC's rectangular block: $L_{med} = 2.032$ mm. Due to the negligible gas density outside of the interaction region, we will treat the gas density as a boxcar function with a thickness $L_{med} = 2.032$ mm set by dimensions of the rectangular block.

When operating at maximum backing pressure, the maximum absorption length for the LPC at 100 eV in argon is identical to that of the free expansion jet: $L_{abs} = 0.6$ mm. However, the longer interaction length of the LPC yields a much higher ratio $L_{med}/L_{abs} = 3.5$.

justification for treating the gas thru hole as two diametrically opposed gas jets. compare the mean free path of $p_2$ region to the thickness of the rectangular block. note that we are in the supersonic regime, since p2 is more than 2x p3.

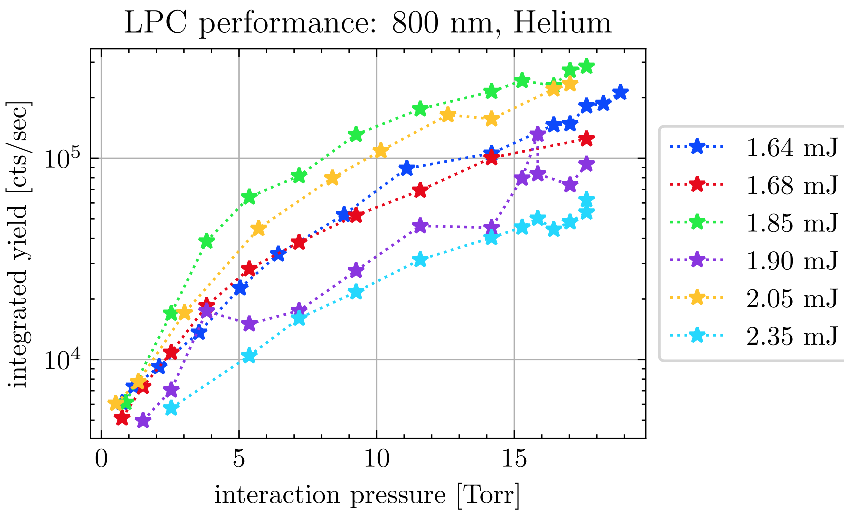


Figure 3.9: Total harmonic yield of the LPC as a function of interaction pressure.

**HHG in LPC**

**compute absorption length, Lmed/Labs for helium**

Fig. 3.9 shows the pressure scaling of the LPC when using an 800 nm pulse and helium gas. The interaction pressure is calculated from the backing pressure and the geometry of the nozzle using Eq. (3.13). From this figure, we can see that the harmonic yield increases with increasing interaction pressure. Using the 1D model of Section 1.3.2, this trend indicates that we are operating in a sub-optimal interaction geometry, and increasing the pressure-length would improve our harmonic yield.

Fig. 3.17 shows a spectrum using optimized generation conditions (17 Torr interaction pressure, 1.85 mJ). Under these conditions, the highest resolvable harmonic is at 104 eV. From Eq. (1.27), we estimate $U_p = 25$ eV and $I_0 = 4.2 \times 10^{14}$ W/cm$^2$. On the other hand, if we calculate the peak intensity from the input pulse energy, we would expect $I_0 = 6 \times 10^{15}$ W/cm$^2$, nearly an order of magnitude higher that the HHG spectrum suggests. This suggest an inability to phase match the high energy photons.

Under these conditions, with a 400 mm focal length, we estimate the interaction energy to be $6 \times 10^{15}$ W/cm$^2$, and $U_p =$ From Eqs. (1.12) and (1.27), we calculate

can you predict the cutoff energy using the interaction intensity? for a cutoff energy of 100 eV, at 800 nm, in helium (assuming perfect phase matching), Up = 23.78 eV, and I = $4 \times 10^{14}$ W/cm$^2$. do we have perfect phase matching?

calculate the interaction intensity from the input beam. assuming a 16 mm diameter beam, 1.89 W of input power at 800nm, we should have an intensity of $1 \times 10^{16}$ W/cm$^2$, which is 25 times higher than the intensity predicted from the cutoff energy. if we had this

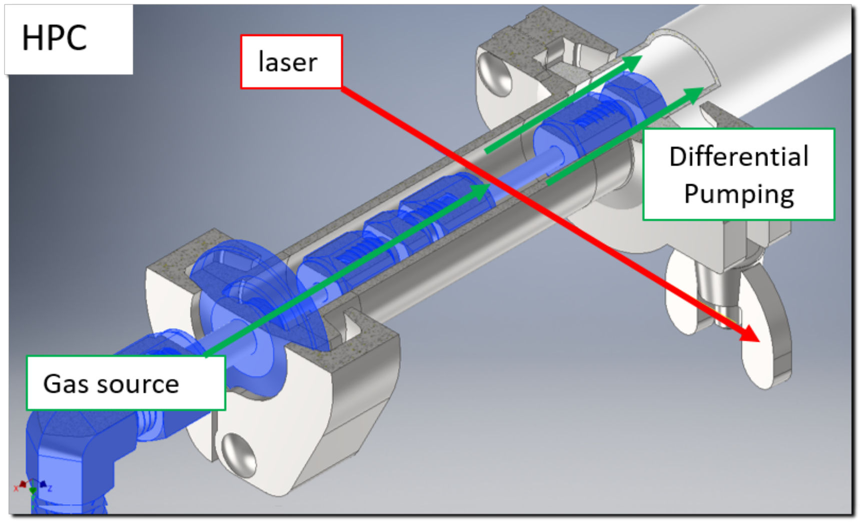


Figure 3.10: Cutaway view of the HPC interaction region. From bottom left to top right: welded gas feedthrough, concentric inner & outer pipes, connection to edge-welded bellows. The high pressure region is shaded blue. The green lines indicate the gas flow direction; the red line indicates the laser propagation direction.

intensity, our cutoff would be way higher ... something's not right. maybe we just can't phase match the higher photon energies?

advantages: increased interaction length - brighter! easy to align.

disadvantages: relative to the free expansion nozzle, you don't get any cooling.

### 3.2.5 High Pressure Cell

#### Design of HPC

The high pressure cell (HPC) was designed to be a drop-in upgrade to the previously available HHG gas sources. As such, we did not consider a semi-infinite gas cell design which would require disruptive chamber modifications. We also did not want to implement a waveguide solution, as its performance would be strongly effected by the coupling (and therefore the laser pointing) into the assembly [71, 72]. Finally, we wanted to avoid the complications of a pulsed solenoid valve [25], so the HPC was designed to be user-servicable with low-cost replacement parts. As such, it consists of standard Swagelok and KF fittings with minimal modifications and a custom bellows assembly. The only consumable part is the stainless steel pipe housing the interaction region, and it only needs to be replaced when the HPC is installed or the focusing condition is changed.

The design of the HPC is shown in Figs. 3.10 and 3.11. It features two concentric cylinders: a stainless steel inner pipe which serves as the interaction region and gas source, and

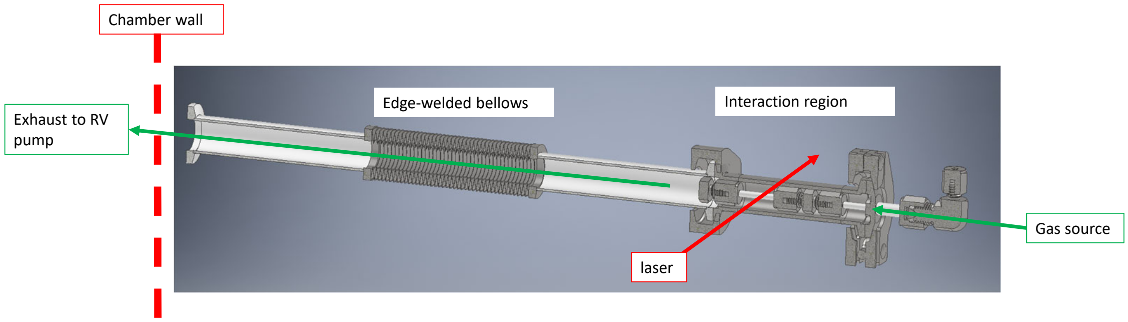


Figure 3.11: Cutaway view of the HPC assembly showing the flexible bellows connection and connection to the chamber wall.

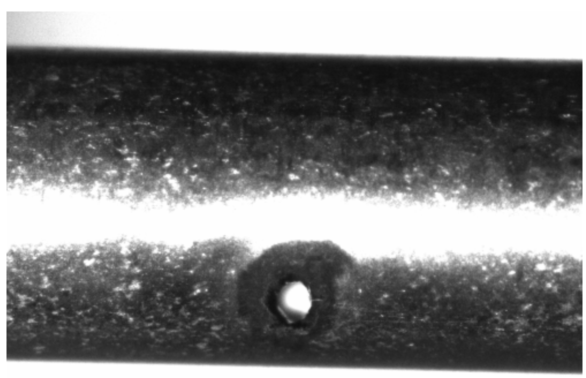

Figure 3.12: Photograph of the HPC's inner pipe showing the laser-drilled hole (bottom center of pipe). See text for details.

an outer shroud connected to an external rough pump which provides differential pumping. The inner pipe is connected to a gas line with continous flow. Laser-drilled diametrically opposed pinholes on the inner pipe wall allow for light propagation while minimizing gas flow to the outer shroud. A small portion of the gas within the outer shroud flows into the generation chamber via the machined holes, but most of the gas flows towards the exhaust and into a dedicated rough pump.

The relative positions of the inner pipe and the outer shroud are fixed by the KF hardware connections upon assembly. However, this positioning is not repeatable within the tolerances imposed by the laser transmission requirements. As a result, a new section of stainless steel pipe must be laser drilled every time the HPC is disassembled or removed from the generation chamber. The HPC assembly's position relative to the laser is adjustable via the same vacuum XYZ manipulator. A set of flexible bellows, visible in Fig. 3.11, allows for this movement while maintaining a vacuum-tight connection between the outer shroud and the chamber wall. A Baratron pressure gauge monitors the pressure inside the bellows and the outer shroud during operation.[9] The flexible bellows has enough slack to allow the HPC to move below the optical axis, allowing the beam to pass over the top of the outer shroud. This is useful when aligning downstream optics.

The laser passes through the HPC assembly perpendicular to its symmetry axis; therefore the gas-laser interaction length is approximately equal to the diameter of the inner pipe. The outer shroud has two diametrically opposed machined 600 $\mu$m holes for the laser to pass through the assembly. During installation, the user aligns the two apertures in the outer shroud to the laser and fixes its position. Next, the inner pipe is installed and the unattentuated laser drills through the inner pipe walls. Therefore, the four apertures are automatically colinear and aligned to the laser propagation axis.

Fig. 3.12 shows a photograph of the laser-drilled holes, taken with a 0.5x telecentric lens (Edmund Optics part number 62-911). Laser drift & misalignment, as well as daily harmonic optimization procedures over the course of several months have opened up these holes from their original diameter of approximately 100 $\mu$m to a final diameter of 430 $\mu$m.

### Gas Flow in HPC

The geometry of the HPC assembly allows the user to use much higher interaction pressures than other continuous gas sources in the DiMauro lab. Here, we will model the gas flow through the HPC to see why this is the case. Fig. 3.13 shows the gas flow and relevant geometry. With the HPC cell installed, there are three distinct pressure regions: the high pressure inner pipe, the medium pressure outer shroud, and the low pressure generation chamber. Gas flows from the high pressure region through the laser drilled apertures into

[9]Note: the bellows cannot withstand an internal pressure differential greater than 120 Torr. See Section A.5 before operating this system.

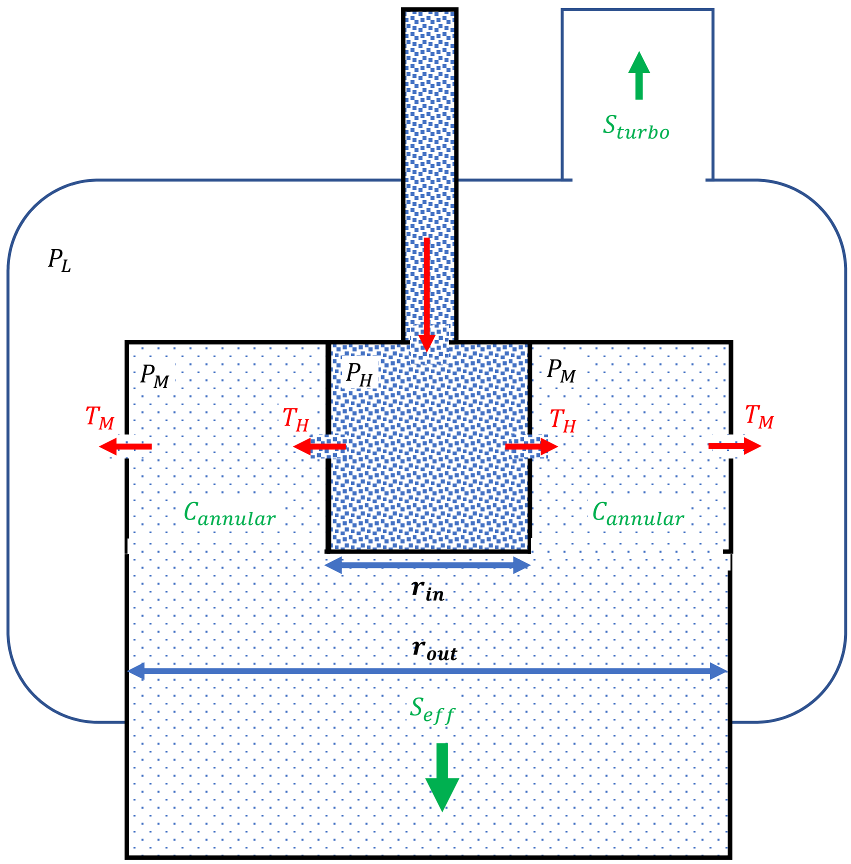


Figure 3.13: Schematic used to calculate the pressures inside the HPC and generation chamber.

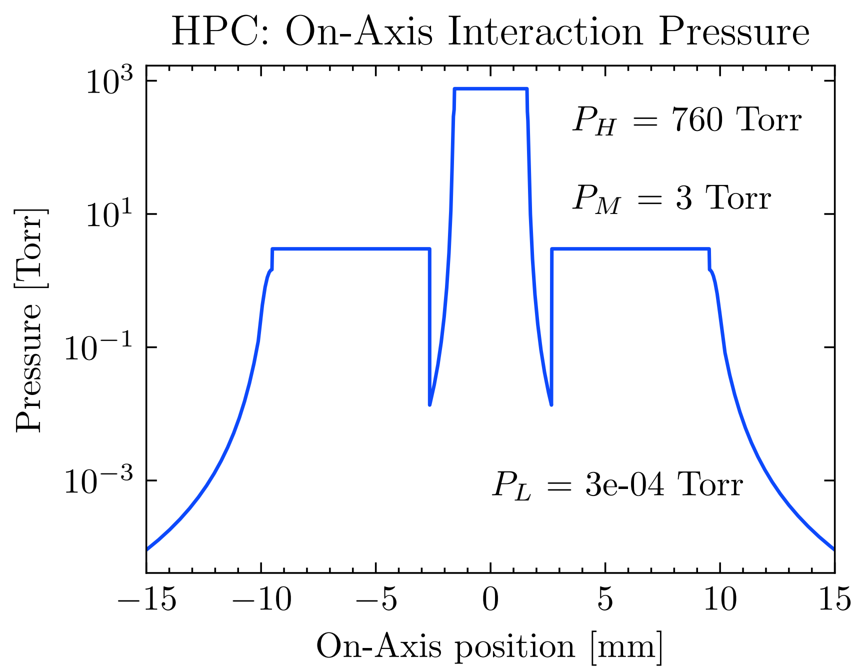


Figure 3.14: Calculated on-axis pressure in the HPC for argon with $P_H = 760$ Torr, $P_M = 3$ Torr and $P_L = 3 \times 10^{-4}$ Torr.

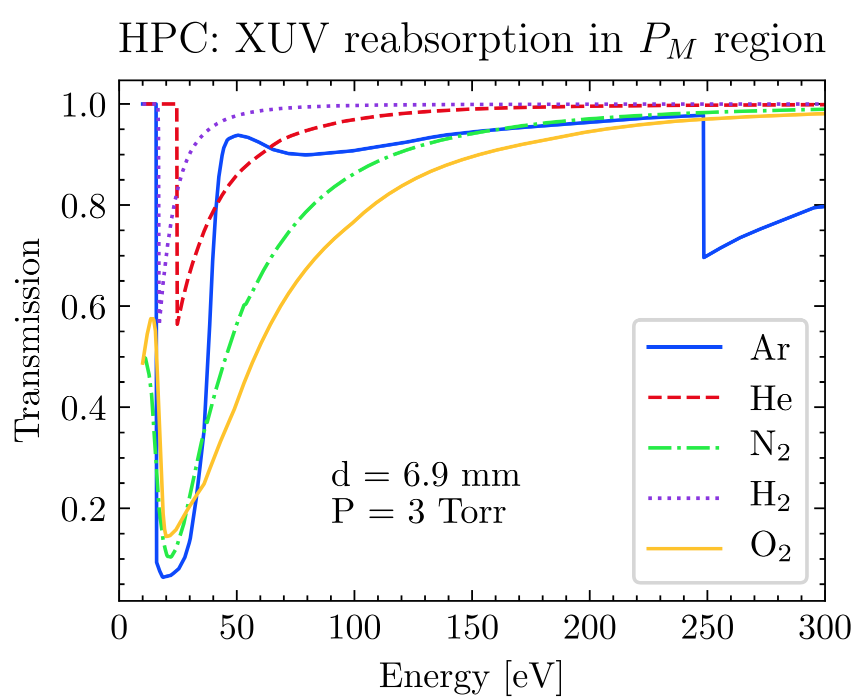


Figure 3.15: XUV reabsorption in the $P_M$ region for different generating media.

the medium pressure region. In the medium pressure region, gas flows through the machined apertures on the outer shroud's walls into the vacuum chamber, or down the bellows assembly to the rough pump.

We define the relevant variables in Fig. 3.13. The dark blue region represents the high pressure region ($P_H$), the light blue region represents the medium pressure region ($P_M$), and the low pressure region is represented by the white region ($P_L$). Red arrows and text indicate gas sources, green arrows and text indicate flow towards the vacuum pumps; blue arrows and text indicate physical dimensions. $P_H$, $P_M$, and $P_L$ are the pressures of the inner pipe, outer shroud, and generation chamber, respectively; $S_{turbo}$, $S_{eff}$ and $C_{annular}$ are the turbo pumping speed, effective rough pumping speed and annular conductance, respectively; $T_H$ ($T_M$) is the gas throughput from the high (medium) pressure region into the medium (low) pressure region.

We assume that the high pressure region is an infinite gas reservoir held at pressure $P_H$ set by the regulator on the gas cylinder. The medium pressure region has a net gas throughput of $Q_M = 2(T_H - T_M)$ and an effective pumping speed $S_{eff}$. The low pressure region has a gas throughput of $2T_M$ and a pumping speed of $S_{turbo}$. The pressure in each region is simply $P = Q/S$. Owing to the large pressure differentials between adjacent regions, the gas throughput of the apertures is supersonic and is proportional to the area of the aperture and the backing pressure, following Eq. (3.6):

$$T_H = cP_H a_H^2, \tag{3.14}$$

where $a_H$ is the diameter of the laser drilled aperture. The supersonic expansion gives rise to a plume structure with an on-axis spatial extent given by the Mach disk location, $x_M/a_H = 0.67\sqrt{P_H/P_M}$ [58]. At on-axis distances larger than $x_M$, we can ignore the supersonic plume structure and consider only the background pressure $P_M$. For $P_H = 760$ Torr, $P_M = 3$ Torr and $a_H = 100$ $\mu$m, $x_M = 10.6a_H = 1.06$ mm. Since the distance between the laser drilled aperture and the outer shroud's machined hole (6.2825 mm) is much greater than $x_M$, so we can ignore the supersonic plume structure when considering the gas flow from the medium pressure region to the low pressure region. As a result, $T_M$ has the same form as $T_H$:

$$T_M = cP_M a_M^2 \tag{3.15}$$

We can calculate the Mach disk location for the machined apertures using measured pressures in each region: for $P_M = 3$ Torr, $P_L = 3 \times 10^{-4}$ Torr, and $a_M = 600$ $\mu$m, we have $x_M = 67a_M = 40.2$ mm. This distance is much smaller than the distance between the HPC and the next vacuum chamber (25 cm), so we can ignore the effect of the HPC's supersonic plumes on the rest of the beamline.

The medium pressure region is pumped by a small RV pump with pumping speed $S_{RV}$.

This pumping speed is reduced by the geometry of the pipes between the shroud's apertures and the mouth of the pump. First, the inner pipe and outer shroud form an annual pipe; secondly, the bellows and the several feet of soft PVC tubing further reduce the pumping speed. Given the relatively high pressures in the medium pressure region (a few Torr), the mean free path of the gas is much smaller than the characteristic length scale of the system and we are in the viscous regime. Therefore, we can compute the effective pumping speed $S_{eff}$ of the medium pressure region by successive application of the standard conductance equations [33, 37]. First, the conductance of the annual region (liter/s) is:

$$C_{annular} = \frac{1}{1000} \frac{\pi}{8\eta} \frac{P_1 + P_2}{2L} \left( r_{out}^4 - r_{in}^4 - \frac{(r_{out}^2 - r_{in}^2)^2}{\log\left[r_{out}/r_{in}\right]} \right) \tag{3.16}$$

where $r_{out}$ and $r_{in}$ are the outer and inner radii of the annular region, $\eta$ is the viscocity, $L$ is the length of the annular region, and the pressures on either side of the annular region are $P_1$ and $P_2$. The conductance of the bellows assembly, the chamber feedthrough and the several feet of PVC tubing is treated using standard formalism

$$C_{KF} = 179 \frac{d^4}{L} \frac{P_1 + P2}{2} \tag{3.17}$$

where $d$ is the diameter of the pipe, $L$ is the length, and $(P_1 + P_2)/2$ is the average pressure along the pipe. With a known conductance $C$ and pumping speed $S$, we can calculate the effective pump speed $S_{eff}$ in the usual way:

$$\frac{1}{S_{eff}} = \frac{1}{C} + \frac{1}{S} \tag{3.18}$$

We now have a framework in which to calculate the pressure profile of the HPC. To pump the HPC, we use a small 5 L/s rough pump connected to the chamber via a 150 cm long KF25 soft PVC tube, which delivers a pumping speed of 4.97 L/s to the chamber wall. The bellows assembly (KF16 diameter, 30 cm long) reduces the pumping speed to 4.69 L/s at the beginning of the annular section. The annular section of the HPC assembly is very restrictive ($r_{out} = 0.7875$ cm, $r_{in} = 0.6415$ cm, $L = 8.661$ cm), with a conductance of $C_{annular} = 1.64$ L/s and an effective pumping speed for the medium pressure region of $S_{eff} = 1.22$ L/s. If we assume a laser drilled aperture diameter of $a_H = 193$ $\mu$m and a backing pressure of $P_H = 760$ Torr, and a turbo pump speed of $S_{turbo} = 1000$ Liter/s, then we will have $P_M = 3.12$ Torr and $P_L = 3.16 \times 10^{-4}$ Torr.

Fig. 3.14 shows the on-axis pressure for the HPC. We can see that the HPC concentrates the gas within the inner pipe (760 Torr) where most of the XUV light will be produced. Due to the lower pressures and the finite Rayleigh range, harmonics will not be produced in the medium pressure region ($P_M = 3$ Torr). However, the extended interaction length (6.9 mm) will lead to significant transmission losses at lower photon energies (20 - 50 eV),

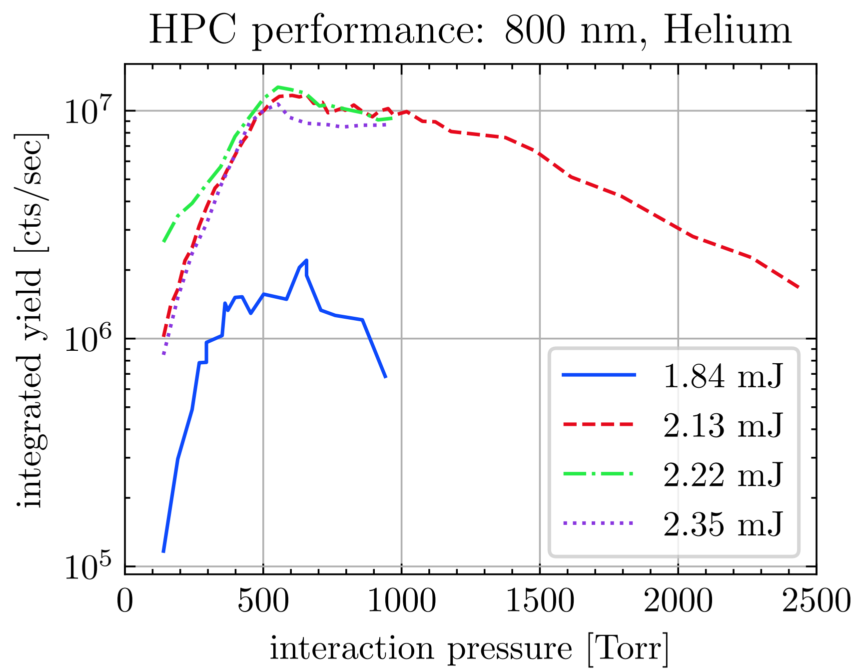


Figure 3.16: Total harmonic yield as function of interaction pressure in the HPC.

depending on the generating media. Fig. 3.15 shows this effect. Even with these absorption losses, the improved pressure-length product of the HPC makes it a bright XUV source in this energy range, as will be shown below.

#### HHG in the HPC

The pressure scaling of the HPC is shown in Fig. 3.16. Unlike the LPC, we can see a maximum in the harmonic yield with respect to pressure. Although the y-axis scale for Figs. 3.9 and 3.16 is arbitrary, they are in the same units and therefore are comparable. We can see that the total harmonic yield of the HPC exceeds that of the LPC by about 2 orders of magnitude.

HHG yields at higher pressures are lower than otherwise expected, most likely due to increased XUV absorption in the PM region, and perhaps non-ideal IR propagation before the focus. ie, the increased pressure messes up the pulse, or the XUV is reabsorbed after it is made.

A comparison between the LPC and the HPC is shown in Fig. 3.17.

The performance increase of the HPC comes from an increased pressure-length product, which is primarily due to the inner pipe's geometry and the differential pumping afforded by the outer shroud. We have tested the HPC with backing pressures up to 150 psig, which was previously only possible in our lab using expensive and unreliable pulsed valves.

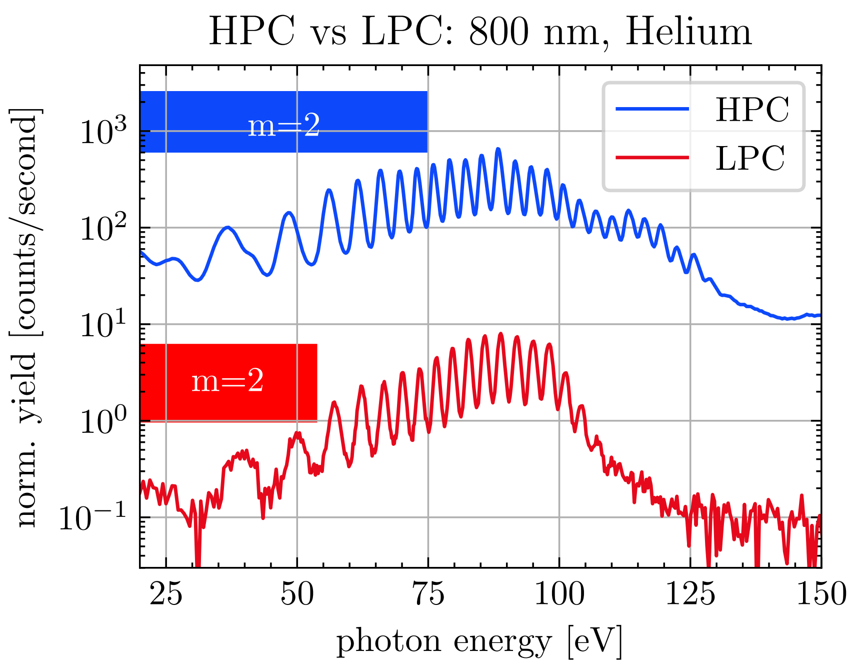


Figure 3.17: Comparison of the LPC and the HPC in helium at 800 nm. Generation conditions for each were optimized (LPC: 17 Torr interaction pressure, 1.85 mJ; HPC: 650 Torr, 2.13 mJ) in helium at 800 nm. The HPC extends the cutoff from 104 eV to 132 eV and increases the XUV brightness by roughly 100x across the spectrum. Note that harmonics with energies less than half the cutoff are contaminated by $2^{\text{nd}}$ order diffraction from the XUV spectrometer's grating.


Figure 3.18: Amsterdam Piezo Valve. The nozzle is located at the center of the front face (flat side).

- limited pump speed → differential pumping is required

harmonic yield results

advantages: much brighter due to pressure-length product. future application: can operate in low-pressure mode and reduce downstream generation gas contamination of target chamber.

disadvantages: difficult to align and initially install (once it's installed, alignment is easy). messed up mode. HHG instability at higher pressures.

pictures of the HPC.

### 3.2.6 Pulsed Amsterdam Piezovalve

We briefly had access to a commercial pulsed valve (Amsterdam Piezo Valve by MassSpecpecD BV)[10]. Operating a valve in pulsed mode greatly reduces the gas throughput into the vacuum chamber, as the throughput scales approximately with the duty cycle of the valve. Typical valve opening times are on the order of tens of microseconds [39, 40, 57]. When operated at 1 kHz to match our laser repetition rate, we achieve about two orders of magnitude reduction in chamber operating pressure, compared to a DC gas source of similar dimensions. The Amseterdam piezo valve utilizes an o-ring mounted to a

[10]Special thanks to Andrew Piper for letting us borrow his equipment.

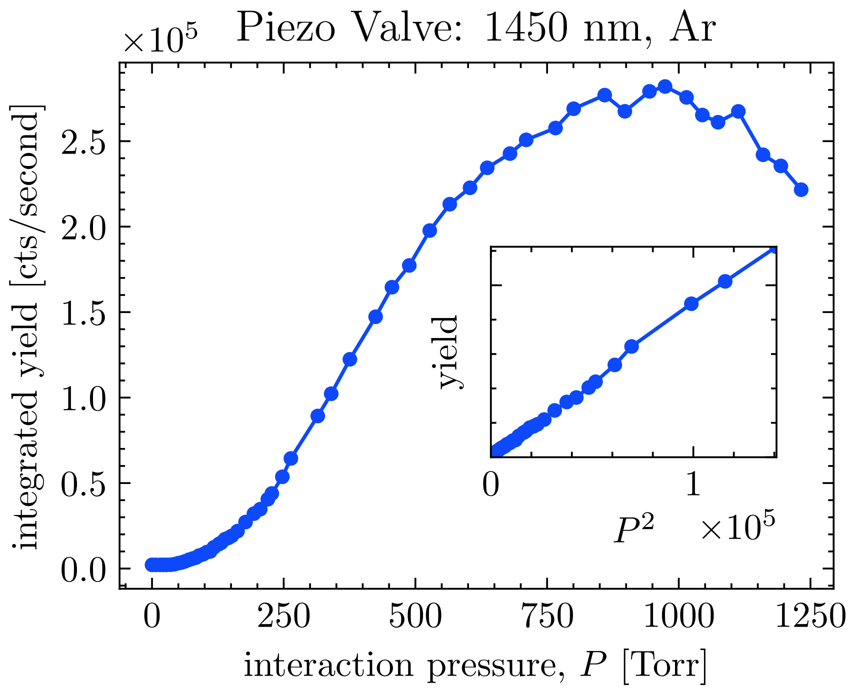


Figure 3.19: Integrated harmonic yield from the piezo valve as a function of interaction pressure. The inset shows excellent quadratic behavior with respect to interaction pressure. Assumed on-axis distance is $x = 250$ $\mu$m.

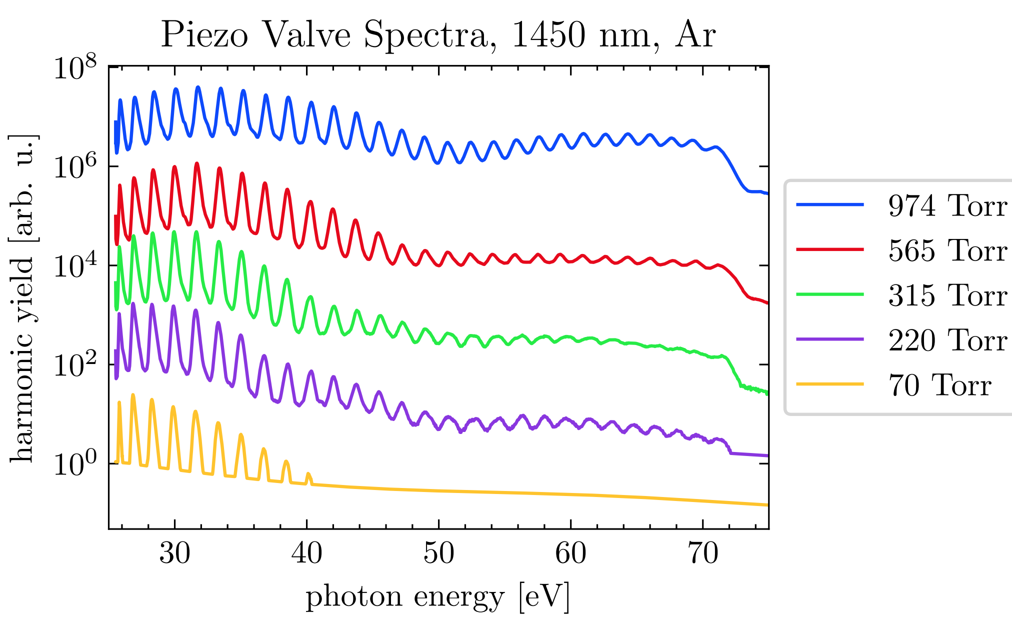


Figure 3.20: piezo valve spectra vs pressure. Spectra are vertically offset for visual clarity. Assumed on-axis distance is $x = 250$ $\mu$m.

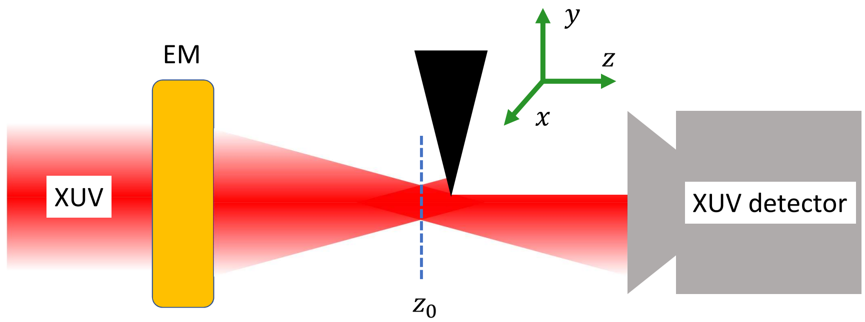


Figure 3.21: Schematic of XUV knife edge measurement. EM: ellipsoidal mirror, $z_0$: XUV focal plane.

cantilever piezoelectric flapper to briefly open an internal gas inlet port. Our model has a $d = 500$ $\mu$m diameter straight-channel nozzle and a backing pressure range of 0 - 15 bar.

For these experiments, we used a 75 $\mu$s opening time and an operating voltage of 150 V. The on-axis distance from the aperture to the optical axis is estimated to be $x = 250$ $\mu$m.

We use Eqs. (3.2a), (3.2b) and (3.3b) to calculate the on-axis jet parameters: the Mach number is $M = 1.45$, the interaction density is $\rho/\rho_0 = 0.45$ and the interaction pressure is $P/P_0 = 0.27$.

delay introduced by Quantum Composer.

thanks to andrew piper for letting us use his piezovalve.

the piezo valve is shown in Fig. 3.18.

pressure scaling of total harmonic yield is shown in Fig. 3.19.

evolution of spectra / shape of spectra changes with pressure, as shown in Fig. 3.20. this is due to the photon energy dependence of phase matching conditions. this is typical for all gas sources.

for more detail and characterization of the piezo valve, see andrew piper's dissertation [69].

## 3.3 Characterization of XUV Source

### 3.3.1 Knife Edge Measurements

We characterize the XUV focus in the target chamber by performing knife edge measurements at different $k$-positions, as depicted in Fig. 3.21. We use the interior angled edge of the Si frame on a broken sample heterostructure as a knife edge (see Fig. 4.4). This frame makes an excellent knife edge as it has a very well-defined geometry and fits in the sample

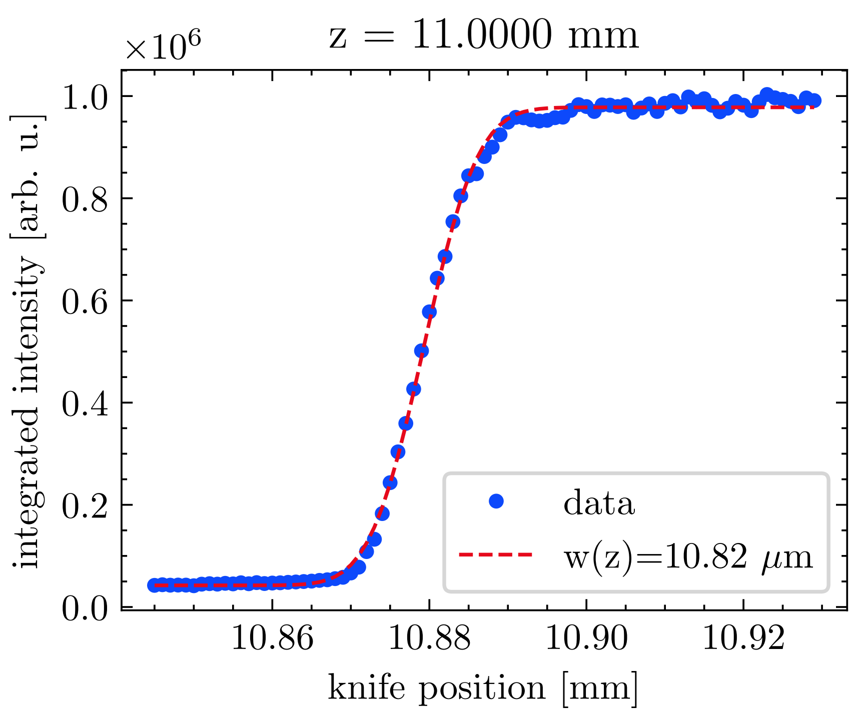


Figure 3.22: A typical XUV knife edge measurement near the focal plane. The sample motor position is $k = 11.0000$ mm. A fit to equation Eq. (3.21) yields a beam waist of 10.82 $\mu$m at this position.

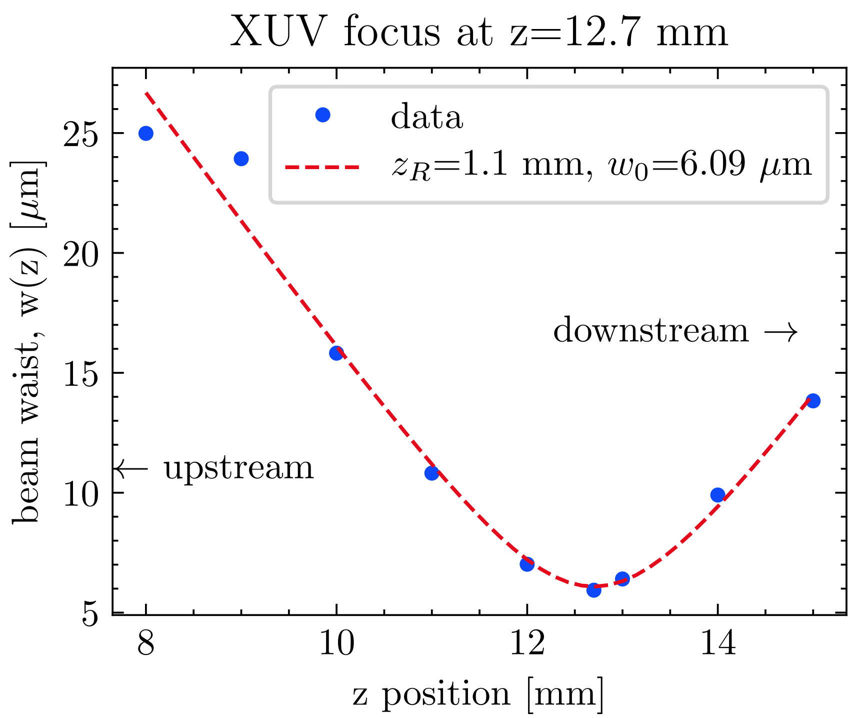


Figure 3.23: Evolution of XUV beam waist as a function of propagation direction, $z$. The Rayleigh range $z_R$ and beam waist $w_0$ are extracted from the fit to Eq. (3.20).

holder. Recalling Gaussian optics, the assumed profile of the XUV beam is:

$$I(x, y, z) = I_0 \left(\frac{w_0}{w(z)}\right)^2 \exp\left(-2\frac{(x - x_0)^2 + (y - y_0)^2}{w(z)^2}\right), \tag{3.19}$$

using the coordinate system defined in Fig. 3.21. The XUV focus is at position $(x_0, y_0, z_0)$. The beam waist $w(z)$ will evolve as:

$$w(z) = w_0\sqrt{1 + \left(\frac{z - z_0}{z_R}\right)^2}, \tag{3.20}$$

where $z_R$ is the Rayleigh range. If we use the knife edge to block the transmission as depicted in Fig. 3.21, then the transmitted power will be:

$$P(x, z) = P_0 + \frac{P_{max}}{2}\left(1 - \text{erf}\left(\frac{\sqrt{2}(x - x_0)}{w(z)}\right)\right), \tag{3.21}$$

where $x$ is the insertion of the knife in the beam, $z$ represents the location of the knife plane in the propagation direction, and erf is the error function.

A typical knife edge measurement is shown Fig. 3.22. In this measurement, the knife edge is translated across the XUV spot in 1 $\mu$m steps until the XUV light is completely blocked. A 2D spectrum is saved at each knife edge position. Each image is background subtracted, normalized and summed (integrating over all divergences and wavelengths), which yields the XUV flux as a function of knife position. The resulting curve is fit to Eq. (3.21) and the beam waist $w(z)$ is extracted for this $z$-position.

The knife edge measurement is repeated at different $z$-positions until enough data has been acquired to determine the focal plane. The evolution of the XUV beam waist is shown in Fig. 3.23. In this figure, the beam waist has been fit to Eq. (3.20) to determine the focal plane $z_0$, the Rayleigh range $z_R$ and the beam waist $w_0$. In both figures, a reasonably good fit is obtained, indicating that the XUV light has a Gaussian spatial profile near the focus.

### 3.3.2 harmonic yield stability

### 3.3.3 XUV spectra optimized for various HHG conditions

### 3.3.4 Measured Transmission of Metallic Filters

### 3.3.5 Ground State Measurements of Condensed Matter Samples

## 3.4 characterization of interferometric stability

## 3.5 MCP response

scaling of yield and noise with respect to MCP voltage

# Chapter 4
# ATAS Experiments in Germanium

## 4.1 Introduction

## 4.2 Experimental Considerations

### 4.2.1 sample requirements

There are several sample requirements for a successful condensed matter transient absorption experiment. First and foremost, the sample needs to have an absorption edge within the bandwidth of the XUV source. Second, the material must be the correct thickness for a transmission measurement, given the capabilities of the XUV light source and detector. If the material is too thick, the ground state will absorb most of the XUV flux and the recorded spectrum will be too close to the noise floor of the apparatus. If it is too thin, the laser-induced change of the ground state (on the order of $1-10\%$) will be lost in the noise. As a general guideline, a sample that absorbs 50% at the spectral feature of interest provides a good compromise between these conflicting requirements. Fig. 4.1 shows the expected transmission of several materials, calculated from the atomic scattering factors [32]. We can see that a typical sample will be on the order of 10 - 200 nm thick, depending on the material.

Another upper bound for sample thickness comes from material dispersion. In any material, the XUV light ($n_{\mathrm{IR}} \sim 1$) will outpace the IR light ($n_{\mathrm{IR}} > 1$). This effect can be significant even for ultrathin films. In order to keep the phase slippage between the XUV and IR light below half an IR period, the sample thickness $L$ must obey the following relationship:

$$L \leq \frac{1}{2}\frac{\lambda_{\mathrm{IR}}}{n_{\mathrm{IR}} - n_{\mathrm{XUV}}} \tag{4.1}$$

For germanium excited with $\lambda_{\mathrm{IR}} = 1430$ nm and probed with 30 eV XUV at the $M_{4,5}$ edge, $n_{\mathrm{IR}} = 4.2481$ [63] and $n_{\mathrm{XUV}} = 0.992536$ [32], which gives a maximum thickness of 220 nm.

Next, the sample needs to be excitable using laser sources present in our lab (i.e., ultrafast pulses with wavelengths between 800 nm and a couple of microns). To minimize

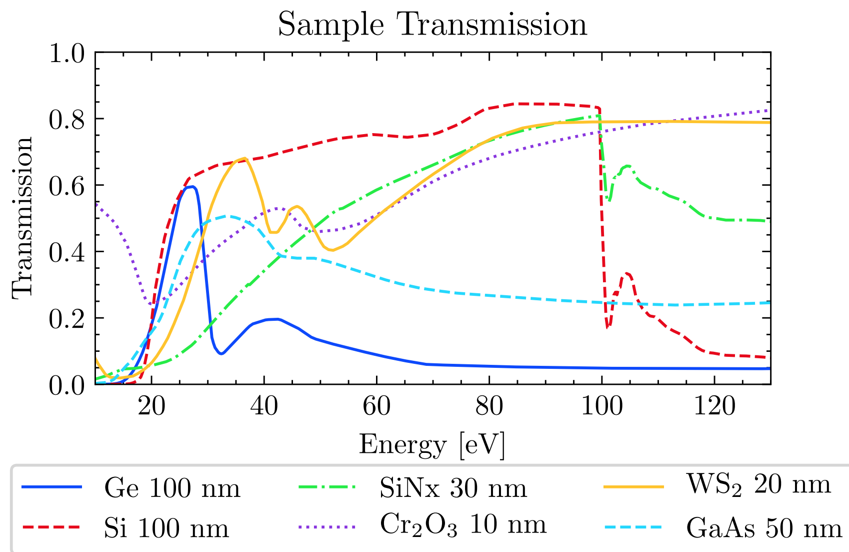


Figure 4.1: Calculated XUV transmission of various materials. Data from [32].

the slow build up of heat (on the order of seconds) and laser-induced damage, the sample needs to be rastered through the laser focus as the experiment is performed. This rastering method necessitates both a large clear aperture ($\sim$ 1 mm$^2$ - 1 cm$^2$) and good sample uniformity. Samples that meet the above thickness and clear aperture requirements are extremely delicate, with thicknesses between 5,000 and 100,000 times smaller than their freestanding lateral dimensions. As such, one should expect most samples to break before, during and after measurements, so a successful experiment will have a materials pipeline that is capable of producing multiple, consistent samples in a short time frame.

### 4.2.2 The Supporting Nitride Membrane

While most materials have an absorption edge within the range 25 - 150 eV, there are very few commercially available pre-fabricated materials with both the requistite large clear aperture and thickness. Note that either characteristic is relatively easy to achieve individually, but their combination presents unique materials challenges. We considered three synthesis methods to produce this quasi-2D sample:

1. sample growth on a traditional substrate, followed by chemical back-etching or milling of the substrate until sub-micron thickness of the heterostructure is achieved;

2. sample growth on a traditional substrate, followed by mechanical transfer onto a membrane;

3. sample growth on a membrane.

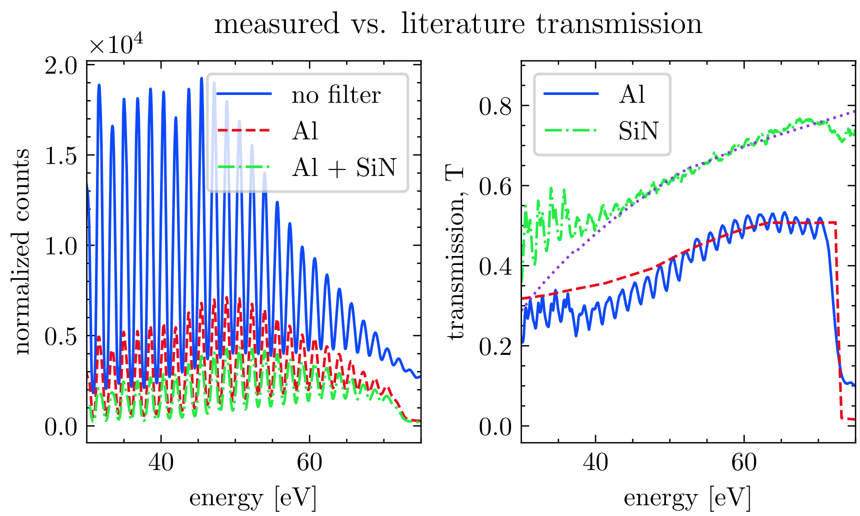


Figure 4.2: XUV transmission measurements of Al metallic filter and silicon nitride membrane. Left panel: normalized XUV counts for i) unfiltered HHG signal, ii) HHG going through a 200 nm Al filter and iii) HHG going through a 200 nm Al filter and 30 nm of silicon nitride. Counts are scaled by the Jacobian. Right panel: transmission curves obtained from the left panel's data. Also shown are literature values for 20 nm of silicon nitride and 200 nm of Al with two 4 nm oxide layers [32]. Multilayer interference is not taken into account. Oscillations in measured transmission are numerical artifacts which will be discussed in the text.

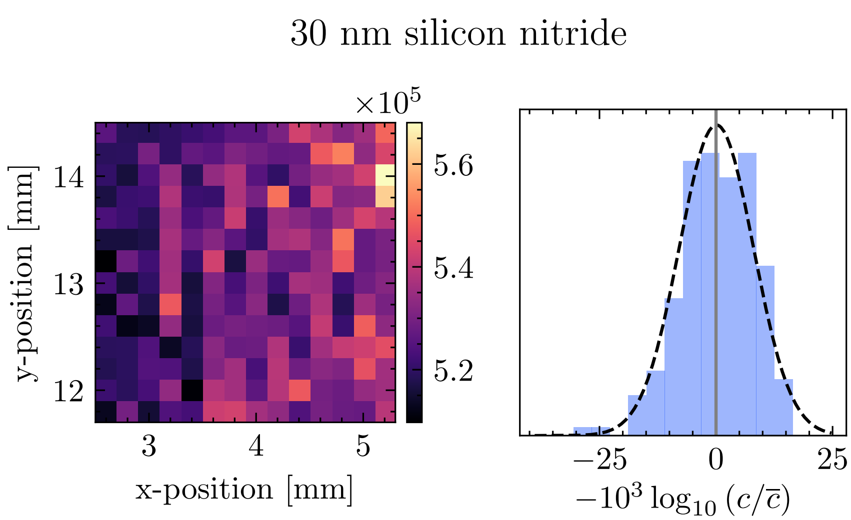


Figure 4.3: XUV transmission map of 30 nm silicone nitride freestanding membrane. Left panel: integrated XUV counts in the range 30 – 34 eV. Sample holder motor positions are indicated by x- and y-positions. Right panel: histrogram of logarithmic deviation of counts from the average. Dashed line shows a normal distribution.

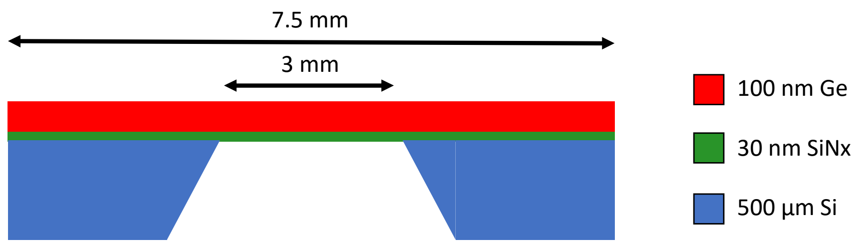


Figure 4.4: Cartoon showing the cross section of the free standing sample heterostructure. A 500 $\mu$m thick Si frame supports a freestanding 30 nm low stress silicon nitride membrane (Norcada QX7300X), upon which 100 nm of germanium has been deposited. The Si frame has a 3x3 mm$^2$ square clear aperture and a 7.5x7.5 mm$^2$ square external dimension. The taper of the Si frame thickness along the perimeter of the clear aperture forms a knife edge. In an ATAS experiment, the XUV and IR pulses propagate from the top to bottom of the figure.

Sample quality and composition is heavily impacted by local growth conditions such as substrate temperature, deposition rate, substrate crystal cut, substrate-sample lattice mismatch, etc. Many of these characteristics are changed when growing on a substrate of a different cut, or by replacing a substrate with a membrane. In general, one should not expect success when applying a substrate-optimized growth recipe to a freestanding membrane. Therefore, methods 1 and 2 will yield the highest quality samples, as they leverage already-developed sample recipes. However, both methods require a technically difficult second step that is prone to failure.

Selective chemical etching recipes exist for certain compounds, but they usually require an additional chemically intert layer in the heterostructure to protect the sample. Adding this layer will come at the expense of the total XUV flux transmitted by the heterostructure. Additionally, the chemical etching rates are highly dependent on local chemistry, fluid convection and temperature [17], which ultimately means that the amount of material removed is uncontrollable and unrepeatable within our requirements (499.9 $\mu$m $\pm$ 10 nm removed from a 500 $\mu$m substrate). For these reasons, we decided to not pursue a chemical etch recipe. Ion or electron milling is more controllable, but too expensive to implement on a large scale. The above reasons preclude the use of Method 1.

Mechanical transfer of thin samples is a tried and true method, but it usually results in flakes with lateral dimensions on the order of 100 $\mu$m. Repeated transfer of many flakes is possible, but there little control over their exact positioning on the membrane. This results in a random distribution of flakes; the flakes are sometimes folded or overlapping one another. These mishaps increase the effective optical density of the sample, changing the IR and XUV absorption properties significantly.

An XUV spatial measurement needs to be taken prior to any ATAS experiment, but a non-uniform distribution of flakes on a membrane would require a much higher resolution map. This is because the flakes are on the order of the XUV and IR focii, so it is critical that the raster points in Fig. 4.5 correspond to the center of each flake to avoid edge diffraction and to minimize the effects of slow laser pointing drift. For a uniform film, a map can be taken using 200-250 $\mu$m step sizes, as the most important feature is the border of the clear aperture. On the other hand, each flake would have to be sampled $\sim$5 times in each direction to find its center. As a conservative estimate, a membrane covered with $100 \times 100\ \mu\text{m}^2$ flakes would require a step size of 20 $\mu$m, which increases the number of raster points by a factor of $10^2 = 100$. Considering that a $3 \times 3\ \text{mm}^2$ clear aperture sampled with 200 $\mu$m steps takes $\sim$45 minutes to map, a random distribution of flakes would take a prohibitively long time to map out.

With the first two methods ruled out, we turn to the third method of growing directly on a freestanding membrane. Although it will result in a lower quality sample, it does not have the same technical hurdles of the previous two methods. However, the large clear area makes the heterostructure extremely fragile. We initially attempted to circumvent this problem by using an array of smaller clear apertures.

As shown in Fig. 4.5, most of the sample's area isn't directly used by the laser - it exists as a buffer between the grid of sample points. An alternative to a single clear aperture is an array of micro-apertures, each with a diameter on the order of the IR spot size. The micro-apertures exist within a mechanically robust substrate and a thin membrane lies on top of the structure. This configuration significantly eases the material strength requirements by reducing the size of the unsupported area from cm-scale to sub-mm-scale. The regular grid of apertures avoids the difficulties of a randomly distributed sample, easing the XUV mapping step size requirements. Fortunately, these arrays are commercially available from Silson, Norcada (silicon nitride membranes) and US Applied Diamond (diamond membranes) but we encountered technical difficulties in their implementation. Because the aperture size is on the order of the size of the IR focal spot, there is very little room for positioning error, and our motors were insufficiently precise for this application. Further, these arrays are typically only available in at most a $3 \times 3$ array, which provides an insufficient number of raster points for an ATAS experiment.

With these limitations in mind, we decided to use large aperture x-ray windows from Norcada. These windows consist of a mechanically robust Si frame substrate with a square clear aperture cut through the center. The structure is fabricated so that a thin membrane covers the clear aperture. A schematic of the cross section is shown in Fig. 4.4.

Norcada offers these structures with either a silicon (polycrystalline or single-crystal) or a silicon nitride membrane. An ideal membrane is transparent to both XUV and IR wavelengths with a high damage threshold. Referring to Fig. 4.1, 100 nm of Si provides a relatively flat transmission curve from 25 to 100 eV. In constrast, 30 nm of silicon nitride has

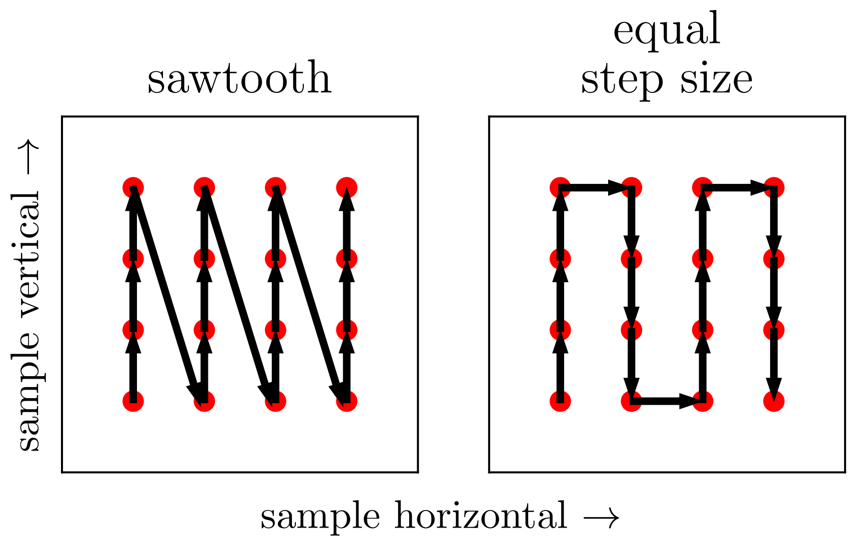


Figure 4.5: Schematic of competing raster methods, shown in the sample's reference frame. The clear aperture of the sample is represented by the interior of the black square. The laser propagation direction is out of the page. The laser focal spots are shown as red circles, and the movement of the sample holder relative to the laser focus is indicated by arrows. A 200 $\mu$m border exists between the raster array and the perimeter of the sample's clear aperture. This diagram is to scale for a $1 \times 1$ mm$^2$ clear aperture sample, a 60 $\mu$m diameter IR focal spot and a 200 $\mu$m step size.

poor, but featureless, transmission at lower energies. Both materials transmit light below their bandgaps (5 eV for SiN and 1.14 eV for Si). Finally, silicon nitride's higher bandgap results in a significantly higher laser damage threshold [4, 29, 45]. Taking all these factors into account, we decided to use 30 nm silicon nitride membranes for germanium transient absorption experiments. The measured transmission of a typical membrane is shown in Fig. 4.2.

### 4.2.3 rastering of sample through focus to avoid heating, charge build-up

### 4.2.4 XUV maps of samples

### 4.2.5 IR propagation in thin films (TMM starting with LightPipes output)

### 4.2.6 orbital-resolved excitation probability vs wavelength (band structure calculations)

Fig. 4.9 shows the spectral content of the TOPAS signal at $\lambda =$ nm. If we make the assumption that the spectral lineshape of the TOPAS output is invariant under wavelength

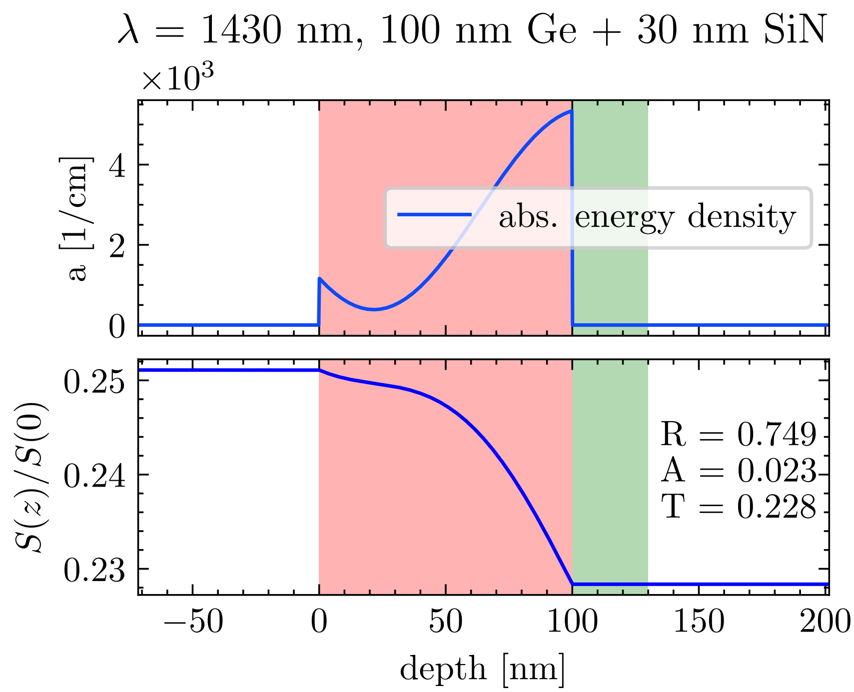


(a)

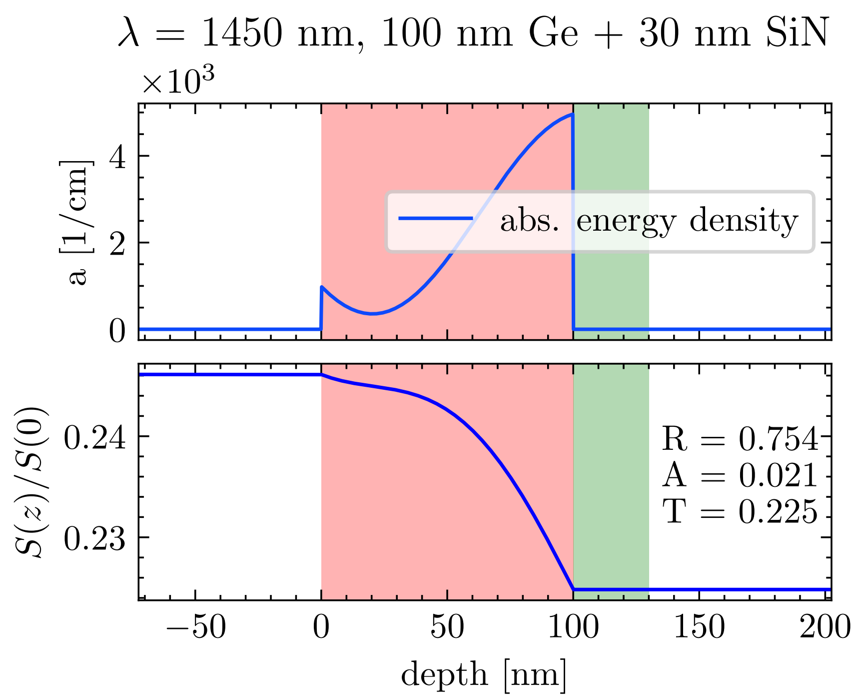


(b)

Figure 4.6: Thin film calculations for the sample heterostructure. The red region represents germanium; green is silicon nitride. Top panel shows the absorbed energy density per unit input power. Bottom panel shows the local intensity $S(z) \equiv \mathbf{S}(z) \cdot \hat{z}$, normalized by the input intensity $S(0) \equiv \mathbf{S}(0) \cdot \hat{z}$. Calculations performed using the TMM package for Python [8, 9].

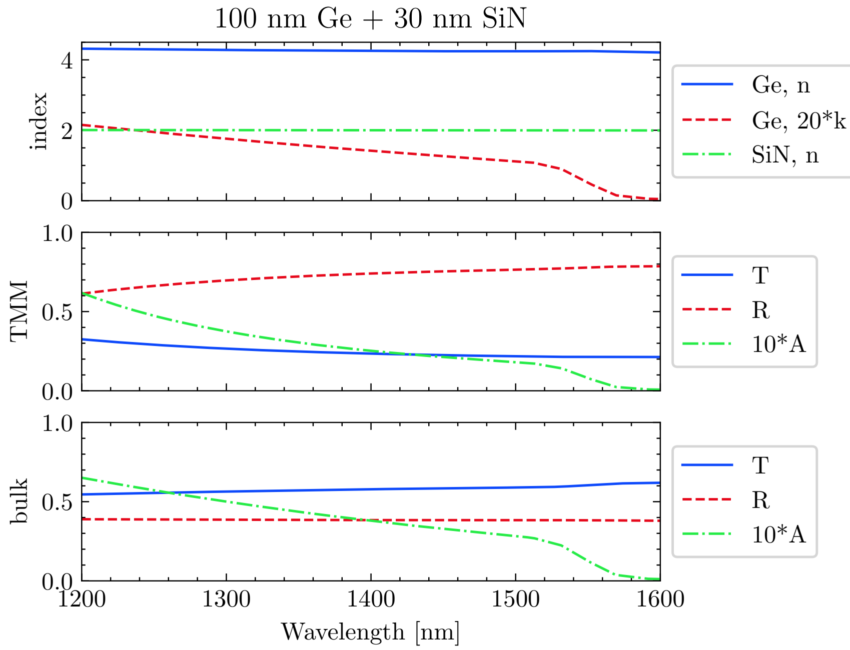


Figure 4.7: TMM calculation showing the spectral response of the sample heterostructure.

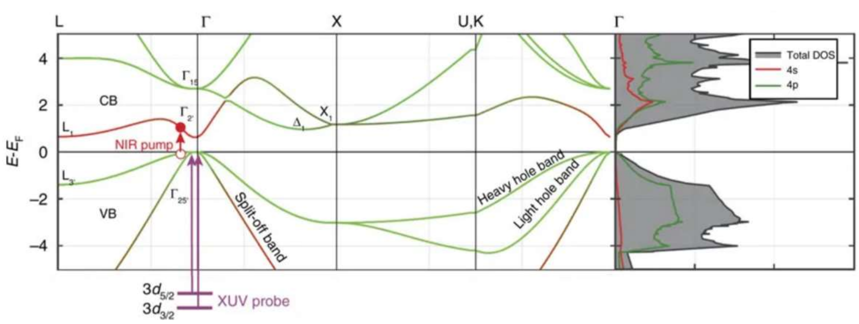


Figure 4.8: Band structure and orbital character of germanium. Purple arrows indicate XUV-induced transitions from the $3d$ core levels to the valence bands. Red arrow indicates IR-induced transition across the direct band gap. Figure adapted from [94].

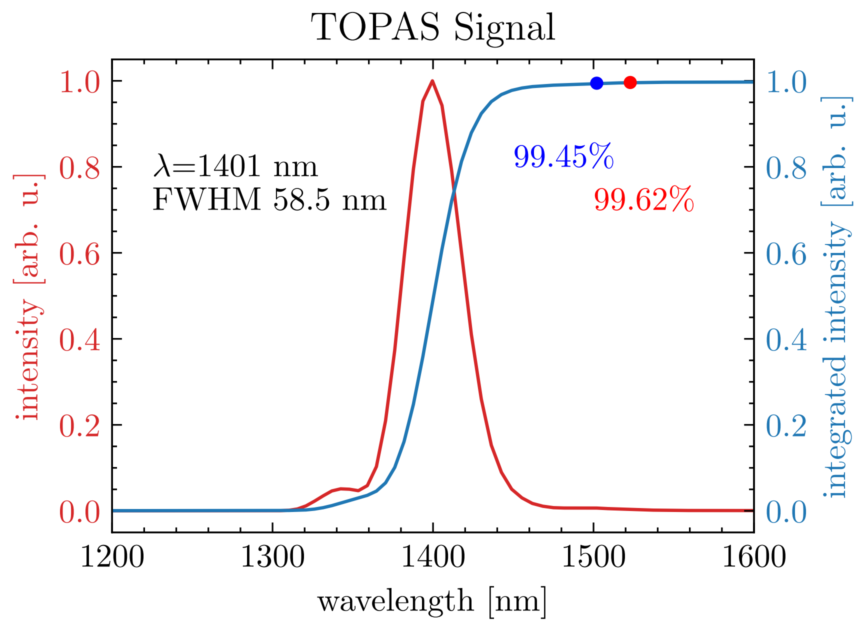


Figure 4.9: TOPAS spectral content at $\lambda = 1400$ nm.

shifts, then we can use this spectrum to estimate the spectral intensity at the bandgap when the TOPAS is set to 1430 or 1450 nm. The red line shows the spectral intensity, and the blue line is the integrated sum of the red line. The two dots are located at wavelengths 100 nm (blue) & 120 nm (red) above the central wavelength of the pulse, which correspond to the location of the bandgap when the TOPAS is set to 1450 and 1430 nm, respectively. We can see that over 99% of the pulse energy is contained in wavelengths below the bandgap.

### 4.2.7 laser damage

### 4.2.8 estimation of excited carrier density

**need to include orbital-resolved excitation probability results in this section**

We are concerned with two quantities: the peak excitation fraction in the sample and the average excitation fraction at the location of the XUV focus. The former quantity is relevant when considering sample damage, whereas the latter will be proportional to the measured signal. If the XUV and IR spots are perfectly overlapped at the sample plane, then these two quantities are approximately equal. We first calculate the peak excitation fraction, then we consider how a misaligned beam will affect the measured signal.

The laser propagation calculations in Fig. 2.28 were done for vacuum, but we are concerned with the field in our sample. The electric field inside a dielectric $E_{\text{int}}$ is related to the external electric field by the following equation [78]:

$$E_{\text{int}} = \frac{2}{1+\sqrt{\epsilon}} E_{\text{ext}} \tag{4.2}$$

where $E_{\text{int}}$ is the electric field inside the sample, $E_{\text{ext}}$ is the electric field outside the sample, $\epsilon$ is the dielectric constant and its square root is the refractive index $n_{\text{IR}}$. The internal intensity $I_{\text{int}}$ is the square of the internal electric field. For germanium at $\lambda = 1430$ nm, $n_{\text{IR}} = 4.2481$, and we have the following relations:

$$\begin{aligned} E_{\text{int}} &= 0.381 \times E_{\text{ext}} \\ I_{\text{int}} &= 0.145 \times I_{\text{ext}} \end{aligned} \tag{4.3}$$

Given our laser paremeters, we can estimate the highest carrier density within the sample. First, we estimate the absorbed laser fluence, $F_{\text{abs}}$ [35]:

$$F_{\text{abs}} = F_{\text{inc}} \left(1 - R\right) \left(1 - \exp(-\alpha L)\right) \left(1 + R \exp(-\alpha L)\right), \tag{4.4}$$

where $F_{\text{inc}}$ is the incident fluence, $R$ is the reflectivity equal to the square of the Fresnel coefficient, $\alpha$ is the absorption coefficient and $L$ is the sample thickness. The bracketed terms in Eq. (4.4) are the fraction of fluence transmitted by the first surface, the fraction absorbed by a single pass through the sample, and the additional absorption due to a back reflection off the rear face of the sample. Note that the back-propagating beam will arrive (on average) at a delay of $n_{\text{IR}} L/(2c) \approx 0.7$ fs later than the forward-propagating beam. This time scale is nearly two order of magnitude less than the IR pulse duration, so we should expect any electron dynamics initiated by the back reflection to contribute to the measured signal.

If each absorbed photon corresponds to an excited electron, then the excited carrier density $\Delta N$ is given by the following expression [21]:

$$\Delta N = \frac{F_{\text{abs}}}{\hbar\omega} \frac{1}{L}, \tag{4.5}$$

where $\hbar\omega$ is the IR photon energy. In Eq. (4.5), the quantity $F_{\text{abs}}/(\hbar\omega)$ represents the number of absorbed photons per unit area; dividing this quantity by the sample thickness gives the number of absorbed photons per unit volume. This assumes that the skin depth of the material is greater than membrane thickness, which is true for germanium at these wavelengths.

Finally, we convert the excited carrier density to a fractional excitation. Germanium has $N_{\text{u.c.}} = 2$ valence electrons per unit cell, and each unit cell has a volume $V_{\text{u.c.}} = 4.527 \times 10^{-23}$ cm$^3$. Therefore the fractional carrier excitation is

$$f = \Delta N \frac{V_{\text{u.c.}}}{N_{\text{u.c.}}} \tag{4.6}$$

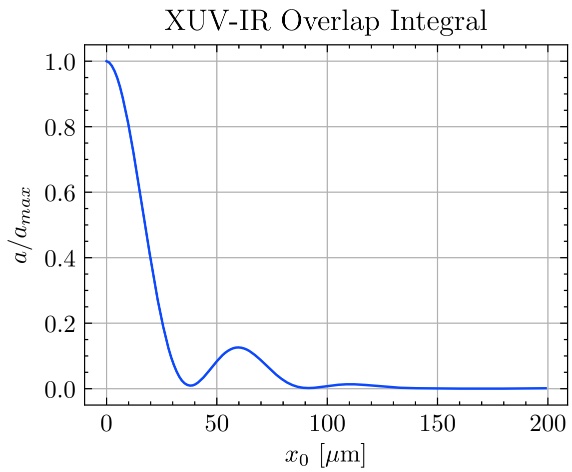


Figure 4.10: XUV-IR overlap function, as defined in Eq. (4.8), calculated using the numerical simulation results of Fig. 2.28 and a Gaussian XUV beam with a 6 $\mu$m waist. The result has been normalized to perfect overlap, $a_{max}$.

We can use literature values for 100 nm of germanium pumped at $\lambda = 1430$ nm light. From the literature [63], $R = 0.38315$, $\alpha = 5803.4$ cm$^{-1}$, and so $F_{\text{abs}} = 0.0413 \times F_{\text{inc}}$. Therefore, only about 4.13% of the incident fluence is absorbed by the sample.

According to the calculations in Fig. 2.28, for each 1 $\mu$J energy input pulse (measured at L4), 0.413 $\mu$J makes it to the focal plane. 49% of that energy is within the main lobe, which contains 0.202 $\mu$J of energy. Approximating the central lobe as a Gaussian beam with a FWHM of 35 $\mu$m and a pulse energy of 0.202 $\mu$J, the peak fluence is calculated by dividing the total energy of the Gaussian by $\pi w^2/2$. The Gaussian beam waist $w$ is related to the FWHM via $w^2 = \text{FWHM}^2/(2\ln 2)$. Thus, for each 1 $\mu$J input energy, the peak fluence in the central lobe is 14.6 mJ/cm$^2$ and the absorbed peak fluence is 0.60 mJ/cm$^2$. This corresponds to an peak excited carrier density of $4.3 \times 10^{20}$ cm$^{-3}$ and an excitation fraction of 0.98% (per 1 $\mu$J of input energy).

### 4.2.9 XUV-IR spatial overlap

The excitation fraction can be computed for each spatial coordinate on the sample using the above method and the predicted intensity distribution from the numerical beam propagation calculations. Because the electrons are being excited via a single-photon process, the excited carrier density will be proportional to the fluence, and thus proportional to the intensity shown in Fig. 2.28. Because the intensity of the XUV is very weak, the absorption of the XUV by the sample is also linear. Thus, we should expect the ATAS signal to be proportional to the XUV-IR overlap integral:

$$a = \frac{\int dV\ I_{\text{IR}} I_{\text{XUV}}}{\int dV\ I_{\text{IR}} \int dV\ I_{\text{XUV}}} \tag{4.7}$$

Here, the integration volume is over the entire sample. If we assume that the intensity distribution does not appreciably change over the thickness of the sample, we can simplify the above equation. This is a reasonable assumption because the sample ($L = 100$ nm) is much thinner the Rayleigh range ($z_R \sim 1$ mm), and the absorption is low ($\sim 4\%$). So we assume the sample is a $\delta$-function in thickness and only evaluate the intensities at the focal plane. With this assumption, the overlap integral becomes:

$$a = L \frac{\int dA\ I_{\text{IR}} I_{\text{XUV}}}{\int dA\ I_{\text{IR}} \int dA\ I_{\text{XUV}}} \tag{4.8}$$

Knife edge measurements have been performed on the XUV light, showing that it has a Gaussian spatial profile with a beam waist of 6 $\mu$m. We write down the spatial profile of the XUV light at the focus:

$$I^{XUV} = I_0^{XUV} \exp\left(-2((x - x_0)^2 + (y - y_0)^2)/w_{XUV}^2\right) \tag{4.9}$$

Here, $I_0^{XUV}$ is the peak intensity and $w_{XUV}$ is the beam waist (radius), defined as the point where the intensity falls to $e^{-2} = 13.5\%$ of its maximum. The lateral shift from the center of the IR focal spot in the horizontal and vertical directions is $x_0$ and $y_0$, respectively. With this formulation, and using the simulation results for the IR spot, the XUV-IR overlap integral is calculated as a function of XUV-IR misalignment $(x_0, y_0)$. This result is shown in Fig. 4.10. Here, XUV beam is translated relative to the IR beam in the horizontal direction ($x_0$ with $y_0 = 0$) and the overlap is computed from Eq. (4.8).

Fig. 4.10 shows the sensitivity of a condensed matter ATAS experiment to relative alignment.[11] A spatial overlap deviation of 10 $\mu$m will cause the XUV-IR overlap - and thus the measured signal - to drop by 20%. Note that a 10 $\mu$m displacement of the IR at the sample corresponds to a 15 $\mu$rad tilting of the hole mirror (HM). There are two ways misalignment can affect experimental results. If the relative positions of the XUV and IR focal spots changes as an experiment is performed, then the recorded ATAS signal would be a function of both the laser-induced dynamics and the XUV-IR spatial misalignment. On the other hand, if the entire experiment is performed using a constant misalignment, we would be exciting the sample to some peak excitation fraction $f$, but our probe would be measuring a lower excitation fraction ($\approx f a/a_{max}$). Consequently, the measured ATAS signal would be lower than otherwise expected, and any attempts to boost the signal by

[11] Note that the relevant parameter in Eq. (4.8) is the relative positions of the two focal spots. We have yet to calculate the sensitivity of spatial overlap to deviations in the input laser pointing.

increasing the interaction intensity could result in permanent laser-induced sample damage.

A condensed matter ATAS experiment has much tighter alignment tolerances than a gas phase experiment. This discrepancy is a simple consequence of sample geometry and density. In either experiment, the measured signal comes from the region of space where the sample density, XUV intensity and IR intensity overlap. The transmission of XUV through the sample is, to first order, $T = \exp(-n\mu_a d)$, where $n$ is the number density, $d$ is the sample thickness and $\mu_a$ is the photoabsorption cross section. As discussed above, for technical reasons the experiment should be designed with $T \approx 1/2$. Therefore, the product $n\mu_a d$ will be approximately constant for any transient absorption experiment.

The number density of a condensed phase sample is determined by the chemistry of the compound and is on the order of $4 \times 10^{22}$ atoms/cm$^3$. The experimentalist is free to engineer clever sample geometries, heterostructures and/or nanopatterns, but the high atomic density (and thus absorption coefficient) dictates a total sample thickness on the order of 100 nm. On the other hand, the spatial profile and density of a gas phase sample is determined by the gas nozzle design and its backing pressure, respectively. A typical nozzle used in our lab produces a gas plume with lateral dimensions on the order of 200 - 500 $\mu$m. This effectively creates a sample that is three orders of magnitude thicker than a condensed phase sample, which relaxes the alignment constraints significantly. This has important consequences for the alignment of the sample.

If the XUV and IR are perfectly collinear, then the beam overlap region is effectively infinite in the propagation direction. In this case, the XUV-IR overlap integral will be positive regardless of any displacement of the sample plane from the focal plane, and maximal when the sample lies in the focal plane. However, if there is a small angle $\delta\theta$ between their $k$-vectors, then the beams will only spatially overlap within a finite region. In this case, the position of the sample plane relative to the beam crossing plane becomes a critical experimental parameter. For an infinitely thick sample (i.e., a chamber effusively filled with gas), it wouldn't matter where the beams crossed as long as they overlapped somewhere within the chamber. Then, the overlap integral would decrease as a function of $\delta\theta$, but it would never go to zero. For a thin sample, the bounds of Eq. (4.7) must enclose the beam overlap region, or else the integral will be zero. Thus, the signal strength of a condensed phase ATAS experiment is roughly 3 orders of magnitude more sensitive to the $z$-position of the sample relative to the focal plane than a gas phase ATAS experiment.

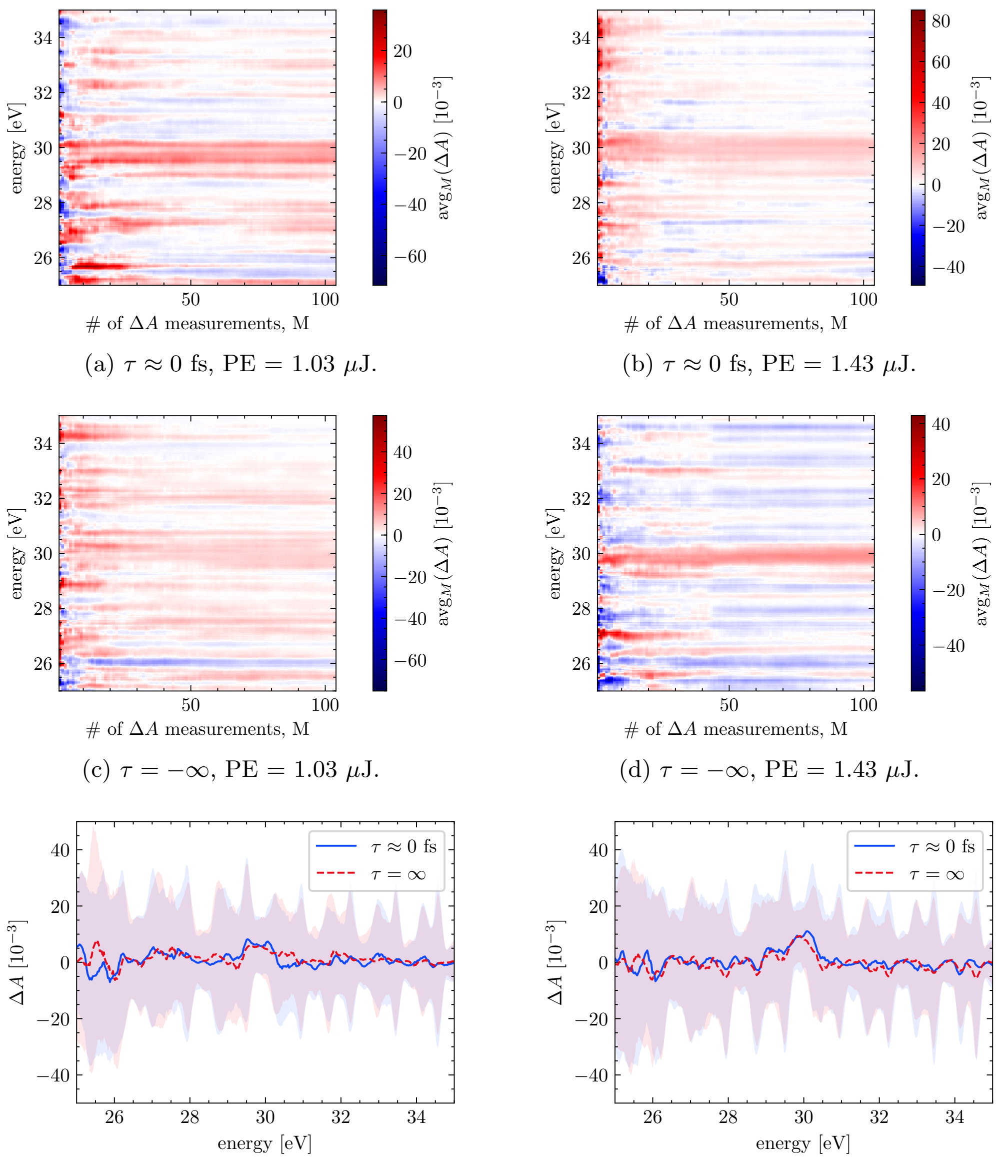


(a) $\tau \approx 0$ fs, PE = 1.03 $\mu$J.

(b) $\tau \approx 0$ fs, PE = 1.43 $\mu$J.

(c) $\tau = -\infty$, PE = 1.03 $\mu$J.

(d) $\tau = -\infty$, PE = 1.43 $\mu$J.

(e) PE = 1.03 $\mu$J.

(f) PE = 1.43 $\mu$J.

Figure 4.11: 1 kHz fixed-delay ATAS measurements on 100 nm Ge using a $\lambda = 1450$ nm excitation pulse. See text for details.

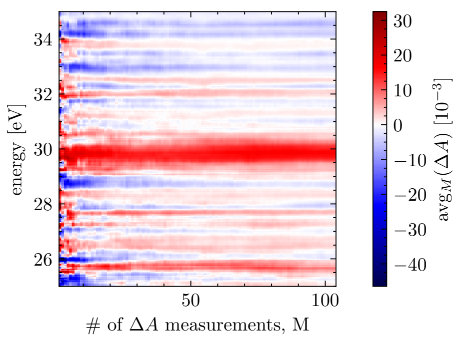


(a) $\tau \approx 0$ fs, PE = 1.75 $\mu$J.

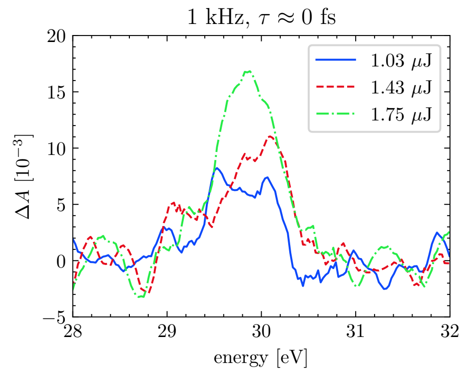


(b) PE scaling at $\tau \approx 0$ fs.

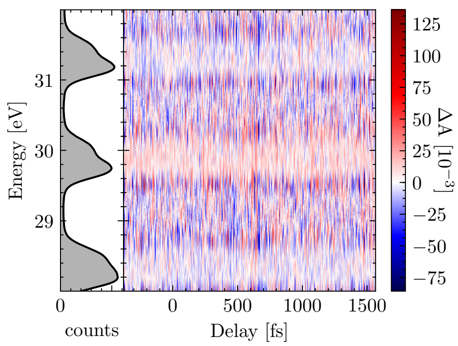


(c) PE = 1.43 $\mu$J.

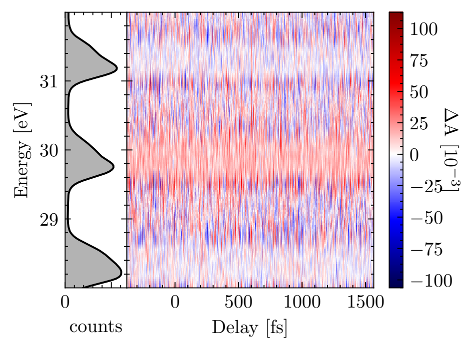


(d) PE = 1.75 $\mu$J.

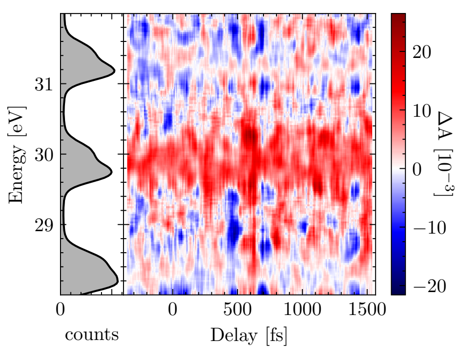


(e) PE = 1.43 $\mu$J (rolling average).

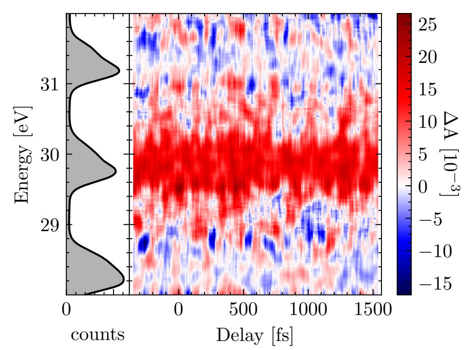


(f) PE = 1.75 $\mu$J (rolling average).

Figure 4.12: 1 kHz ATAS measurements in Ge using a $\lambda$ = 1450 nm excitation pulse. Fig. 4.12a: fixed-delay ATAS measurements with a pulse energy of 1.75 $\mu$J. Fig. 4.12b: Pulse energy scaling at overlap of 1 kHz measurements. Figs. 4.12c to 4.12f: delay scans at 1 kHz. Figs. 4.12c and 4.12d: raw delay scan data. Figs. 4.12e and 4.12f: rolling average of the raw data with a 65 fs window (20 delay points). The left panel on each spectrogram shows the ground state spectrum $S_{gs}(E)$. See text for details.

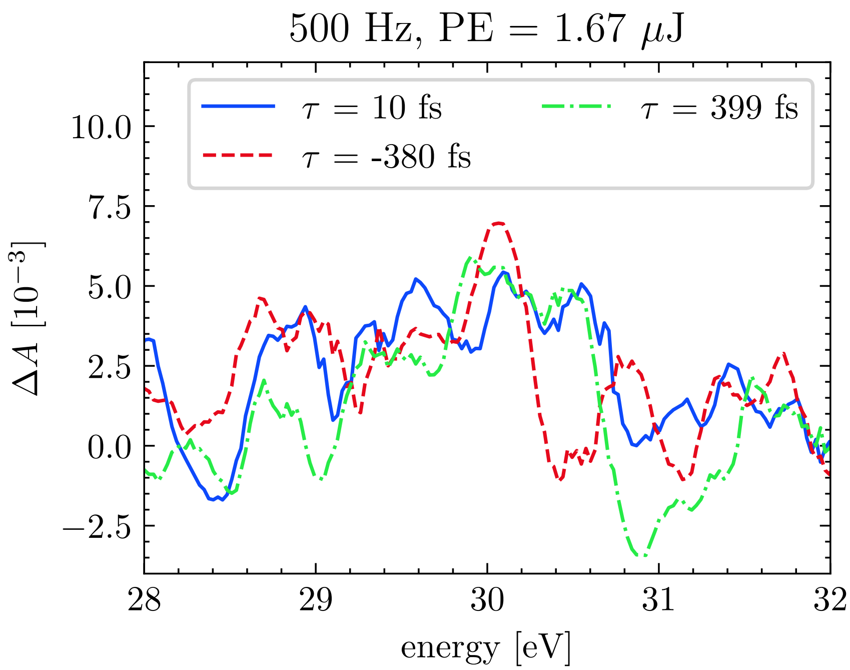


Figure 4.13: 500 Hz ATAS measurements in Ge using a $\lambda = 1450$ nm, 1.67 $\mu$J excitation pulse. Each delay curve is an average of 104 identical measurements. The sample shows no delay dependance within the uncertainty of the measurement.

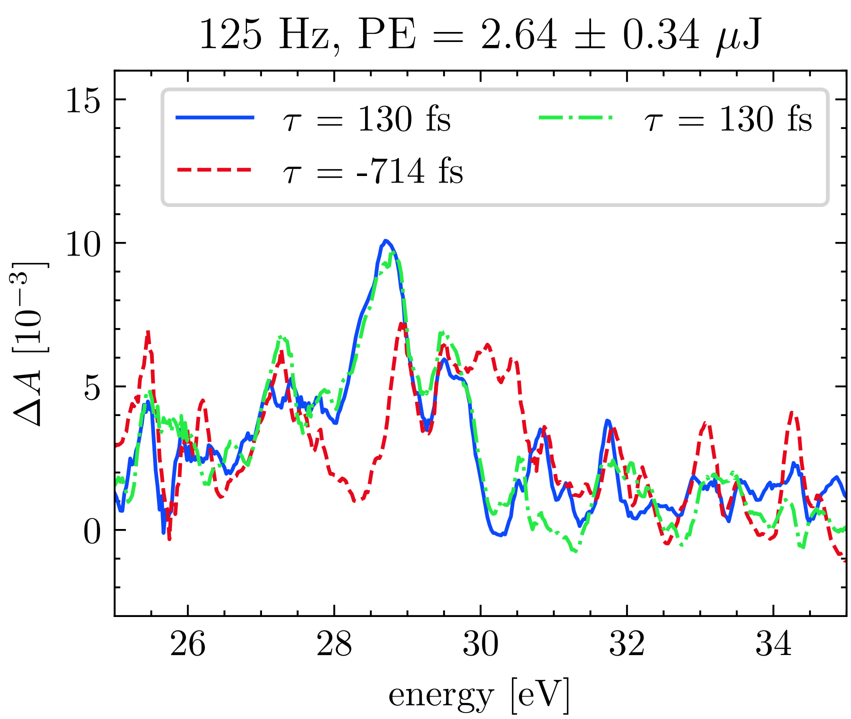


Figure 4.14: 125 Hz ATAS measurements in Ge using a $\lambda = 1450$ nm, 2.64 $\mu$J excitation pulse. Each lineout represents the average of 394 measurements. See text for details.

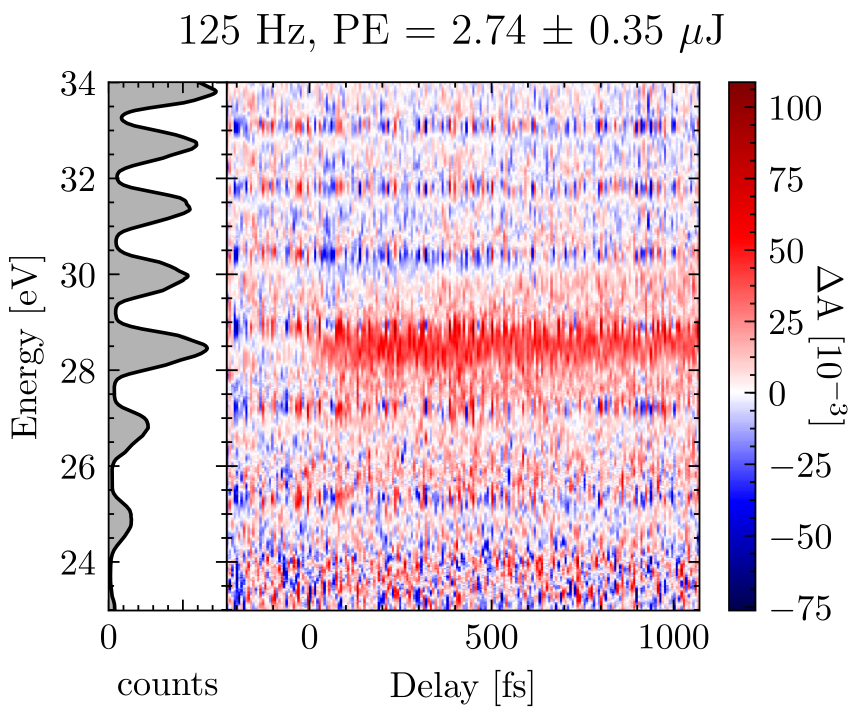


Figure 4.15: 125 Hz delay scan in Ge using a $\lambda = 1450$ nm, $2.74 \pm 0.35$ $\mu$J excitation pulse. This is an average of 3 repeated measurements. See text for details.

## 4.3 Optimizing experimental ATAS parameters for Germanium thin films

### 4.3.1 rep rate (avoiding ms-scale excitation)

We performed exploratory experiments at 1 kHz to determine the optimal excitation pulse energy. For this set of measurements, we generated harmonics in Argon using $\lambda = 1450$ nm, a 200 nm Al filter and the $2C$ optics removed (see Fig. 2.16). Two delay points were recorded: with the XUV and IR pulses overlapped ($\tau = 0$) and with the XUV pulse arriving about 300 fs before the IR ($\tau = -\infty$). For each delay point, we used three pulse energies: 1.03, 1.43 and 1.75 $\mu$J. To increase the signal-to-noise, we performed each experiment 104 times and averaged the datasets. The exposure time was 0.5 seconds, and the sample was rastered so that each measurement was recorded at a new position on the sample. The results are shown Figs. 4.11, 4.12a and 4.12b.

Figs. 4.11a to 4.11d and 4.12a show the average $\Delta A$ as a function of the number of averaged measurements, $M$. Spectral features are apparent after averaging about 10 datasets together, but the fidelity of the signal does not appreciably improve after the first $M = 50$ datasets. Figs. 4.11e and 4.11f show the average signal (lines) and the standard deviation (shaded area), as calculated from the entire ensemble of measurements. The data is noisy, but we can see a spectral feature near 30 eV which scales with pulse energy (or perhaps average power). This behavior is evident in Fig. 4.12b. However, this feature is delay-independent: $\Delta A$ has nearly the same value regardless of whether the XUV arrives before or after the IR pulse.

To confirm the delay-independence of this feature, we performed delay scans at two different pulse energies (1.43 and 1.75 $\mu$J). These measurements are shown in Fig. 4.12. Delay was controlled by inserting a fused silica wedge into the inteferometer (W in Fig. 2.16). Each delay step corresponds to approximately 3.25 fs (25 $\mu$m of wedge insertion).

The raw data is shown in Figs. 4.12c and 4.12d. As this experiment was only performed once ($M = 1$), the contrast is poor and the 30 eV feature is barely visible. The spectral feature becomes more prominent after performing a rolling average over 20 delay points (65 fs), which is shown in Figs. 4.12e and 4.12f. These delay measurements confirm our suspiscion that the absorption feature is delay-independent at 1 kHz.

One possible origin of a delay-independent signal can be a very long-lived excited state with lifetime $1/\Gamma$. Each laser shot initiates an assortment of electron and phonon dynamics, each with their own time scales. If any of these excited states have time scales that approach the inverse rep. rate of the laser ($1/RR$), then the dynamics from the previous shot will still be evolving by time the next shot arrives. Since each exposure integrates over hundreds or thousands of laser shots, measurements at a nomimal delay $\tau$ will contain information from several delays $\tau_i$, each separated by the time between laser shots: $\tau_i = \tau, \tau - \frac{1}{RR}, \tau - \frac{2}{RR}, \ldots$, with the amplitude of each contribution weighed by an exponential decay factor $\exp(+\tau_i \Gamma)$. If this is the case, then the magnitude of the delay-independent signal should decrease as time between laser shots is increased. As the time between laser shots is increased past the lifetime of the state, the excited state population from the previous laser shot will be small enough to observe the dynamics of the shorter-lived states. Experimentally, we can accomplish this by adjusting the rep. rate divider on the Spitfire amplifier (which reduces the rep. rate), and/or using an optical chopper.

The rep. rate was halved to 500 Hz using the Spitfire's rep. rate divider ($m = 2$) and the exposure time was doubled to 1 second so that the number of laser shots per exposure was held constant. A series of fixed-delay measurements were recorded using a 1.67 $\mu$J pulse energy, shown in Fig. 4.13. The spectral feature at 30 eV is still present, but it does not exhibit any delay dependence within the uncertainty of the measurement. It is notable that, for a similar pulse energy, the magnitude of the feature at 500 Hz is half that of the 1 kHz measurement. This is consistent with the hypothesis of a long-lived state contributing to the signal.

The rep. rate was lowered to 125 Hz using a combination of the rep. rate divider ($m = 4$) and an optical chopper ($T = 50\%$) placed after the TOPAS. The exposure time was increased

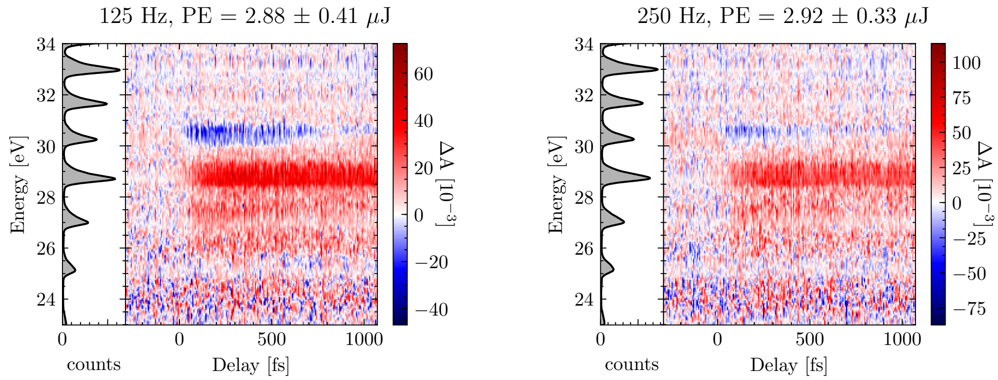


(a) 125 Hz ($M = 6$)

(b) 250 Hz ($M = 2$)

Figure 4.16: 125 vs. 250 Hz measurements at $\lambda = 1430$ nm.

to 4 seconds to maintain sufficient counts on the detector. An ATAS spectrum was recorded about 130 fs after temporal overlap and several hundred fs before overlap using a $2.64 \pm 0.34$ $\mu$J excitation pulse ($\lambda = 1450$ nm), as shown in Fig. 4.14. A second measurement after overlap was recorded to ensure repeatability. At negative delays (red curve), we see the familiar 30 eV feature, albeit weaker at $6 \times 10^{-3}$. Near overlap, we see a new feature emerge at 28.7 eV, with a magnitude of $\approx 10 \times 10^{-3}$. This observation is consistent with long-lived excited state at 30 eV. A delay scan at 125 Hz, shown in Fig. 4.15, reveals that the 28.7 eV feature is indeed time-dependent with a ps-scale lifetime.

### 4.3.2 IR pulse energy

### 4.3.3 harmonic spectrum ($\lambda$, 2-color generation)

The fundamental wavelength was decreased by 20 nm to 1430 nm, where the absorption length in Ge is about 5% shorter. For a fixed pulse energy, this increases the excitation fraction and thus the strength of the $\Delta A$ signal. Changing the wavelength also changes which initial and final states near the Fermi level are populated, according to the band structure calculations in Fig. 4.8. Using this shorter wavelength we can observe a more robust sample response, as shown in Fig. 4.16.

At 1430 nm, we can see a sample response from 25.7 to 31 eV. From 25.7 to 30 eV, there is a broad increase in absorption, with the largest increase occuring between 28.4 and 29.5 eV. A decrease in absorption occurs between 30 and 31 eV. These features are present in both the 125 and 250 Hz data. The 30 eV negative delay feature persists in the 250 Hz dataset, but at $12 \times 10^{-3}$ it does not overwhelm the rest of the sample response. Further measurements were performed at either 125 Hz to suppress the static feature, or at 250 Hz to minimize data collection time.

cartoon showing
2D image -> lineout
-> deltaA
calculations &
normalization

Figure 4.17: this cartoon shows the data pipeline. it is an overview of all the processing steps i do on the data.

### 4.3.4 optimized ATAS Ge experimental results

### 4.3.5 post-experiment analysis: verify we didn't permanently damage sample

## 4.4 Data Analysis

### 4.4.1 description of data pipeline

#### going from 2D image to 1D spectra

background subtraction, selecting a divergence window, normalization by exposure time & divergence window, integration over divergence window

energy calibration:
Ar fano features vs
pixel

Figure 4.18: this figure shows the argon fano features vs pixel for the purpose of calibrating the spectrometer.

**energy calibration**

**$A$, $\Delta A$ calculation**

#### 4.4.2 systematic noise sources in our experiment

#### 4.4.3 methods to numerically correct for harmonic noise and drift

#### 4.4.4 frequency filtering to remove $\omega, 2\omega$ oscillations

### 4.5 Physical Interpretation of spectra

#### 4.5.1 decomposition of spectral response

#### 4.5.2 description of observed dynamics

# Chapter 5
# Conclusions

say something here ...

# Appendix A
# Guidelines for using the TABLe

## A.1 OMRON Pump-down Procedure

Special thanks for Andrew Piper for coding and installing the OMRON safety system. Below is an operational guideline to pump the system down to UHV using the OMRON system. Please see Andrew Piper's OMRON manual for additional details on the microcontroller system.

This procedure assumes that the chambers are initially at atmospheric pressure, the rough pumps are turned on, and the solenoid shutoff valves on the roughing line are closed.

1. Seal and isolate all chambers. Close the manual hand valves between each turbo pump and the solenoid shutoff valves. Reattach any blow-off flanges (KF-25 blanks) that may have come off from the previous venting cycle.

2. Ensure the OMRON's, safety system is engaged by attempting to open one of the pneumatic gate valves via the control panel. **Caution: operating a gate valve between two chambers with a pressure differential can cause catastrophic system failure! Only perform this step after you have verified that all chambers are at atmospheric pressure!** If the gate valve opens while both chambers are above the upper setpoint, then the OMRON, safety system has been disabled. Enable the safety system by switching the override switch to OFF.

3. Retract the metal filters from the beam path to protect them from potential pressure surges.

4. Initiate the pump-down sequence by pressing the OK button on the OMRON. This will open all solenoid valves simultaneously with a loud *thunk!*

5. Slowly open the manual handvalves while monitoring the pressure load on the rough pumps to avoid overloading the rough pump system. Use the two Raspberry Pi remote pressure monitoring systems to monitor the inlet pressure for each blower

system. As a rule of thumb, try to keep the inlet pressure below ≈100 Torr during this step. **Warning: overloading the rough pumps will result in pump oil being expelled into the rough pump's exhaust line. Continuing to run in this condition can lead to overheating and eventually seizing of the rough pump.**

6. Once the hand valves are fully open on all chambers, you can turn each blower system ON to accelerate the remaining pump-down procedure.

7. Power on the turbo power supplies and switch the turbos to ON. After a few seconds, the magnetically levitated turbos will start levitating with a soft *thunk!*.

8. Each turbo will automatically start spinning when its chamber reaches the upper set point (about 200 mTorr). The turbos will take a few minutes to reach their final speed.

9. Wait for the system to pump down. It typically takes 15-45 minutes for the entire system to reach $10^{-6}$ Torr.

10. The pneumatic gate valves for adjacent chambers will be enabled when both chambers are below their lower setpoint pressure (about $5 \times 10^{-6}$ Torr). Once all chambers are below their lower setpoints, the OMRON considers the system is to be fully pumped down.

11. ARM each chamber by pressing ESC + [chamber number]. The OMRON's display will update to show which chambers are armed (G: generation & differential pump chambers, M: mirror chamber, T: target chamber, S: photon spectrometer chamber).

## A.2 OMRON Venting Procedure

The OMRON system was designed with the ability to vent any single chamber or combination of chambers while keeping the others pumped down. This was a possibility when each chamber had its own rough pump, but now that the mirror, target & spectrometer chambers share a single blower system, extra care must be taken. **Any chambers that share a backing rough pump must be vented simultaneously to avoid turbopump overload.** For example, the mirror chamber, target chamber and spectrometer share a common blower system, and attempting to vent the one chamber while keeping the others will result in the spectrometer's turbo pump crashing due to the high backing pressure in the rough line.

This procedure assumes an initial condition of all chambers pumped down to UHV with the turbos running.

1. Turn off all gas sources / loads. If the HPC is installed, follow the HPC shutdown procedure.
2. Turn off the blowers.
3. Block the laser into the interferometer.
4. Close the pneumatic gate valves.
5. Disarm the chambers by pressing ESC + [chamber number].
6. Verify the OMRON's safety system is not disabled by checking the bypass switch.
7. Enable the venting valves by switching ON the vent & purge controls on the control panel. The chambers will not vent without this step!
8. Remove the KF clamps on the blow-off valves.
9. Start the OMRON venting script by pressing ALT + [chamber number] on the OMRON.
10. The user can now walk away from the system. It will take a few hours to vent.

The venting script will immediately stop the turbopump's motors, open the solenoid venting valves after 30 seconds, close the roughing line's solenoid valves after 30 minutes, and close the solenoid venting valves after about 5 hours. The preceding timeline was chosen following the manufacturer's recommendation, and to avoid closing the roughing line's valves before the turbos had completely stopped spinning.

## A.3 Aligning the Interferometer

### A.3.1 the generation arm

#### The Ellipsoidal Mirror

### A.3.2 the pump arm

### A.3.3 finding spatial overlap

### A.3.4 finding temporal overlap

## A.4 Pointing into the Interferometer

the importance of pointing into the interferometer - spatial and temporal alignment

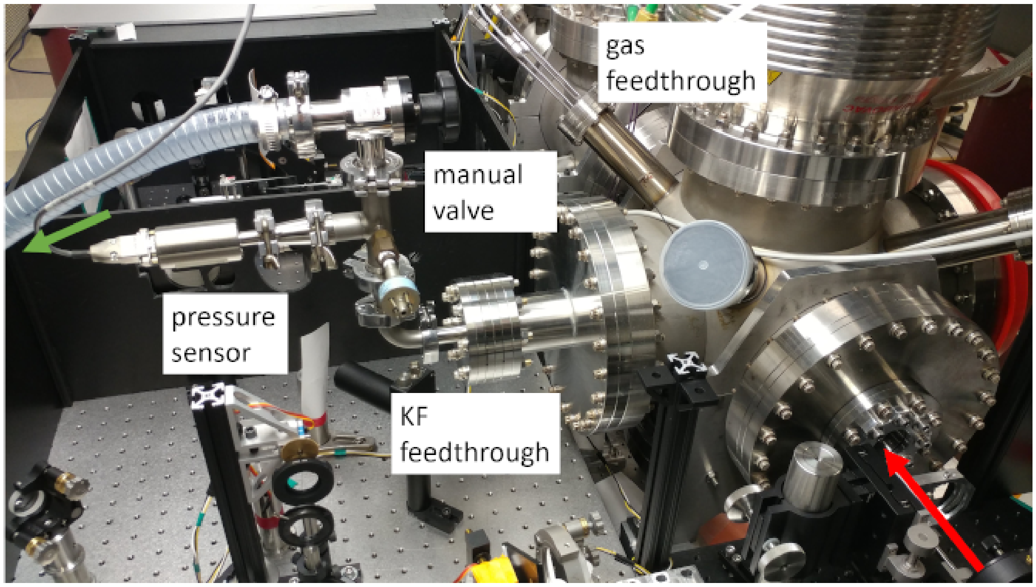


Figure A.1: Exterior view of the generation chamber with the HPC installed showing the ancillary vacuum hardware. Red arrow indicates input laser path; green arrow points towards the HPC's RV pump.

## A.5 The High Pressure Cell (HPC)

### A.5.1 Introduction

*main text: description of the HPC's design, pressure & harmonic performance, pressure modeling, phase matching considerations. this section: how to install and actually use the HPC, how to machine or reorder certain parts.*

- focal length considerations. range of acceptable focal lengths. advantages of reflective vs transmissive focusing. possible schemes for shorter focal lengths.

- space constraints of TABLe generation chamber limit the size of the XYZ stack. these are Newport 9066 1/2" travel stages, with 1" travel thorlabs motors (that's what we had, ideally you would use 1/2" motors). as a result, you can accidentally drive the motor more than the stage will allow. this will result in the motor falling out of the stage. in this case, you will have to immediately block the laser, vent the chamber, and reattach the motor. note: travel of all motors is from 0 to 14 mm.

- in-vacuum manipulation via the vacuum bellows (limits of motion, max pressure differential)

The ancillary vacuum hardware can be seen in Fig A.1. A small oil-lubricated RV pump (not shown in this picture) provides differential pumping to the interior of the HPC. An inline Baratron diaphragm pressure sensor (effective range: 1 - 760 Torr) tracks the interior pressure of the edge-welded bellows. A manual gate valve is used to isolate the HPC from

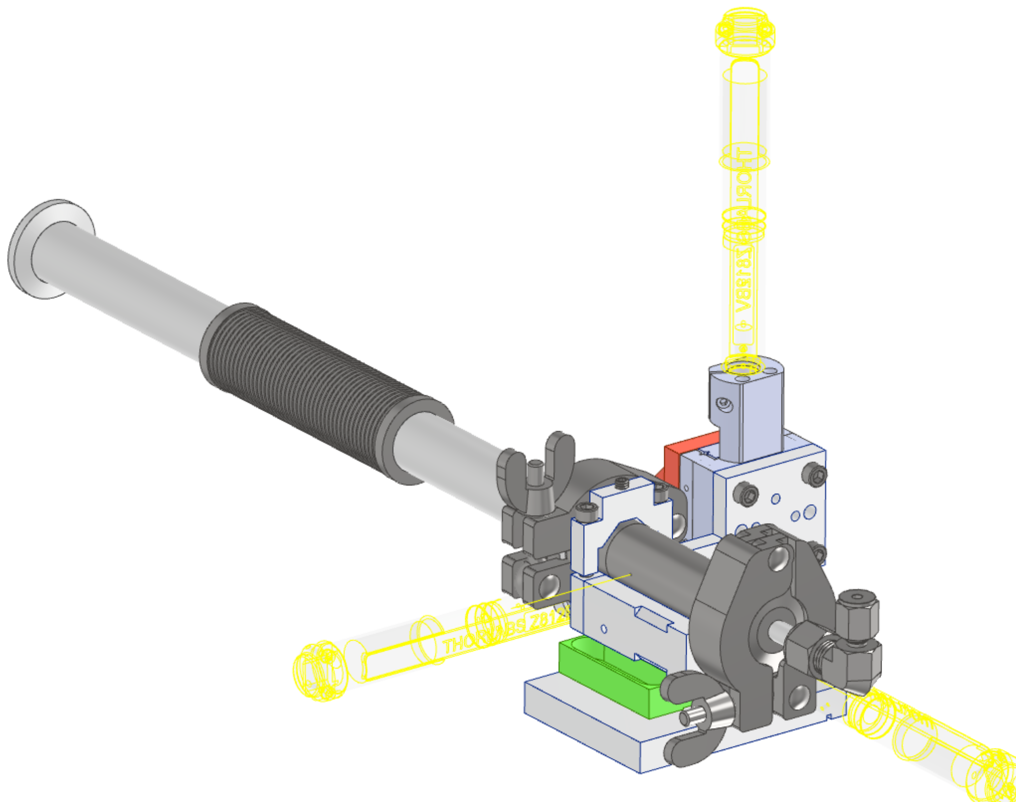

Figure A.2: The HPC with bracket installed on the XYZ translation stage, configured for the generation chamber. The hose clamp and gas supply tube is omitted from this drawing for clarity.

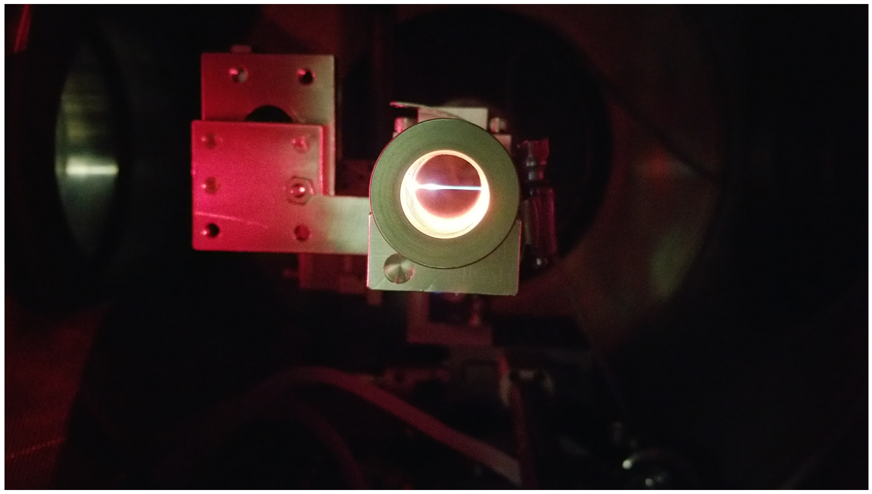

Figure A.3: Laser filament in the aligned outer pipe of the HPC. The inner pipe is not yet installed. Alignment of the outer pipe is done at very low intensities; after alignment the power was increased to create a filament for illustrative purposes only. This picture was taken in the target chamber during the initial testing of the HPC. The geometry of this chamber requires that the orientation of the mounting bracket is reversed compared to what is shown in Fig A.2.

the RV pump when the additional pumping is not needed. Right angle KF fittings were used to route the HPC's vacuum line above the pump arm of the interferometer.

### A.5.2 Initial Installation and Alignment

First, a note about laser safety. The following alignment procedure should be done at the lowest possible laser power to minimize both accidental drilling of the HPC and the danger posed by stray light. Stray reflections or scatter from the many metallic surfaces of the HPC assembly pose a potential safety risk during alignment. The surface most likely to cause laser scatter is the front face of the outer pipe, which is roughened stainless steel located about 3/8" before the focus. The material's roughness and the negative radius of curvature of the incoming light make it unlikely that incident light will coherently focus to a point upon reflection. However, it is possible that the sidewall of the outer pipes's aperture could act as a focusing mirror. Additionally, the hose clamp or mounting bracket could coherently reflect light towards the user. The user is advised to strictly follow all laser safety protocols during this alignment procedure. Whenever possible, direct observation of the laser beam on the surfaces of the HPC should be avoided, instead a webcam should be used to view the interior of the generation chamber.

The initial installation of the HPC can be time consuming and tedious, but once installed it will retain its alignment for a period of weeks or months. The pointing into the cell should

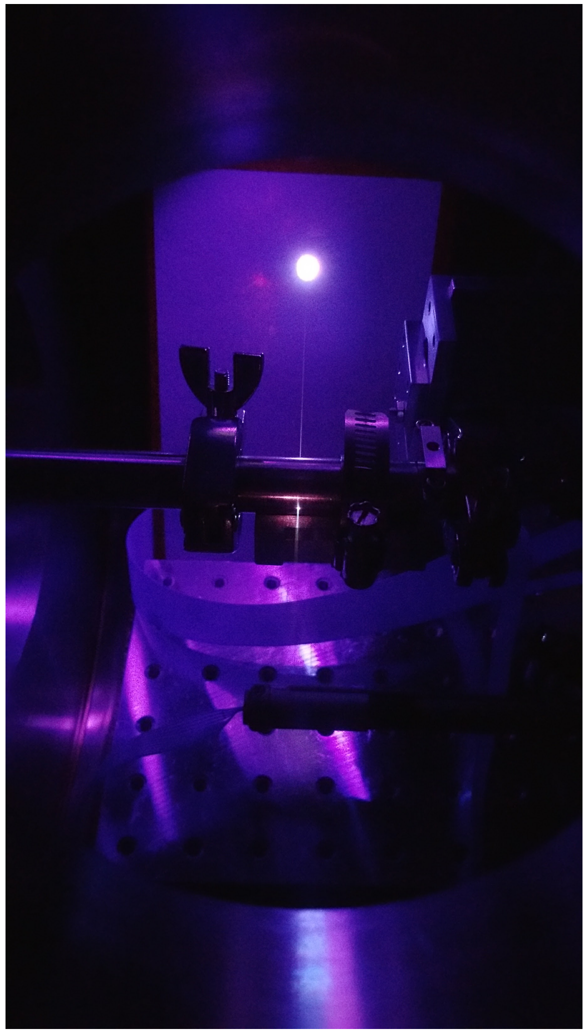

Figure A.4: Laser drilling the inner pipe. A card blocks the laser after exiting the HPC. The HPC was pressurized with Ar gas to enhance the filament for illustrative purposes.

be done on a daily basis, but this is only slightly more complicated than what must be done with a free expansion gas jet.

Optically, the HPC cell consists of four pinhole apertures (diametrically opposed pinholes on both the inner and outer pipes) with the laser focus near the center of the inner pipe. The optical transmission of the HPC is therefore very sensitive to the relative alignment of these components, as well as the pointing of the laser into the HPC. To simplify the alignment, the two innermost holes are laser drilled *in-situ* after the outer pipe has been aligned. To maintain the relative alignment of the inner & outer apertures, the user should refrain from adjusting the inner pipe after the initial alignment is completed. Therefore, daily alignment of the HPC should be performed using only the in-vacuum motorized XYZ stages.

The first step of the HPC installation is installing the rough vacuum feedthrough flange. The TABLe's generation chamber uses a custom flange (a 4.5" CF blank with a KF16 half nipple welded to the air-side and a KF16 bulkhead groove & tapped holes machined into the vacuum side). To accommodate the length of the in-vacuum bellows, we use a custom 10" CF to 4.5" CF reducing nipple (OAL = 4.25"), which acts as a spacer between the feedthrough flange and the KF16 flange on the HPC. Although it was absent from the original design, a spacer 4.5" CF flange (thickness = 0.68") between the feedthrough and the reducing full nipple is used to relax the compression in the bellows and allow for a larger range of motion. For convenience, the user should install the edge-welded bellows to the bulkhead flange before installing the flange on the chamber.

The supporting bracket for the HPC was designed to be interchangeable with the free gas nozzle's bracket. This design, shown in Fig. A.2, allows the user to change the gas source type without disturbing the alignment of the XYZ stage to the optical axis. For completeness, we will assume that the XYZ stage has been misaligned or removed from the chamber. First, the user should align the laser to the interferometer so that the laser path in the generation chamber can be used as a reference. Then, the stage should be positioned in the chamber so that the focus is roughly in the center of the stage's motion. Finally, the stage's z-direction should made parallel to the optic axis. This can be done by tracking the position of the laser on a card mounted to the stage while moving the stage upstream and downstream of the focus. After clamping the stage to the breadboard, check that the alignment is still true before continuing to the next step.

The next step is to align the outer pipe of the high pressure cell by maximizing its light transmission. This is best done in two steps: first, coarse alignment is done visually at low power (insufficiently intense to laser drill the pipe), followed by fine adjustments using a power meter at moderate intensities (above the noise floor of the power meter). Note that accidentally drilling out the outer pipe will reduce its differential pumping performance. Given the chamber's small size, it is not practical to place a power meter in the generation chamber after the focus during the alignment procedure. Rather, it is preferable to divert the beam out of the vacuum system using the linear actuator & silver mirror assembly located approximately 85 cm downstream of the focus.[12] When inserted, the linear actuator intersects the beam path and redirects the beam out of the vacuum system through a window onto the upper deck of the optical table. The beam size can be reduced using a focusing lens onto the face of a power meter. Note that for most generation focusing conditions, the large beam size at the diverting mirror makes this beam path lossy. To accurately calculate the transmission through the HPC, it is necessary to measure the power immediately after the HPC in the generation chamber.

For the coarse alignment, the input beam intensity should be reduced using an upstream iris, to the point that it is barely visible near the focus. Since a tightened KF connection prevents rotation of the components, the alignment of the outer pipe is done prior to making any KF connections. However, the KF clamps should be fitted on either end of the pipe to ensure that there is enough room to make the connections without disturbing the alignment once finished. The outer pipe should be placed in its cradle, with the aluminum & hose clamps made snug around the pipe but not taut.[13] Transmission should be optimized by iteratively tuning the following parameters: (1) rotation of the pipe in the cradle, (2) height of the cradle using the vertical motor, and (3) horizontal (transverse) position of the assembly using both the horizontal motor and the position of the pipe in the cradle. For fine adjustment, the iris should be adjusted so that the power meter reads about 20-30 mW when measured after the linear actuator.[14] The clamps should be tightened so that movement of the pipe is possible, but difficult. The area around the power meter should be covered to prevent air currents from affecting the measurement. The transmitted power should be optimized using the same procedure as before.

Once the outer pipe is aligned, tighten all connections and connect the bellows to the outer pipe. Check that the alignment has not been changed by torquing these connections. Verify that the unattenuated laser beam can pass through the outer pipe without interference, as shown in Fig. A.3. If everything looks good, we can proceed to install the inner pipe.

First, attach the gas delivery feedthrough flange onto the HPC assembly without the inner pipe. Being mindful to not disturb the alignment of the outer pipe, check that the gas delivery tubing does not interfere with the laser path. Remove the gas delivery feedthrough flange, cut the inner pipe to length (OAL = 1.75"), and make the Swagelok connection between the inner pipe and the KF feedthrough. Make sure the inner pipe is normal to the

[12]Special thanks to Eric Moore for designing and installing this optomechanical component.

[13]The HPC's XYZ assembly and bracket were designed for the TABLe generation chamber. If it is being installed elsewhere, the user should verify that the height is correct. When installed correctly, the bottom of the Z-motor range should correspond to the HPC lowered completely out of the way of the laser; the top of the range should correspond to the laser going through the center of the HPC, with about 1 mm to spare.

[14]This power is appropriate for a 1kHz repetition rate and a generation focal length of 30 or 40 cm.

flange's sealing surface, otherwise the laser will skim the sidewall of the inner pipe rather than go through the center. Install the gas delivery assembly onto the HPC assembly by tightening the KF clamp.

Laser drilling the inner pipe will sputter a significant amount of metal onto the inner surfaces of the chamber. Since the active drilling surface is on the upstream face of the pipe, most of the material will go upstream. Therefore, the laser window needs to be swapped out for a "sacrificial" window prior to drilling.[15] Out of an abundance of caution, close the gate valve to the mirror chamber, retract the linear actuator & silver mirror from the beam path, and block the generation chamber's vacuum aperture with a card.

Laser drilling should be done with the appropriate safety precautions: wearing laser goggles, notifying fellow labmates of your activity, and posting signs on the entrances to the lab. The user can cover up the chamber's flanges and set up a webcam to remotely monitor the laser drilling status to minimize the risk of inadvertent laser exposure.

At this point, the actual process of laser drilling is quite simple. There is no way to control the exact positioning of the inner pipe relative to the outer pipe, so there are no adjustments to make. Rather, the design relies on the mechanical alignment of the inner pipe relative to the outer pipe, which is ultimately set by the gas feedthrough weld, the Swagelok and the KF fitting. On the other hand, a used inner pipe cannot be reinstalled to the HPC once it is removed, since alignment is effectively impossible. To laser drill the pipe, simply let the unattenuated beam into the chamber and wait a few minutes until the laser emerges from the exit of the HPC. See Fig. A.4.

If you are planning on scanning the k-direction of the HPC during an experiment, you should do so now while you are set up for laser drilling. Similarly, if you are using a non-reflective (achromatic) focusing scheme and are planning on changing wavelengths during your experiment (which will change the effective focal length), you should step through the full range of wavelengths while drilling. Doing so will open up the apertures slightly, resulting in additional metal deposition on the sacrificial laser window.

After laser drilling is complete, reinstall the laser window and verify the HPC has retained its alignment.

### A.5.3 Alignment with the HPC Installed

The daily pointing procedure, described in A.4, is largely unchanged by the presence of the HPC. However, there are some extra considerations that need to be made if the HPC is

[15] After drilling, the sacrificial window will be completely coated with a thin metal film. Most of the metal can be removed using methanol, but don't expect to be able to use the window for anything but laser drilling. Using a window with different optical properties (i.e., thickness or material), or no window at all, will change the pointing and effective focal length of the beam. It has been suggested that the laser window could be protected by placing a thin sheet of transparent plastic (Saran Wrap) between the window and the HPC, but we haven't tested this method.

installed. The small apertures of the HPC and the non-linear nature of HHG demand high accuracy in the pointing into the cell, so small corrections to the positioning of the HPC have to be made after the daily pointing procedure is completed.

#### Pointing into the Interferometer

If the interferometer is already aligned, the presence of the HPC does not really complicate the daily procedure of the beamline. In this case, the user should block the laser into the generation chamber and align the pointing into the interferometer using the pump arm, as usual.[16] The procedure described in A.4 is sufficiently accurate to get the laser through the HPC, but it won't necessarily yield optimized harmonics. Rather, the user may have to make small tweaks to the transverse position of the HPC. This can be done by optimizing the harmonic flux by making small (10 - 25 $\mu$m) steps using both the vertical and horizontal HPC motors while monitoring the harmonic yield using a fast camera exposure ($< 0.5$ s). In our experience, the optimal HPC position is typically within 50 $\mu$m of the previous day's position.

The HPC's apertures may no longer be circular if the HPC has been subjected to accidental laser drilling or significant laser drift. Non-circular apertures may result in a complex spatial profile of the harmonics, which can make the optimization of the harmonic yield difficult.

#### Aligning the Interferometer

If the interferometer needs to be realigned, then the HPC must be lowered out of the way of the laser. This is because the spatial mode of the IR is distorted by the HPC's apertures, which can introduce small shifts in the pointing of the IR after the HPC. Once the HPC is out of the way, the alignment procedure described in A.3 can be followed without modification. Unless major changes were made to the interferometer, the angle of the HPC's apertures should remain aligned to the k-vector of the generation arm. In this case, the optimal position of the HPC can be found by maximizing the transmitted power of an the attenuated laser through the HPC, as described in the latter part of A.5.2. If major modifications were made to the interferometer, the user should consider aligning the HPC from scratch.

### A.5.4 Pump Down Procedure

- pump down procedure
    - generating and optimizing harmonics
    - max internal pressure / pressure differential of the bellows tube

[16] Failure to block the laser prior to changing the pointing may result in laser-drilling the HPC.

- max displacement of the tube

### A.5.5 Startup and Shutdown

## A.6 Laser System Specifics

importance of pointing & laser performance for our experiments

### A.6.1 The Spitfire

#### Regular Maintenance

- cleaning the stretcher
    - increasing the pump laser currents
    - changing the chiller fluid, desiccants, etc

#### quirks and features

- regen cavity tweaks
    - photodiode problems
    - software issues - bugs and troubleshooting

### A.6.2 Pointing Stabilization into the External Compressor

- dietrich plots for pointing

### A.6.3 The Spitfire's External Compressor

#### external compressor alignment

#### cleaning the grating

### A.6.4 The TOPAS-HE

- aligning - importance of power stability and pointing stability

### A.6.5 stability

- boxing things up - power stability throughout the day, people in the lab - unstable harmonic yield from the HPC at high pressures

## A.7 The Shutter System

## A.8 The Vacuum System

- blower upgrade
    - remote pressure sensing
    - vacuum calculations for steady state pressure of beamline

## A.9 Required Maintenance

vacuum system (rough pumps, blowers, turbos) and spitfire (cleaning the gratings)

## A.10 Best practices: data acquisition

read-out noise from camera. (how noise scales)

# Bibliography

[1] M. V. Ammosov, N. B. Delone, and V. P. Krainov. Tunnel ionization of complex atoms and of atomic ions in an alternating electromagnetic field. *Sov. Phys. JTEP*, 64(6):1191–1194, 1986.

[2] J. Arnaud. Representation of Gaussian beams by complex rays. *Appl. Opt., AO*, 24(4):538–543, Feb. 1985.

[3] D. T. Attwood. *Soft X-Rays and Extreme Ultraviolet Radiation: Principles and Applications.* Cambridge University Press, Cambridge ; New York, 2000.

[4] D. R. Austin, K. R. P. Kafka, Y. H. Lai, Z. Wang, C. I. Blaga, and E. A. Chowdhury. Femtosecond laser damage of germanium from near- to mid-infrared wavelengths. *Opt. Lett., OL*, 43(15):3702–3705, Aug. 2018.

[5] P. Balcou, A. S. Dederichs, M. B. Gaarde, and A. L\textquotesingleHuillier. Quantum-path analysis and phase matching of high-order harmonic generation and high-order frequency mixing processes in strong laser fields. *J. Phys. B: At. Mol. Opt. Phys.*, 32(12):2973–2989, Jan. 1999.

[6] P. Balcou, P. Sali‘eres, A. L'Huillier, and M. Lewenstein. Generalized phase-matching conditions for high harmonics: The role of field-gradient forces. *Phys. Rev. A*, 55(4):3204–3210, Apr. 1997.

[7] C. Bourassin-Bouchet, M. M. Mang, F. Delmotte, P. Chavel, and S. de Rossi. How to focus an attosecond pulse. *Opt. Express, OE*, 21(2):2506–2520, Jan. 2013.

[8] S. Byrnes. Tmm: Simulate light propagation in multilayer thin and/or thick films using the fresnel equations and transfer matrix method., Feb. 2017.

[9] S. J. Byrnes. Multilayer optical calculations. *arXiv:1603.02720 [physics]*, Nov. 2019.

[10] A. Camper, A. Ferré, V. Blanchet, F. Burgy, D. Descamps, S. Petit, T. Ruchon, and Y. Mairesse. Combined high-harmonic interferometries for vectorial spectroscopy. *Opt. Lett., OL*, 40(22):5387–5390, Nov. 2015.

[11] A. Camper, A. Ferré, N. Lin, E. Skantzakis, D. Staedter, E. English, B. Manschwetus, F. Burgy, S. Petit, D. Descamps, T. Auguste, O. Gobert, B. Carré, P. Salières, Y. Mairesse, and T. Ruchon. Transverse Electromagnetic Mode Conversion for High-Harmonic Self-Probing Spectroscopy. *Photonics*, 2(1):184–199, Mar. 2015.

[12] A. Camper, H. Park, S. J. Hageman, G. Smith, T. Auguste, P. Agostini, and L. F. DiMauro. High relative-phase precision beam duplicator for mid-infrared femtosecond pulses. *Opt. Lett., OL*, 44(22):5465–5468, Nov. 2019.

[13] A. Camper, T. Ruchon, D. Gauthier, O. Gobert, P. Salières, B. Carré, and T. Auguste. High-harmonic phase spectroscopy using a binary diffractive optical element. *Phys. Rev. A*, 89(4):043843, Apr. 2014.

[14] T. Carette, J. M. Dahlström, L. Argenti, and E. Lindroth. Multiconfigurational Hartree-Fock close-coupling ansatz: Application to the argon photoionization cross section and delays. *Phys. Rev. A*, 87(2):023420, Feb. 2013.

[15] Z. Chang. *Fundamentals of Attosecond Optics.* CRC Press, Boca Raton, 2011.

[16] R. C. Chirla. *Attosecond Pulse Generation and Characterization.* Ph.D. thesis, The Ohio State University, Columbus, OH, 2011.

[17] Y.-H. Chiu, N. G. Minutillo, R. E. Williams, G. J. Smith, D. W. McComb, J. A. Carlin, E. Johnston-Halperin, and F. Yang. Photoluminescence evolution in GaAs/AlGaAs core/shell nanowires grown by MOCVD: Effects of core growth temperature and substrate orientation. *Journal of Crystal Growth*, 429:1–5, Nov. 2015.

[18] A. Cirri, J. Husek, S. Biswas, and L. R. Baker. Achieving Surface Sensitivity in Ultrafast XUV Spectroscopy: M2,3-Edge Reflection–Absorption of Transition Metal Oxides. *J. Phys. Chem. C*, 121(29):15861–15869, July 2017.

[19] E. Constant, D. Garzella, P. Breger, E. Mével, C. Dorrer, C. Le Blanc, F. Salin, and P. Agostini. Optimizing High Harmonic Generation in Absorbing Gases: Model and Experiment. *Phys. Rev. Lett.*, 82(8):1668–1671, Feb. 1999.

[20] P. B. Corkum. Plasma perspective on strong field multiphoton ionization. *Phys. Rev. Lett.*, 71(13):1994–1997, Sept. 1993.

[21] S. K. Cushing, A. Lee, I. J. Porter, L. M. Carneiro, H.-T. Chang, M. Zürch, and S. R. Leone. Differentiating Photoexcited Carrier and Phonon Dynamics in the $\Delta$, $L$ , and $\Gamma$ Valleys of Si(100) with Transient Extreme Ultraviolet Spectroscopy. *J. Phys. Chem. C*, 123(6):3343–3352, Feb. 2019.

[22] J.-C. Diels and W. Rudolph. *Ultrashort Laser Pulse Phenomena: Fundamentals, Techniques, and Applications on a Femtosecond Time Scale.* Optics and Photonics. Elsevier / Academic Press, Amsterdam ; Boston, 2nd ed edition, 2006.

[23] L. Drescher, O. Kornilov, T. Witting, G. Reitsma, N. Monserud, A. Rouzée, J. Mikosch, M. J. J. Vrakking, and B. Schütte. Extreme-ultraviolet refractive optics. *Nature*, 564(7734):91, Dec. 2018.

[24] S. Eich, A. Stange, A. V. Carr, J. Urbancic, T. Popmintchev, M. Wiesenmayer, K. Jansen, A. Ruffing, S. Jakobs, T. Rohwer, S. Hellmann, C. Chen, P. Matyba, L. Kipp, K. Rossnagel, M. Bauer, M. M. Murnane, H. C. Kapteyn, S. Mathias, and M. Aeschlimann. Time- and angle-resolved photoemission spectroscopy with optimized high-harmonic pulses using frequency-doubled Ti:Sapphire lasers. *Journal of Electron Spectroscopy and Related Phenomena*, 195:231–236, Aug. 2014.

[25] U. Even. The Even-Lavie valve as a source for high intensity supersonic beam. *EPJ Techn Instrum*, 2(1):17, Dec. 2015.

[26] A. D. Farinas and E. D. Green. Optical beam steering and sampling apparatus and method, May 2009.

[27] G. Fraser. X- and $\gamma$-ray imaging using microchannel plates. *Nuclear Instruments and Methods in Physics Research*, 221(1):115–130, Mar. 1984.

[28] G. M. Fryer and R. M. Barrer. A theory of gas flow through capillary tubes. *Proceedings of the Royal Society of London. Series A. Mathematical and Physical Sciences*, 293(1434):329–341, Aug. 1966.

[29] E. G. Gamaly, A. V. Rode, B. Luther-Davies, and V. T. Tikhonchuk. Ablation of solids by femtosecond lasers: Ablation mechanism and ablation thresholds for metals and dielectrics. *Physics of Plasmas*, 9(3):949–957, Feb. 2002.

[30] A. Gibaud and G. Vignaud. Specular Reflectivity from Smooth and Rough Surfaces. In J. Daillant and A. Gibaud, editors, *X-Ray and Neutron Reflectivity: Principles and Applications*, Lecture Notes in Physics, pages 85–131. Springer Berlin Heidelberg, Berlin, Heidelberg, 2009.

[31] T. Gorman. *Attosecond Probing of Electron Dynamics in Atoms and Molecules Using Tunable Mid-Infrared Drivers.* Ph.D. thesis, The Ohio State University, Columbus, OH, 2018.

[32] E. Gullikson. CXRO X-Ray Interactions With Matter. http://henke.lbl.gov/optical_constants/.

[33] M. H. Hablanian. *High-Vacuum Technology: A Practical Guide*. Number 111 in Mechanical Engineering. Marcel Dekker, New York, 2nd ed., rev. and expanded edition, 1997.

[34] S. J. Hageman. *Complex Attosecond Transient-Absorption Spectroscopy*. PhD thesis, The Ohio State University, Columbus, OH, 2020.

[35] M. Harb, R. Ernstorfer, T. Dartigalongue, C. T. Hebeisen, R. E. Jordan, and R. J. D. Miller. Carrier Relaxation and Lattice Heating Dynamics in Silicon Revealed by Femtosecond Electron Diffraction. *J. Phys. Chem. B*, 110(50):25308–25313, Dec. 2006.

[36] B. L. Henke, E. M. Gullikson, and J. C. Davis. X-Ray Interactions: Photoabsorption, Scattering, Transmission, and Reflection at E = 50-30,000 eV, Z = 1-92. *Atomic Data and Nuclear Data Tables*, 54(2):181–342, July 1993.

[37] D. M. Hoffman, B. Singh, and J. H. Thomas, editors. *Handbook of Vacuum Science and Technology*. Academic Press, San Diego, CA, 1998.

[38] M. R. Howells. Mirrors for Synchrotron-Radiation Beamlines. In A. S. Schlachter and F. J. Wuilleumier, editors, *New Directions in Research with Third-Generation Soft X-Ray Synchrotron Radiation Sources*, NATO ASI Series, pages 359–385. Springer Netherlands, Dordrecht, 1994.

[39] D. Irimia, D. Dobrikov, R. Kortekaas, H. Voet, D. A. van den Ende, W. A. Groen, and M. H. M. Janssen. A short pulse (7 microsecond FWHM) and high repetition rate (dc-5kHz) cantilever piezovalve for pulsed atomic and molecular beams. *Review of Scientific Instruments*, 80(11):113303, Nov. 2009.

[40] D. Irimia, R. Kortekaas, and M. H. M. Janssen. In situ characterization of a cold and short pulsed molecular beam by femtosecond ion imaging. *Phys. Chem. Chem. Phys.*, 11(20):3958, 2009.

[41] D. Kane and R. Trebino. Characterization of arbitrary femtosecond pulses using frequency-resolved optical gating. *IEEE J. Quantum Electron.*, 29(2):571–579, Feb./1993.

[42] C. J. Kaplan, P. M. Kraus, A. D. Ross, M. Zürch, S. K. Cushing, M. F. Jager, H.-T. Chang, E. M. Gullikson, D. M. Neumark, and S. R. Leone. Femtosecond tracking of carrier relaxation in germanium with extreme ultraviolet transient reflectivity. *Phys. Rev. B*, 97(20):205202, May 2018.

[43] S. Kazamias, S. Daboussi, O. Guilbaud, K. Cassou, D. Ros, B. Cros, and G. Maynard. Pressure-induced phase matching in high-order harmonic generation. *Phys. Rev. A*, 83(6):063405, June 2011.

[44] S. Kazamias, F. Weihe, D. Douillet, C. Valentin, T. Planchon, S. Sebban, G. Grillon, F. Augé, D. Hulin, and P. Balcou. High order harmonic generation optimization with an apertured laser beam. *Eur. Phys. J. D*, 21(3):353–359, Dec. 2002.

[45] L. Keldysh. Ionization in the Field of a Strong Electromagnetic Wave. *SOVIET PHYSICS JETP*, 20:1307–1314, May 1965.

[46] D. Kiesewetter. *Dynamics of Near-Threshold Attosecond Electron Wavepackets in Strong Laser Fields*. Ph.D. thesis, The Ohio State University, Columbus, OH, 2019.

[47] P. Kirkpatrick and A. V. Baez. Formation of Optical Images by X-Rays. *J. Opt. Soc. Am.*, 38(9):766, Sept. 1948.

[48] J. L. Krause, K. J. Schafer, and K. C. Kulander. Calculation of photoemission from atoms subject to intense laser fields. *Phys. Rev. A*, 45(7):4998–5010, Apr. 1992.

[49] S. Kühn, M. Dumergue, S. Kahaly, S. Mondal, M. Füle, T. Csizmadia, B. Farkas, B. Major, Z. Várallyay, E. Cormier, M. Kalashnikov, F. Calegari, M. Devetta, F. Frassetto, E. Månsson, L. Poletto, S. Stagira, C. Vozzi, M. Nisoli, P. Rudawski, S. Maclot, F. Campi, H. Wikmark, C. L. Arnold, C. M. Heyl, P. Johnsson, A. L'Huillier, R. Lopez-Martens, S. Haessler, M. Bocoum, F. Boehle, A. Vernier, G. Iaquaniello, E. Skantzakis, N. Papadakis, C. Kalpouzos, P. Tzallas, F. Lépine, D. Charalambidis, K. Varjú, K. Osvay, and G. Sansone. The ELI-ALPS facility: The next generation of attosecond sources. *J. Phys. B: At. Mol. Opt. Phys.*, 50(13):132002, July 2017.

[50] J. Ladislas Wiza. Microchannel plate detectors. *Nuclear Instruments and Methods*, 162(1):587–601, June 1979.

[51] J. Ladislas Wiza. Microchannel plate detectors. *Nuclear Instruments and Methods*, 162(1-3):587–601, June 1979.

[52] Y. H. Lai, J. Xu, U. B. Szafruga, B. K. Talbert, X. Gong, K. Zhang, H. Fuest, M. F. Kling, C. I. Blaga, P. Agostini, and L. F. DiMauro. Experimental investigation of strong-field-ionization theories for laser fields from visible to midinfrared frequencies. *Phys. Rev. A*, 96(6):063417, Dec. 2017.

[53] L. D. Landau, E. M. Lifšic, and L. D. Landau. *Fluid Mechanics*. Number by L. D. Landau and E. M. Lifshitz ; Vol. 6 in Course of Theoretical Physics. Elsevier/Butterworth Heinemann, Amsterdam [u.a], 2. engl. ed., rev., reprint. with corr edition, 2011. OCLC: 934875040.

[54] M. Lewenstein, P. Balcou, M. Y. Ivanov, A. L'Huillier, and P. B. Corkum. Theory of high-harmonic generation by low-frequency laser fields. *Phys. Rev. A*, 49(3):2117–2132, Mar. 1994.

[55] I. H. Malitson. Interspecimen Comparison of the Refractive Index of Fused Silica. *J. Opt. Soc. Am.*, 55(10):1205, Oct. 1965.

[56] C. R. Mansfield and E. R. Peck. Dispersion of Helium. *J. Opt. Soc. Am., JOSA*, 59(2):199–204, Feb. 1969.

[57] C. Meng and M. H. M. Janssen. Measurement of the density profile of pure and seeded molecular beams by femtosecond ion imaging. *Review of Scientific Instruments*, 86(2):023110, Feb. 2015.

[58] D. R. Miller. Free Jet Sources (Chap 2). In G. Scoles, editor, *Atomic and Molecular Beam Methods*, volume 1, pages 14–82. Oxford University Press, 1988.

[59] J. Mooney and P. Kambhampati. Get the Basics Right: Jacobian Conversion of Wavelength and Energy Scales for Quantitative Analysis of Emission Spectra. *J. Phys. Chem. Lett.*, 4(19):3316–3318, Oct. 2013.

[60] H. Motoyama, T. Saito, and H. Mimura. Error analysis of ellipsoidal mirrors for soft X-ray focusing by wave-optical simulation. *Jpn. J. Appl. Phys.*, 53(2):022503, Feb. 2014.

[61] E. Nichelatti. Complex refractive index of a slab from reflectance and transmittance: Analytical solution. *J. Opt. A: Pure Appl. Opt.*, 4(4):400–403, July 2002.

[62] H. Noda, T. Namioka, and M. Seya. Geometric theory of the grating. *J. Opt. Soc. Am.*, 64(8):1031, Aug. 1974.

[63] T. N. Nunley, N. S. Fernando, N. Samarasingha, J. M. Moya, C. M. Nelson, A. A. Medina, and S. Zollner. Optical constants of germanium and thermally grown germanium dioxide from 0.5 to 6.6eV via a multisample ellipsometry investigation. *Journal of Vacuum Science & Technology B, Nanotechnology and Microelectronics: Materials, Processing, Measurement, and Phenomena*, 34(6):061205, Nov. 2016.

[64] S. O'Bryan. *High Resolution XUV Spectrometer: An Overview.* Master's Thesis, The Ohio State University, Columbus, OH, May 2015.

[65] N. Passilly, F. Treussart, R. Hierle, R. de Saint Denis, K. Aït-Ameur, and J.-F. Roch. Simple interferometric technique for generation of a radially polarized light beam. *J. Opt. Soc. Am. A*, 22(5):984, May 2005.

[66] J. Peatross, J. L. Chaloupka, and D. D. Meyerhofer. High-order harmonic generation with an annular laser beam. *Opt. Lett., OL*, 19(13):942–944, July 1994.

[67] E. R. Peck and D. J. Fisher. Dispersion of Argon. *J. Opt. Soc. Am., JOSA*, 54(11):1362–1364, Nov. 1964.

[68] R. Pfisterer and S. Johnston. FRED Optical Engineering Software. Photon Engineering.

[69] A. Piper. *Andrew Piper's Dissertation (in Progress)*. PhD thesis, The Ohio State University, 2022.

[70] L. Poletto, F. Frassetto, F. Calegari, S. Anumula, A. Trabattoni, and M. Nisoli. Microfocusing of attosecond pulses by grazing-incidence toroidal mirrors. *Opt. Express, OE*, 21(11):13040–13051, June 2013.

[71] T. Popmintchev, M.-C. Chen, A. Bahabad, M. Gerrity, P. Sidorenko, O. Cohen, I. P. Christov, M. M. Murnane, and H. C. Kapteyn. Phase matching of high harmonic generation in the soft and hard X-ray regions of the spectrum. *PNAS*, 106(26):10516–10521, June 2009.

[72] T. Popmintchev, M.-C. Chen, O. Cohen, M. E. Grisham, J. J. Rocca, M. M. Murnane, and H. C. Kapteyn. Extended phase matching of high harmonics driven by mid-infrared light. *Opt. Lett., OL*, 33(18):2128–2130, Sept. 2008.

[73] K. Ramasesha, S. R. Leone, and D. M. Neumark. Real-Time Probing of Electron Dynamics Using Attosecond Time-Resolved Spectroscopy. *Annu. Rev. Phys. Chem.*, 67(1):41–63, May 2016.

[74] J. Rothhardt, M. Krebs, S. Hädrich, S. Demmler, J. Limpert, and A. Tünnermann. Absorption-limited and phase-matched high harmonic generation in the tight focusing regime. *New J. Phys.*, 16(3):033022, Mar. 2014.

[75] P. Salières, A. L'Huillier, and M. Lewenstein. Coherence Control of High-Order Harmonics. *Phys. Rev. Lett.*, 74(19):3776–3779, May 1995.

[76] K. J. Schafer, B. Yang, L. F. DiMauro, and K. C. Kulander. Above threshold ionization beyond the high harmonic cutoff. *Phys. Rev. Lett.*, 70(11):1599–1602, Mar. 1993.

[77] S. B. Schoun. *Attosecond High-Harmonic Spectroscopy of Atoms and Molecules Using Mid-Infrared Sources*. Ph.D. thesis, The Ohio State University, Columbus, OH, 2015.

[78] M. Schultze, K. Ramasesha, C. D. Pemmaraju, S. A. Sato, D. Whitmore, A. Gandman, J. S. Prell, L. J. Borja, D. Prendergast, K. Yabana, D. M. Neumark, and S. R. Leone. Attosecond band-gap dynamics in silicon. *Science*, 346(6215):1348–1352, Dec. 2014.

[79] A. Sentenac and J. Daillant. Statistical Aspects of Wave Scattering at Rough Surfaces. In J. Daillant and A. Gibaud, editors, *X-Ray and Neutron Reflectivity: Principles and Applications*, Lecture Notes in Physics, pages 59–84. Springer Berlin Heidelberg, Berlin, Heidelberg, 2009.

[80] A. D. Shiner, C. Trallero-Herrero, N. Kajumba, H.-C. Bandulet, D. Comtois, F. Légaré, M. Giguère, J.-C. Kieffer, P. B. Corkum, and D. M. Villeneuve. Wavelength Scaling of High Harmonic Generation Efficiency. *Phys. Rev. Lett.*, 103(7):073902, Aug. 2009.

[81] S. L. Sorensen, T. Åberg, J. Tulkki, E. Rachlew-Källne, G. Sundström, and M. Kirm. Argon 3s autoionization resonances. *Phys. Rev. A*, 50(2):1218–1230, Aug. 1994.

[82] K. N. Stoev and K. Sakurai. Review on grazing incidence X-ray spectrometry and reflectometry. *Spectrochimica Acta Part B: Atomic Spectroscopy*, 54(1):41–82, Jan. 1999.

[83] D. Strickland and G. Mourou. Compression of amplified chirped optical pulses. *Optics Communications*, 56(3):219–221, Dec. 1985.

[84] E. Takahashi, Y. Nabekawa, H. Mashiko, H. Hasegawa, A. Suda, and K. Midorikawa. Generation of Strong Optical Field in Soft X-Ray Region by Using High-Order Harmonics. *IEEE J. Select. Topics Quantum Electron.*, 10(6):1315–1328, Nov. 2004.

[85] J. Tate, T. Auguste, H. G. Muller, P. Salières, P. Agostini, and L. F. DiMauro. Scaling of Wave-Packet Dynamics in an Intense Midinfrared Field. *Phys. Rev. Lett.*, 98(1):013901, Jan. 2007.

[86] X. M. Tong and C. D. Lin. Empirical formula for static field ionization rates of atoms and molecules by lasers in the barrier-suppression regime. *J. Phys. B: At. Mol. Opt. Phys.*, 38(15):2593–2600, Aug. 2005.

[87] G. Vdovin, F. van Goor, and Guyskk. LightPipes for Python. Flexible Optical.

[88] D. C. Venerus. Laminar capillary flow of compressible viscous fluids. *J. Fluid Mech.*, 555:59, May 2006.

[89] M. Volkov, S. A. Sato, F. Schlaepfer, L. Kasmi, N. Hartmann, M. Lucchini, L. Gallmann, A. Rubio, and U. Keller. Attosecond screening dynamics mediated by electron localization in transition metals. *Nat. Phys.*, pages 1–5, Aug. 2019.

[90] Z. Wang. *Mid-Infrared Strong-Field Laser Interactions with Nanoclusters and Semiconductors*. Ph.D. thesis, The Ohio State University, Columbus, OH, 2018.

[91] S. Zahedpour, J. K. Wahlstrand, and H. M. Milchberg. Measurement of the nonlinear refractive index of air constituents at mid-infrared wavelengths. *Opt. Lett.*, 40(24):5794, Dec. 2015.

[92] A. Zangwill. *Modern Electrodynamics.* Cambridge University Press, Cambridge, 2013.

[93] Q. Zhang, K. Zhao, J. Li, M. Chini, Y. Cheng, Y. Wu, E. Cunningham, and Z. Chang. Suppression of driving laser in high harmonic generation with a microchannel plate. *Opt. Lett.*, 39(12):3670, June 2014.

[94] M. Zürch, H.-T. Chang, L. J. Borja, P. M. Kraus, S. K. Cushing, A. Gandman, C. J. Kaplan, M. H. Oh, J. S. Prell, D. Prendergast, C. D. Pemmaraju, D. M. Neumark, and S. R. Leone. Direct and simultaneous observation of ultrafast electron and hole dynamics in germanium. *Nat Commun*, 8(1):15734, Aug. 2017.